Spectrum sensing using software defined radio receivers

Tamer Badran

THÈSE DE DOCTORAT DE
SORBONNE UNIVERSITÉ

École Doctorale Informatique, Télécommunications et Électronique (EDITE)

Présentée par

Tamer BADRAN

Pour obtenir le grade de

Docteur de Sorbonne Université

Sujet de la thèse :

Balayage de Spectre Utilisant les Récepteurs Radio Logicielle

Date de soutenance : **le 23 Mars 2020**

Le jury est composé de :

Mme. Lirida Naviner	Rapporteuse
M. Khaled Salama	Rapporteur
M. Ramon Parra-Michel	Examinateur
M. Mostafa Hussien	Examinateur
M. Bryce Minger	Examinateur
Mme. Nguyen Thi-Mai-Trang	Examinatrice
M. Naceur Malouch	Examinateur
M. Hassan Aboushady	Directeur de thèse
M. Haralampos Stratigopoulos	Invité

Ph.D. THESIS OF SORBONNE UNIVERSITY

Thesis subject

is

Spectrum Sensing using Software Defined Radio Receivers

A Dissertation

by

Tamer BADRAN

Submitted to obtain the PhD degree from

Sorbonne University

Defense date: **March 23, 2020**

Committee in charge :

Mrs. Lirida Naviner	Telecom Paris, France
Mr. Khaled Salama	KAUST, KSA
Mr. Ramon Parra-Michel	CINVESTAV, Mexico
Mr. Mostafa Hussien	AASTMT, Egypt
Mr. Bryce Minger	Thales, France
Mrs. Thi-Mai-Trang Nguyen	Sorbonne University, France
Mr. Naceur Malouch	Sorbonne University, France
Mr. Hassan Aboushady	Sorbonne University, France
Mr. Haralampos Stratigopoulos	Sorbonne University, France

Contents

List of Figures

List of Tables

Chapter 1

Introduction

1.1 Context

Spectrum Sensing is used in a wide range of modern applications. In Cognitive Radio, in order to optimize the frequency spectrum utilization, awareness of the occupancy of different transmission bands is crucial [Ejaz18]. As shown in Fig. 1.1, hopping from frequency band to another depending on the availability of those bands optimizes transmission and improves quality of service (QoS).

Spectrum sensing is used also in medical applications, to study the side effects of RF electromagnetic field (EMF) exposure on health. Fig. 1.2a shows the geographical density of cellular towers and WiFi networks in 2003. That density was dramatically increased by 2017, as shown in Fig. 1.2b.

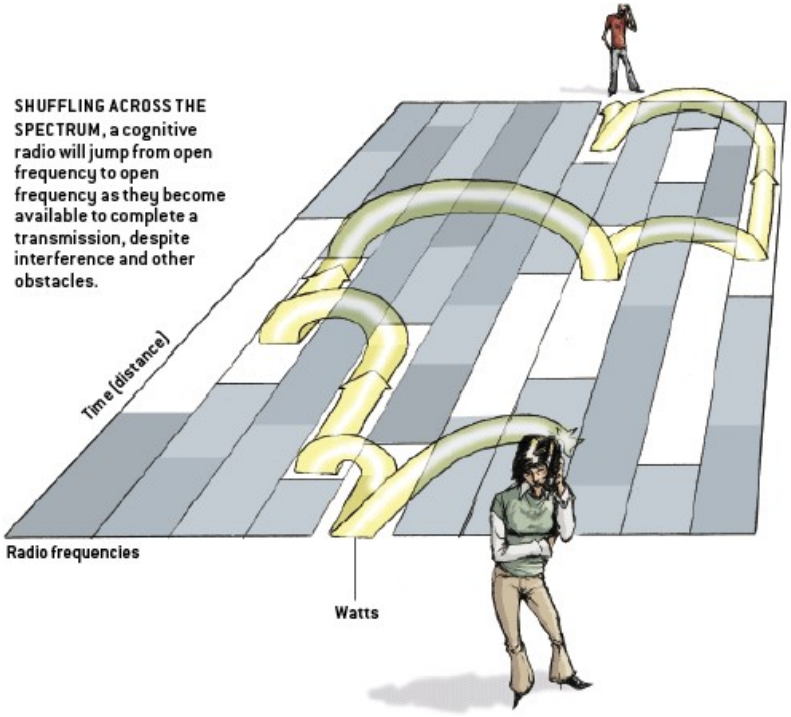

Fig. 1.1: Spectrum Sensing can be used in Wireless Communication to optimize spectrum utilization [Ashley06]

1.2 Thesis Structure

The thesis is organized as follows:

- The motivation and the state of the art related to this thesis' work are reviewed in Chapter 2.
- Chapter 3 presents the system-level design of a tunable bandpass Delta-Sigma ADC.
- A spectrum sensing architecture based on tunable bandpass $\Delta\Sigma$ ADC is presented in Chapter 4. The effect of nonlinearity on the performance is studied.
- A conventional transceiver system is calibrated and tested for spectrum sensing application performance in chapter 6. The effect of I/Q imbalance on the performance is shown by hardware measurement results.
- Neonates exposure to RF-EMF and its effect on their physiological parameters is studied in chapter 7.

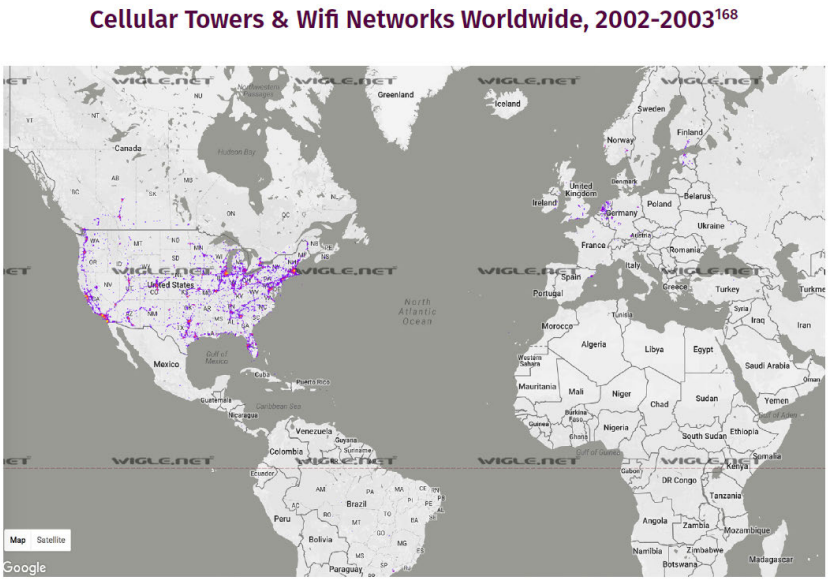

(a) Geographical Density of Cellular Towers and WiFi Networks in 2003

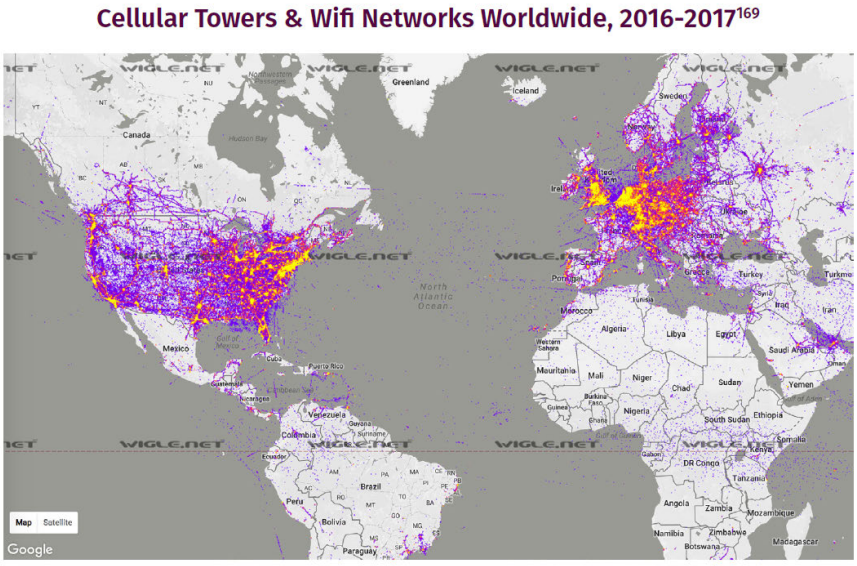

(b) Geographical Density of Cellular Towers and WiFi Networks in 2017

Fig. 1.2: Evolution of Geographical Density of Cellular Towers and WiFi Networks [Pineault17]

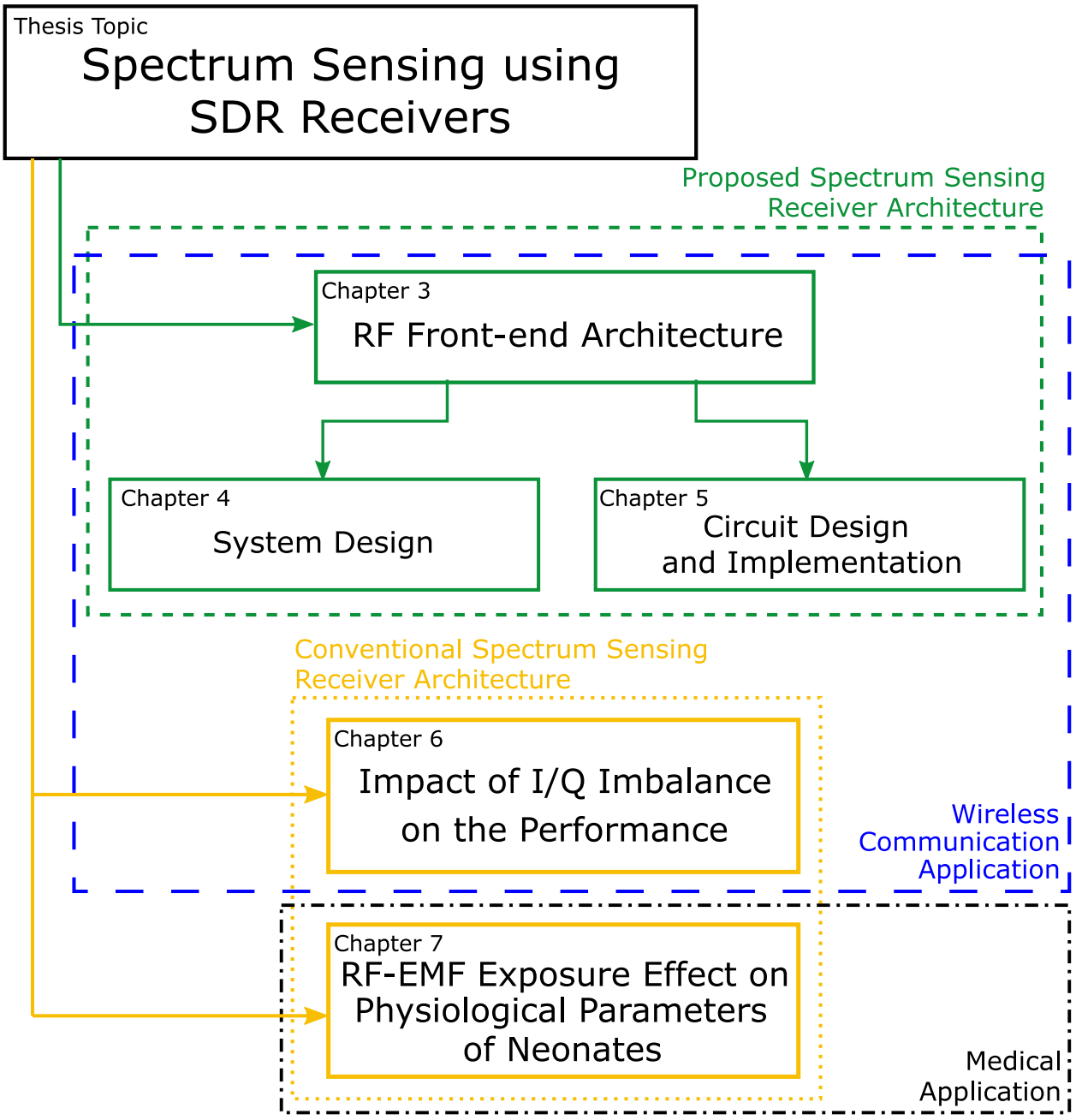

Fig. 1.3: Graphic Illustration of the Thesis Structure

- Finally, chapter 8 conclude the thesis.

Fig. 1.3 illustrates the thesis structure graphically.

Chapter 2

Thesis Contribution and Related Work

2.1 Introduction

This chapter presents the thesis contributions and their positioning with respect to the state of the art. Section 2.2, illustrates the different aspects of spectrum sensing. The order of remaining sections is made same as the thesis chapters. The proposed RF front-end of the proposed spectrum sensing receiver architecture is presented in section 2.3. Section 2.4 discusses the complete receiver architecture, the energy-detection spectrum sensing technique, and the effect of circuit nonlinearity on the spectrum sensing performance. The spectrum sensing receiver implementation is presented in section 2.5. The work related to the impact of I/Q imbalance on the performance of conventional spectrum sensing receivers is reviewed in section 2.6. Section 2.7 discusses spectrum sensing in medical applications. Finally, section 2.8 summarizes the contributions of this thesis.

2.2 Spectrum Sensing

There are many aspects of spectrum sensing, as shown in Fig. 2.1 [Yucek09b]. Some standards inherently utilizes spectrum sensing in the operation [Bluetooth10, ISO12, IEE19].

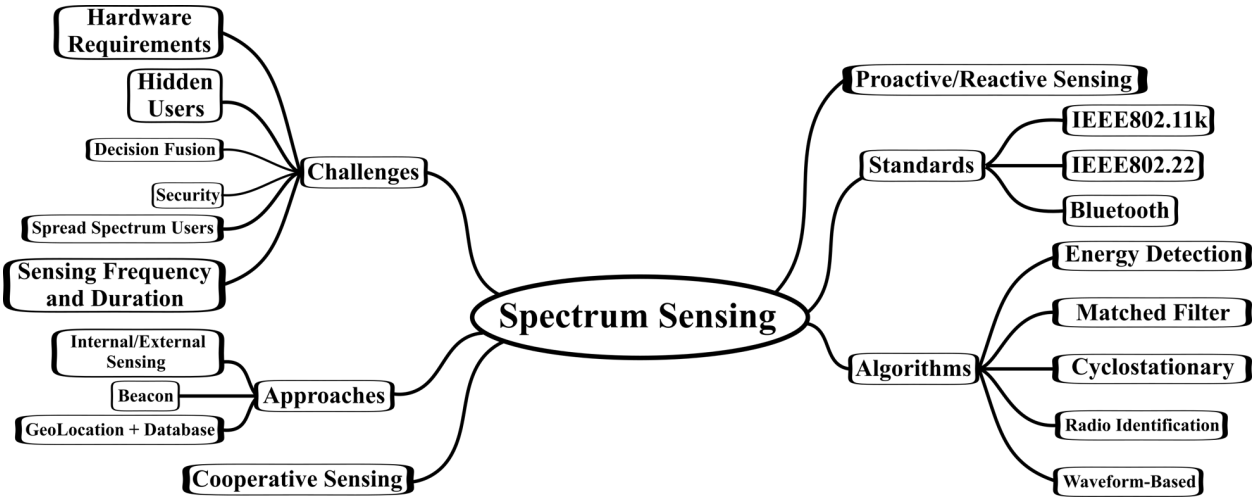

Fig. 2.1: Spectrum Sensing Aspects [Yucek09b]

The spectrum sensing can be either reactive or proactive. In reactive spectrum sensing, the system has only one receiver which switches between signal reception and sensing the spectrum. In a proactive system, there are two receivers, one dedicated for sensing the spectrum and the other is dedicated for signal reception. Proactive sensing system is preferred because the availability of different bands will be ready as soon as the system needs it, despite that it consumes additional power and area for the extra receiver.

The evaluation metrics for a spectrum sensing receiver depend mainly on two probabilities. The first is the probability of detection, P_D, which characterize how much of the busy bands are actually detected as busy by the algorithm. The second is probability of false-alarm, P_{FA}, which characterize how much available bands are detected as busy bands. Normally, two curves are plotted to evaluate the performance, first is P_D versus Signal-to-Noise-Ratio (SNR) and secondly and more importantly the receiver operating characteristics (ROC) which shows P_{FA} versus P_D.

One of the main challenges in spectrum sensing is the sensing frequency, duration, and resolution. Some legacy systems constraint how frequently the sensing process happens. As soon as the secondary user started using a specific band, the frequency of sensing should be increase in order not to interfere with the primary user. Sensing duration is crucial to the secondary device itself, as the faster sensing is done the faster the secondary device can establish com-

Table 2.1: Spectrum Sensing Techniques

Feature	**Energy Detection**	**Cyclostationary Feature Detection**	**Matched Filter**
Prior Signal Knowledge	None	Preferred	Fully Required
Complexity	Very Low	Moderate	Very High
Modulation Type Dependent	No	Yes	Yes
Latency	Low	high	Low
Immunity to Noise Uncertainty	Low	Moderate	High

munication. Finally, sensing resolution increase the awareness of the spectrum under study, because having a low sensing resolution (one sensing decision for a wide frequency band) may waste a chance of finding available channels that can be used for transmission.

There are many algorithms for spectrum sensing, the most used ones are: Energy Detection [Alom17,Ramírez18,Nasrallah17,Chhagan18,Medina18,Karimi19], Cyclostationary Feature Detection [Cohen17, Tani15, Liu19, Mathew19], and Matched Filtering [Surampudi16, Lv15]. Table 2.1 summarizes the properties of those three algorithms. Also there are hybrid systems that combines Energy Detection with Cyclostationary Feature Detection [Sengupta19, Ivanov18, Ishwerya17].

In this thesis, Energy Detection Spectrum Sensing is chosen mainly for its suitability for hardware implementation and more importantly its independence on the prior knowledge of the transmitted signals.

2.3 Spectrum Sensing Receiver RF Front-end Architecture

The receiver RF front-end architecture used in all spectrum sensing publications contains many analog building blocks with a baseband ADC as shown in Fig. 2.2. For software defined radio, this architecture has high power consumption, and suffers from many nonidealities,

such as DC offset, frequency dependent amplifier gain, nonlinearity, I/Q mismatch.

Using a highly digitized receiver architecture, as shown in Fig. 2.3, would be beneficial in many ways for Spectrum Sensing. It would alleviate the issue of I/Q mismatch, and decrease the overall effect of other nonidealities (DC Offset, Nonlinearity, ...). One efficient implementation of highly digitized receiver is based on bandpass $\Delta\Sigma$ ADC [Haghighitalab18, Belfort17, Ashry13, Martens12, Beilleau09]. Bandpass $\Delta\Sigma$ based receivers have a relatively narrowband and are not suitable for wideband spectrum sensing applications. In order to cover a wide frequency range, a tunable bandpass $\Delta\Sigma$ ADC based receiver is required. In many reports of tunable bandpass $\Delta\Sigma$ ADC based receiver [Shibata12, Kent III07, Gupta12], the receiver suffers from rather complex tuning system and resulting in a relatively high power consumption.

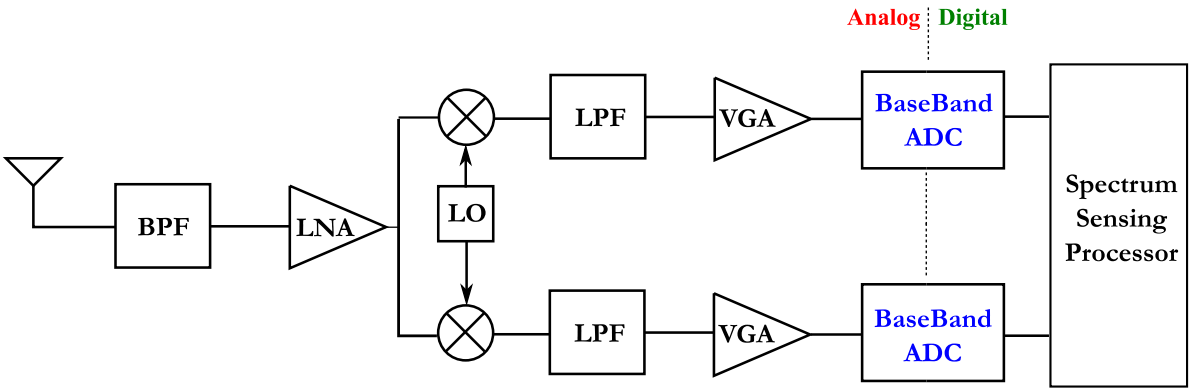

Fig. 2.2: Conventional RF Receiver

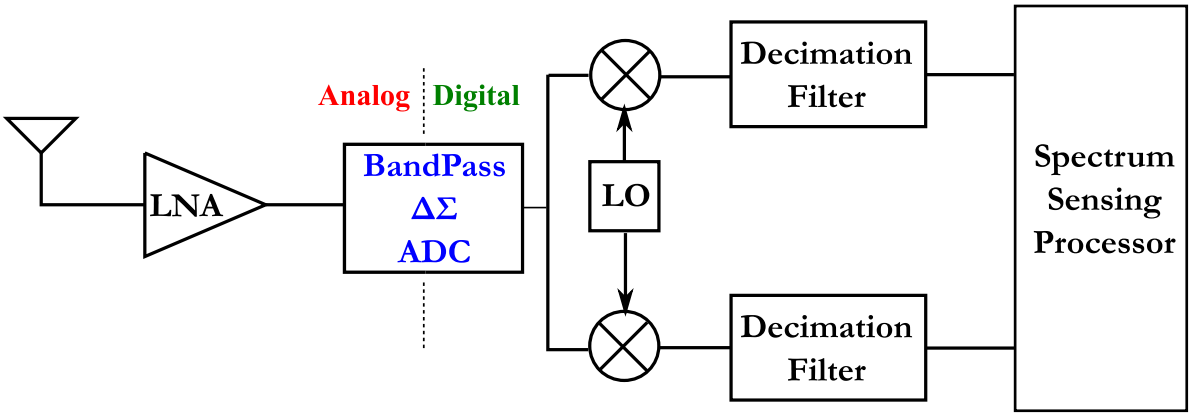

Fig. 2.3: Proposed Highly Digitized Receiver based on an RF $\Delta\Sigma$ ADC.

In this thesis, we present the system-level design of a wide-range low-complexity low-power tunable bandpass $\Delta\Sigma$ ADC in chapter 3.

2.4 Complete Spectrum Sensing System Design

Based on the Analog front-end presented in chapter 3, we propose a complete spectrum sensing receiver architecture in chapter 4, as shown also in Fig. 2.3.

In the Energy Detection Spectrum Sensing, the setting of energy threshold, at which the busy/available decision is taken, is shown to have a great impact on the performance. It has been demonstrated in [Umar13], that many previous energy detection publications set their threshold based on insufficient number of parameters. Also, several publication propose techniques to render the threshold immune to noise uncertainty and the assumed channel model [Mahendru19, Chatziantoniou15, Yu11].

In chapter 4, a test methodology for threshold setting, based on sufficient parameters, is proposed. Also a number of energy calculation samples is chosen with a compromise between the calculation accuracy and sensing duration.

An RF impairment, circuit nonlinearity, highly affects the receiver operation by producing intermodulation distortion components [Razavi11]. Some reports studied the effect of circuit nonlinearity on the performance of spectrum sensing analytically [Boulogeorgos16, Rebeiz15, Taparugssanagorn14, Rebeiz13]. One publication [Safatly14], presented a mitigation technique and evaluated the introduced improvement using a commercial SDR platform. Those papers depended on the conventional receiver architecture for spectrum sensing. A study of the effect of circuit nonlinearity on the proposed $\Delta\Sigma$ based spectrum sensing architecture performance is also presented in chapter 4. The transmission scenarios to achieve that study were chosen to exploit nonlinearity effect on the performance.

2.5 Spectrum Sensing Circuit Design and Implementation

In most of the published work, the authors only build their chosen spectrum sensing algorithm, in other words only a part of the digital backend of the receiver, and they report

the performance based on simulating or testing that module with MATLAB generated baseband input data, that mimics the output of the conventional RF receiver architecture [Teguig18, Ambede17, Ambede17, Kumar17, Fouda17, Das15]. Only a few publications presented the results and performance of a complete spectrum sensing receiver with a commercial RF front-end, as shown in Fig. 2.4, and their own implemented spectrum sensing module [Wang17, Imana17].

In chapter 5, we present an FPGA implementation and validation of the digital backend of the proposed spectrum sensing receiver, including the energy detection processor. As illustrated in Fig. 2.5, the proposed digital backend is suitable for the BP $\Delta\Sigma$ RF front-end presented in section 2.3 (chapter 3).

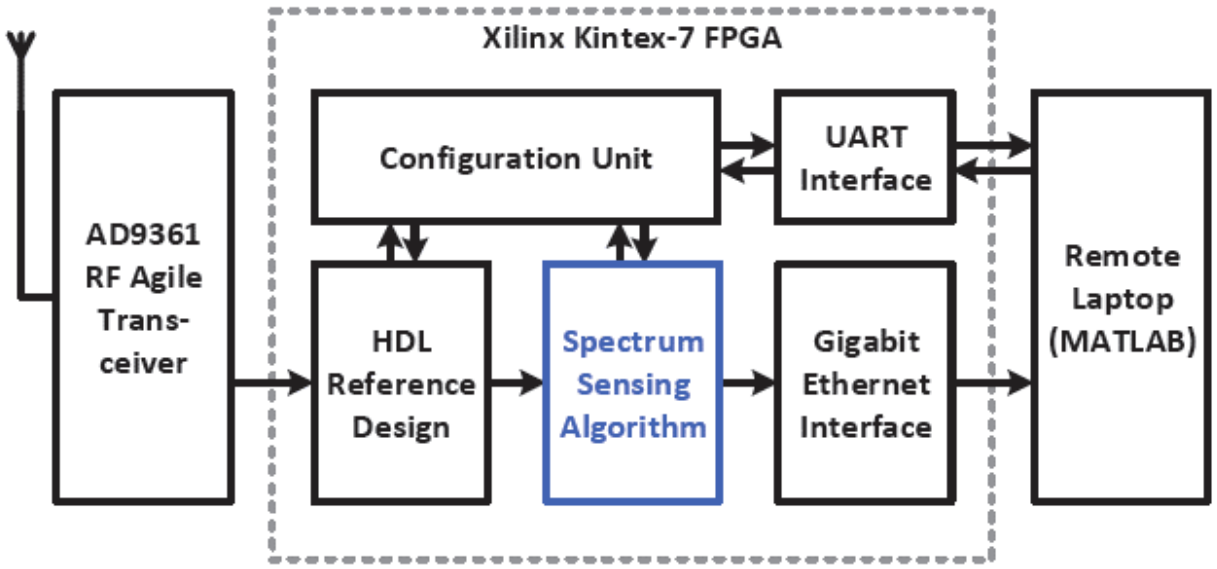

Fig. 2.4: Conventional Receiver Architecture based Spectrum Sensing, using a Commercial RF Front-end. Their contribution was only in the Spectrum Sensing Module [Wang17]

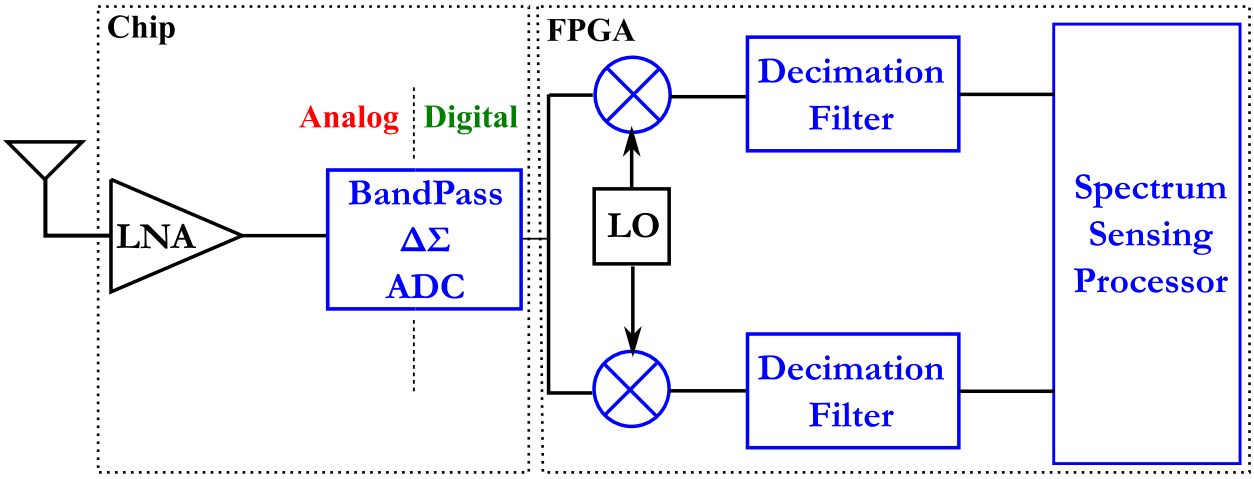

Fig. 2.5: Complete Proposed Architecture for Spectrum Sensing, including RF Front-end, Digital Backend and Spectrum Sensing Processor. Blocks in Blue are covered in this Thesis.

2.6 Impact of I/Q Imbalance on the Spectrum Sensing Performance

The Software Defined Radio (SDR) receiver responsible for spectrum sensing should be able to properly detect which bands are occupied by a primary user (PU) and which band can be used by a secondary user (SU). Fabrication process variations in the RF analog front-end (AFE) of a quadrature receiver lead to mismatch between the in-phase branch (I) and the quadrature branch (Q), as shown in Fig. 2.6. This impairment, known as I/Q Imbalance, reduces image rejection and significantly degrades the performance of the radio communication system [Razavi11].

Other papers have developed methods that can address the effects of I/Q imbalance in wireless communications [Rodriguez-Avila14, Valkama01, Diaz-Rizo18]. In the spectrum sensing context, the impact of I/Q imbalance was studied analytically in [Gokceoglu14, Imana17]. In these papers, only simulation results were used to study the impact of I/Q Imbalance on Spectrum Sensing metrics such as Probability of Detection, P_D, Probability of False Alarm, P_{FA}, and Receiver Operating Characteristics, RoC. In [Wang17], the authors presented interesting hardware measurement based RoC but they did not consider the effect of the RF analog front-end non-idealities on the energy detection performance.

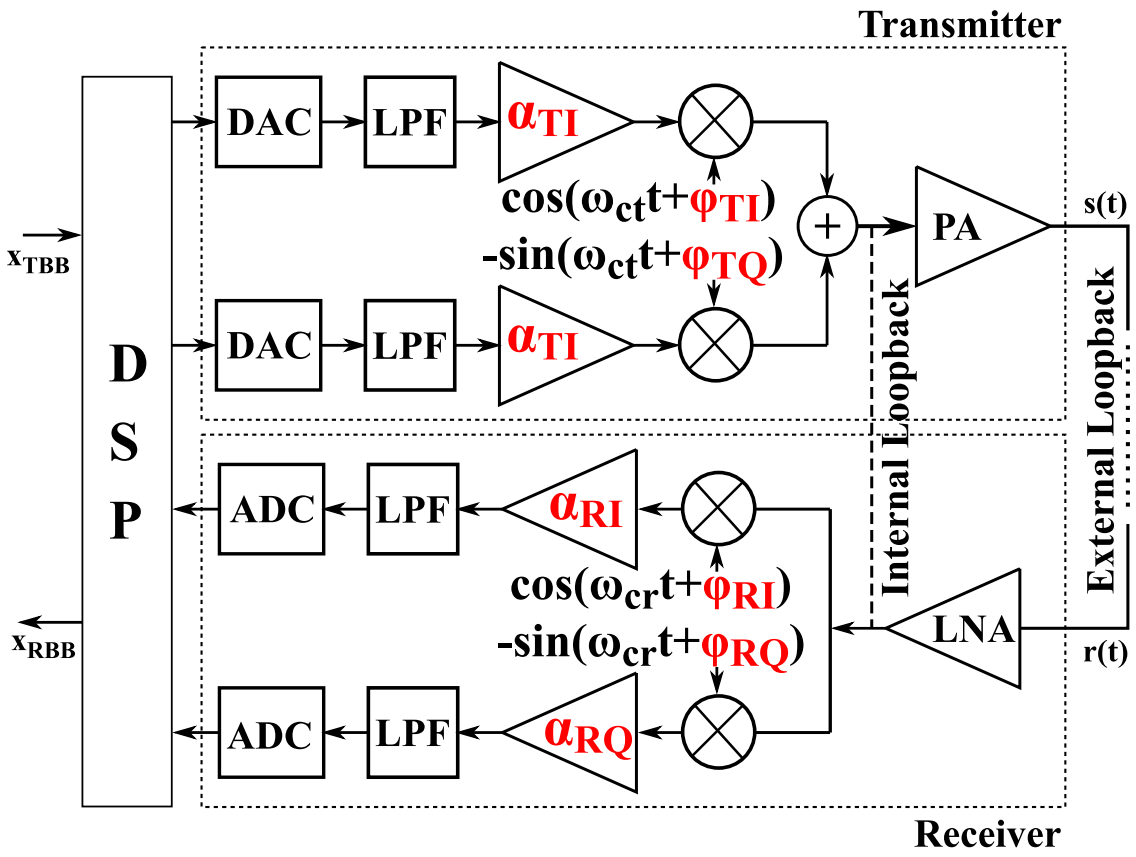

Fig. 2.6: The RF analog front-end of a Software Defined Radio Transceiver including gain and phase I/Q mismatch, DC-offset and frequency dependent gains.

In chapter 6, we perform hardware measurements to study the impact of I/Q imbalance on spectrum sensing algorithm based on energy detection using a conventional SDR platform. A conventional SDR is used because the proposed system in chapter 4 does not suffer from I/Q imbalance. The transmission scenarios to achieve that study were chosen to exploit the impact of I/Q imbalance on the performance.

2.7 Study of the RF-EMF Exposure Effect on the Physiological Parameters of Neonates

Spectrum Sensing can be used for numerous applications: Spectrum awareness and optimization of frequency bands utilization [Khalid19,Sun16,Rawat16,So15,Lai13], Vehicular Ad-Hoc

Networks (VANETs) [Liu17, Anushiya18], and Communication standards coexistence [Li17]. Also it is used in the field of security [Qing18, Elanagai17], Electronic Warfare [Orduyilmaz19], and in the medical field [Calvente17]

In chapter 7, we present the first study of the Radio Frequency ElectroMagnetic Field (RF-EMF) exposure effect on neonates. In this work, we performed simultaneous measurement of RF signals and the physiological parameters of neonates, as shown in Fig. 2.7

2.8 Contribution Summary

The main contributions of this thesis are:

- Chapter 3 [Aboushady20]:
  - System-Level Design of a low-power wide frequency range Tunable Bandpass $\Delta\Sigma$ ADC.

Fig. 2.7: Simultaneous Measurement of RF signals and the Physiological Parameters of Neonates.

- Chapter 4 [Badran20a]:
  - Energy Detection Spectrum Sensing Threshold Setting Methodology.
  - New Highly-Digitized Architecture for Spectrum Sensing Receivers with immunity to I/Q Imbalance.
  - Study of the Effect of Nonlinearity in the proposed architecture on the Spectrum Sensing Performance.
  - Proposing Testing Scenarios to Emphasize the Effect of Circuit Nonlinearity on the Spectrum Sensing Performance.
- Chapter 5 [Badran16, Badran20c]:
  - Implementation and Validation of the Digital Backend of the Proposed Spectrum Sensing Receiver Architecture.
- Chapter 6 [Badran20b]:
  - Wideband Calibration of a Commercial SDR Platform to perform Spectrum Sensing Measurements.
  - Study the I/Q Imbalance Effect on the Spectrum Sensing Performance in a Conventional SDR Platform.
  - Proposing Testing Scenarios to Emphasize the Effect of Circuit I/Q Imbalance, on the Spectrum Sensing Performance.
- Chapter 7:
  - First Study of the Effect of RF-EMF Exposure on the Physiological Parameters of Neonates.

2.9 Conclusions

In this chapter we explained the different aspects of spectrum sensing. The state of the art and the contribution of each chapter of the thesis were presented in sections 2.3 to 2.7. The major contributions of the thesis were also summarized in section 2.8.

Chapter 3

Spectrum Sensing Receiver RF Front-end Architecture

3.1 Introduction

In this chapter, we present an efficient realization of a tunable RF band-pass $\Delta\Sigma$ ADC with a wide tuning range (several gigahetrz). The proposed RF band-pass $\Delta\Sigma$ ADC has an LC resonator with a single-bit quantizer and a minimum number of feedback coefficients. Section 3.2 presents the architecture of bandpass ADC based receivers. The conventional tunable band-pass $\Delta\Sigma$ ADCs architectures are discussed in section 3.3. Section 3.4 presents the architecture and system-level design of the proposed tunable band-pass $\Delta\Sigma$ ADCs. Finally, Section 3.5 concludes the chapter.

3.2 Band-pass $\Delta\Sigma$ ADC Based Receivers

The conventional receiver architecture consists of mainly analog building blocks as shown in Fig. 3.1. This architecture suffers from high power consumption, high nonlinearity, mismatch, and high complexity. A highly digitized receiver architecure, as shown in Fig. 3.2, is easily programmable, alleviates the mismatch problem, and reduces nonlinearity and complexity. In order to build such architecure, a bandpass $\Delta\Sigma$ Analog-to-Digital Converter

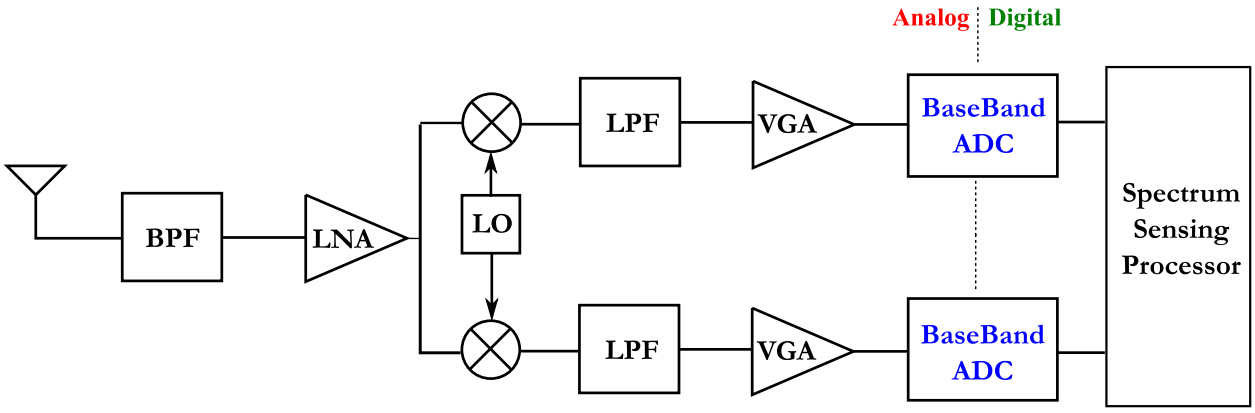

Fig. 3.1: Conventional RF Receiver

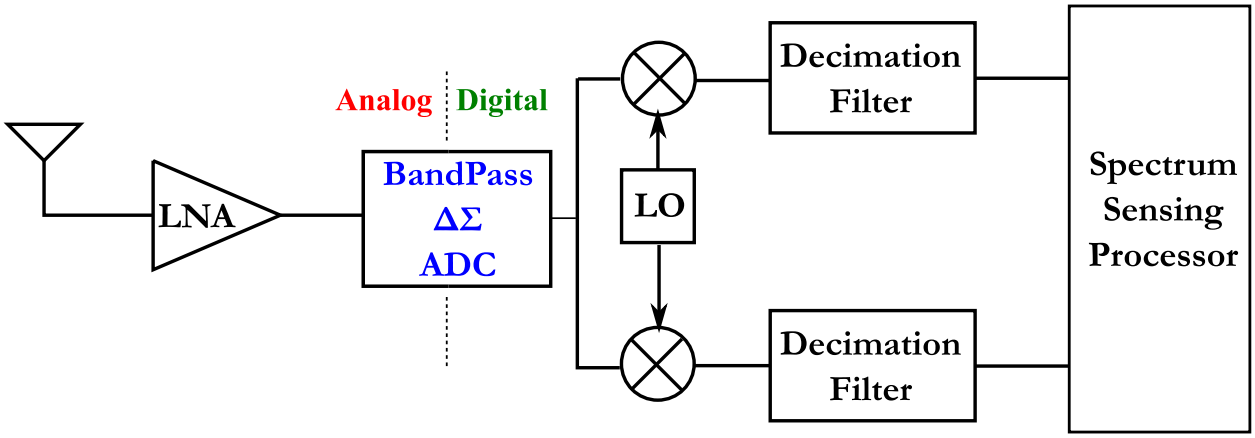

Fig. 3.2: Proposed Bandpass RF Receiver

(ADC) is required. As the ADC is now processing the signal at the carrier frequency, the down-conversion mixer is a digital one. Also because the $\Delta\Sigma$ ADC utilizes oversampling, a decimation filter is required. Having the in-phase and quadrature branches implemented in digital domain, alleviates nonidealities such as I/Q imbalance in phase and gain.

3.3 Conventional Tunable Band-Pass $\Delta\Sigma$ ADCs

The band-pass $\Delta\Sigma$ ADC aims to cover a frequency band around a certain center frequency f_0. However, the performance of this type of ADC is not sufficient, for the wide frequency range required for multi-standard applications. One way to increase the frequency range of

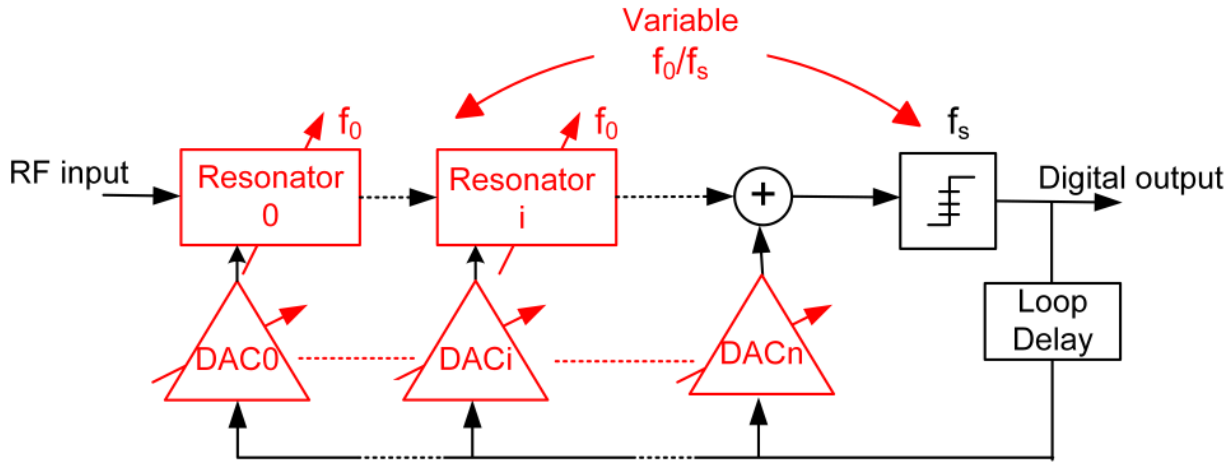

Fig. 3.3: Conventional Architecture using variable $\Delta\Sigma$ ADC Coefficients (Variable Normalized Loop Delay (t_d/T_s), Variable Normalized Center Frequency f_0/f_s)).

$\Delta\Sigma$ ADC is the use of tunable band-pass filter as loop filter. The solution to achieve tunable $\Delta\Sigma$ ADC mainly relies on changing the coefficients and adjusting the parameters to get stable modulator with the same Signal Transfer Function (STF) and Noise Transfer Function (NTF) for each tuning center Frequency f_0, as shown in Fig. 3.3.

The main drawback of the aforementioned modulator is that all the feedback and feed forward coefficients of these $\Delta\Sigma$ modulators have to be tuned with the center frequency. This makes these architectures rather complex which leads to a limited tuning range and a significant increase in the power consumption. As shown in Fig. 3.3, in the work presented in [Shibata12] and [Kent III07], the $\Delta\Sigma$ coefficients have to be tuned for each center frequency for the following reasons:

- The sampling frequency $f_s = 1/T_s$ is variable leading to a variable normalized Loop delay (t_d/T_s). The $\Delta\Sigma$ coefficients are function of the normalized Loop delay.
- The normalized sampling frequency f_0/f_s is variable, as shown in Fig. 3.4, which also leads to a different set of coefficients for each center frequency.

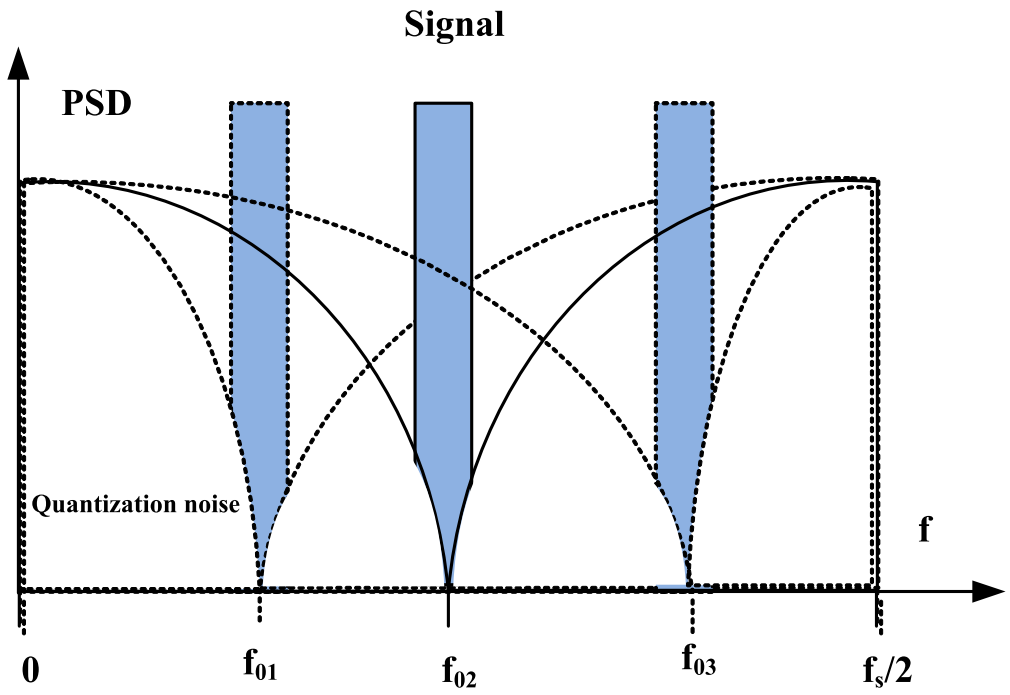

Fig. 3.4: Output Power Spectral Density (PSD) of Conventional Tunable Bandpass $\Delta\Sigma$ ADCs

In the work presented in [Gupta12], the sampling frequency is fixed in order to avoid any variation in the normalized loop delay (t_d/T_s), but since the normalized center frequency f_0/f_s is still variable. This architecture also requires tuning of the $\Delta\Sigma$ coefficients for each center frequency.

It is clear that tuning of the band-pass $\Delta\Sigma$ ADC center frequency, f_0, usually requires a corresponding tuning of feedback or feed forward coefficients of the $\Delta\Sigma$ ADC. Tuning feed forward, feedback or Finite-Impulse Response Digital-to-Analog-Converter (FIRDAC) coefficients in a continuous-Time $\Delta\Sigma$ ADC loop is rather difficult. It usually leads to a more complex architecture, a higher power consumption and a limited tuning range. Furthermore, using a normalized center frequency f_0/f_s ratio different than 1/4 or 3/4 leads to have complex and high power Digital Down Conversion (DDC) mixer and decimation filter [Schreier05].

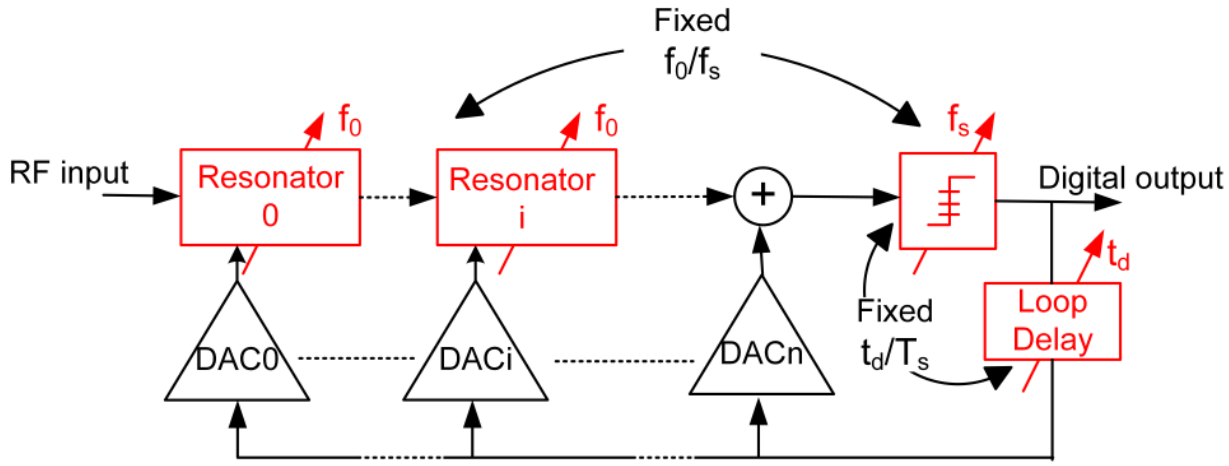

Fig. 3.5: Proposed Architecture using Constant $\Delta\Sigma$ ADC Coefficients (Constant Normalized Loop Delay (t_d/T_s), Constant Normalized Center Frequency f_0/f_s)).

3.4 Proposed Tunable $\Delta\Sigma$ ADC

Fig. 3.5 shows the proposed tunable $\Delta\Sigma$ ADC architecture [Aboushady20]. The proposed tunable $\Delta\Sigma$ has a constant set of coefficients based on loop delay variation control techniques. In addition to exhibiting better performance in terms of tunable operating frequency. It also has constant $f_0/f_s = 1/4 or 3/4$, as shown in Fig. 3.6, to have simple and low power of digital mixer and decimation filters.

By varying the sampling frequency, $f_s = 1/T_s$, the major problem is that the normalized loop delay t_d/T_s of the modulator changes. This normalized loop delay variation affects the performance of modulator, as shown in Fig. 3.7. It can be seen that the $\Delta\Sigma$ ADC with a $1.5T_s$ loop delay does not suffer from from SNR degradation for loop delay in the range from $1.2T_s$ to $1.7T_s$. Moreover, the Noise and Signal Transfer Functions are still the same for loop delay within this acceptable range. Thus, we propose a technique to maintain the normalized loop delay for all sampling frequencies to be within the acceptable range. This loop delay control technique is discussed in detail in section 3.4.2.

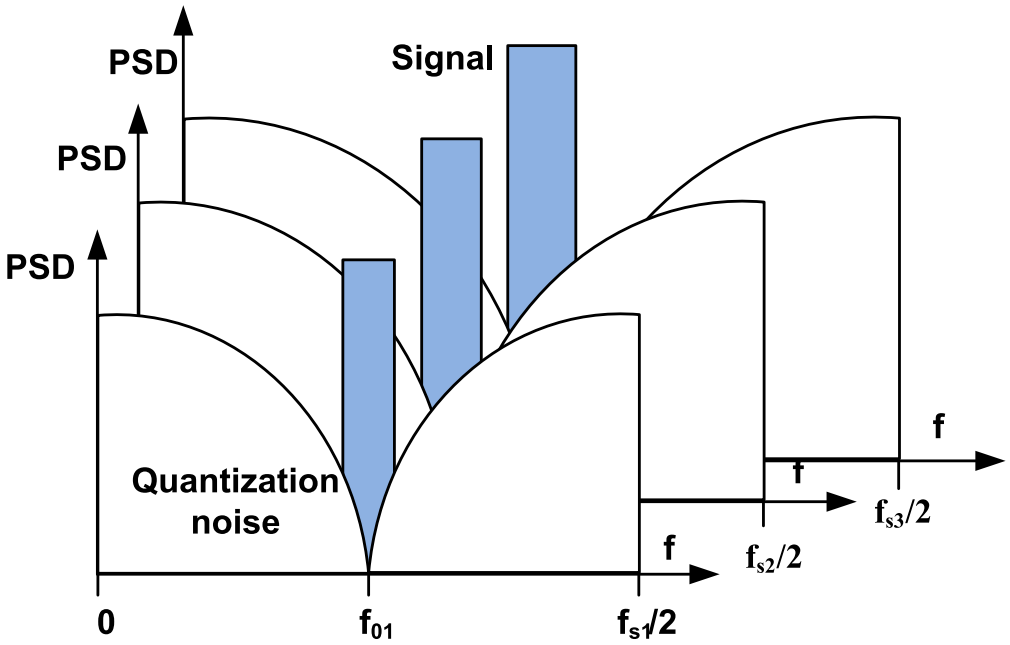

Fig. 3.6: Output Power Spectral Density (PSD) of Proposed Tunable Bandpass $\Delta\Sigma$ ADC

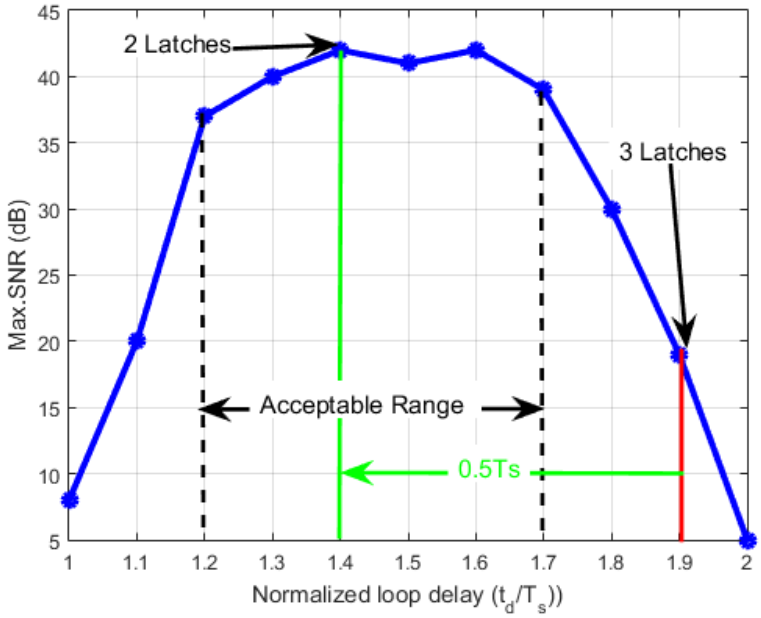

Fig. 3.7: SNR with Loop Delay Variation(Sampling Frequency 9.0GHz).

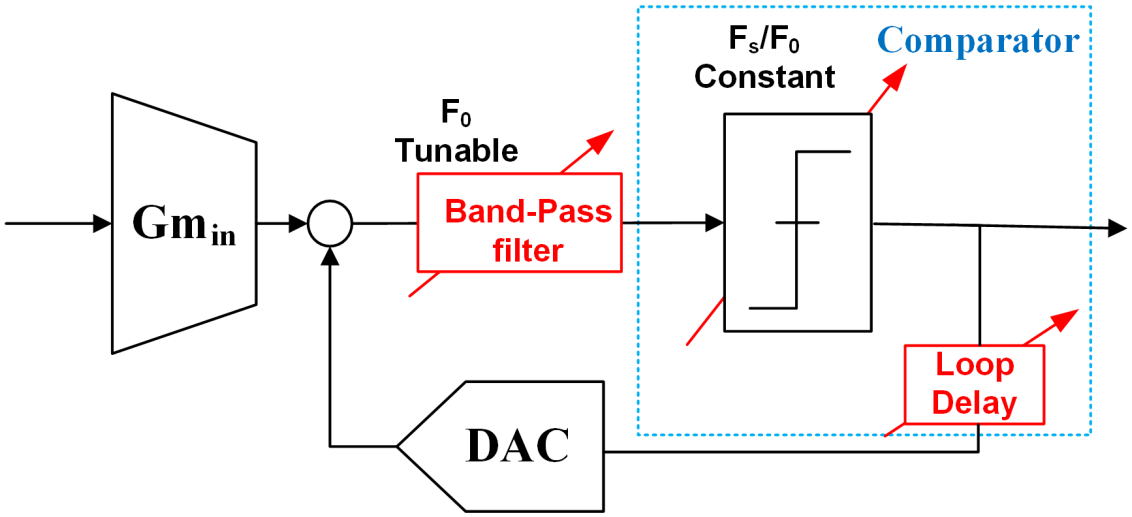

Fig. 3.8: Architecture of the 2^{nd} Order Tunable Band-Pass $\Delta\Sigma$ ADC.

3.4.1 Architecture of the 1.5-to-3.0GHz Tunable RF $\Delta\Sigma$ ADC

The system level design of this architecture is based on the equivalence between the Discrete Time (DT) to Continuous Time (CT) with feedback FIRDAC using the modified Z -transform technique as in [Aboushady02]. The single-bit DT $\Delta\Sigma$ modulators can be design using MATLAB® Schreier toolbox [Schreier99].

The ADC is designed for tunable input signal from 1.5 to 3.0GHz and, it is clocked at 4 or 4/3 times these frequencies for oversampling and subsampling respectively. This simplifies the down-conversion of the ADC output, as the LO sinusoidal signal becomes a series of $\{1, 0, -1, 0\}$ [Cherry00]. As illustrated in Fig. 3.8, the $\Delta\Sigma$ ADC is based on a 2^{nd} order band-pass filter, single-bit quantizer and Non-Return to Zero digital to analog converter (NRZ DAC).

The ADC specifications can be summarized in the following points:

- Type: 2^{nd} order band-pass LC-based $\Delta\Sigma$ ADC.
- Center frequency: $f_o = 1.5 - to - 3.0\,GHz$.
- Sampling frequency: $f_s = 4\,f_o = 6.0 - to - 12.0\,GHz$ for oversampling.
  $f_s = 4/3\,f_o = 2.0 - to - 4.0\,GHz$ for subsampling.

- Oversampling Ratio: $OSR = 64$.
- Bandwidth:$BW = f_s/(2\,OSR) = 47 - to - 93\,MHz$ for oversampling.
  $BW = f_s/(2\,OSR) = 16 - to - 31\,MHz$ for subsampling.
- Loop delay: $t_d = 1.5\,T_s$.

3.4.2 Proposed Comparator with Loop Delay Control

The classical comparator composed of 4 cascaded latches has ideally, $1.5T_s$ delay, as illustrated in Fig. 3.9. It can be seen that each two cascaded latches are toggled, i.e. the latch is in the holding phase when the succeeding latch is in the tracking phase and vice-versa. The delay of each two cascaded latches is a half clock cycle ($T_s/2$) in case of $\tau_{reg} < 0.5T_s$ as shown in Fig. 3.10. Thus, the ideal loop delay of classical comparator compose of N toggled latches.

$$t_d = (N-1)\,T_s/2 \tag{3.1}$$

After circuit implementation, it was found that the actual loop delay exceeds the value predicted by Equation 3.1 by t_{latch}, as illustrated in Fig. 3.10. The practical loop delay can be defined by the following Equation.

$$t_d = (N-1)\,T_s/2 + t_{latch} \tag{3.2}$$

$$t_{latch} = \tau_{last\,latch} + t_{inverter} + t_{DAC}$$

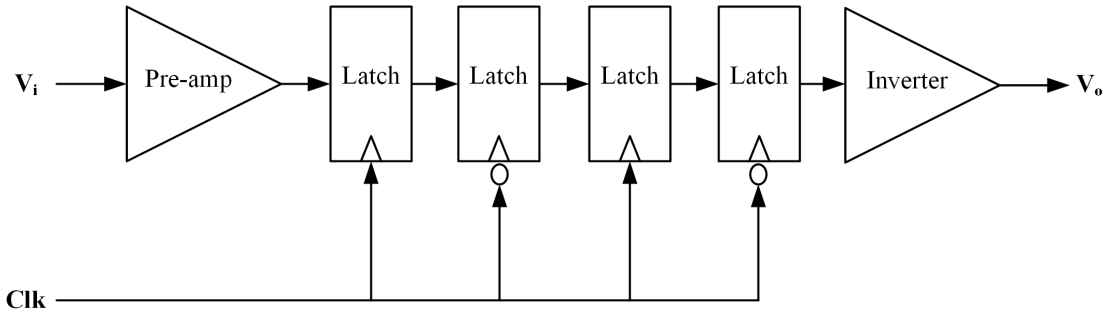

Fig. 3.9: Classical Comparator Block Diagram.

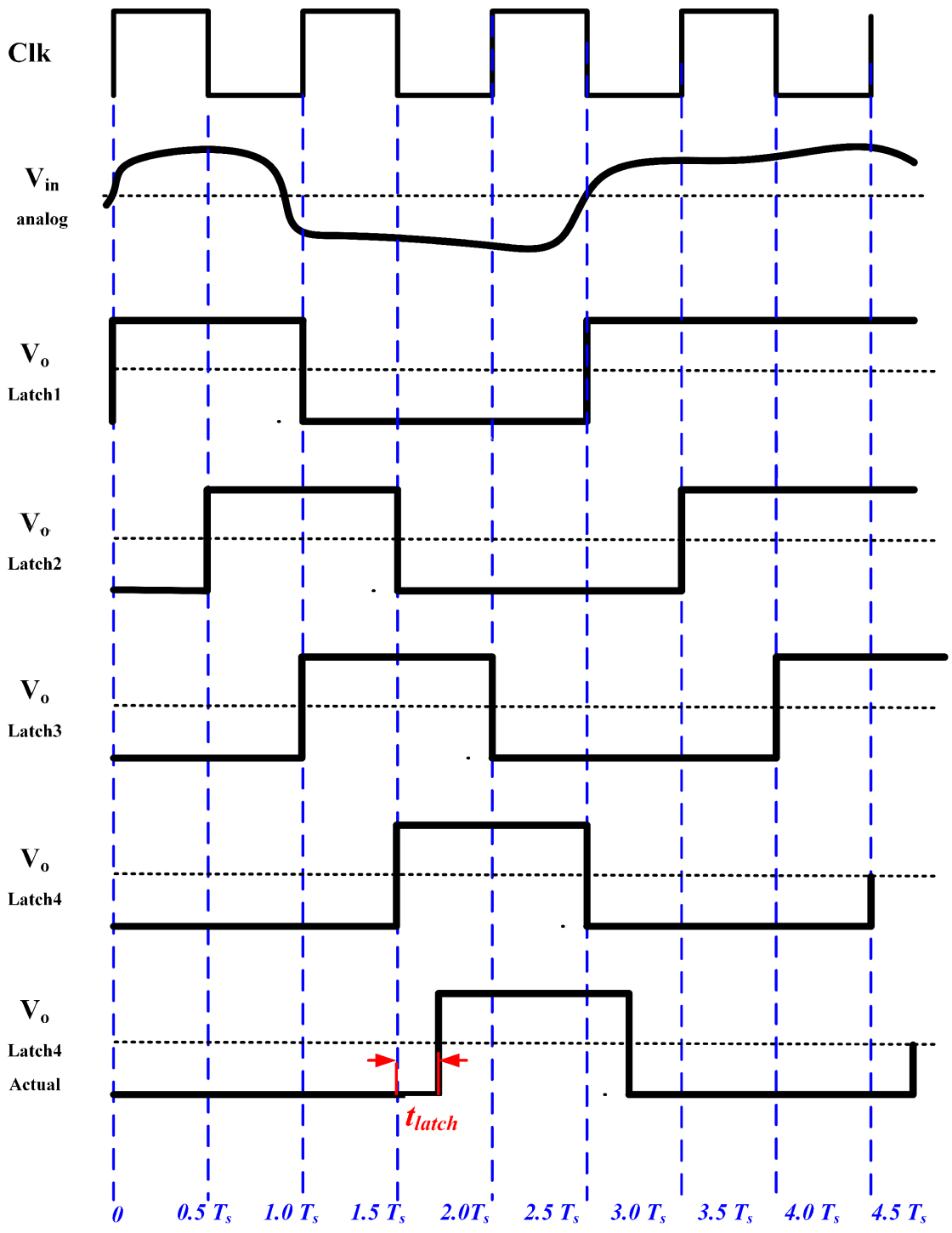

Fig. 3.10: Ideal Comparator Waveforms.

Table 3.1: Normalized Loop Delay (t_d/T_s) versus Number of Toggled Latches.

	Normalized loop delay (t_d/T_s)		
Sampling Frequency (GHz)	2 Latches	3 Latches	4 Latches
2.0	0.7	1.2	1.7
3.0	0.8	1.3	1.8
4.0	0.9	1.4	1.9
5.0	1.0	1.5	2.0
6.0	1.1	1.6	2.1
7.0	1.2	1.7	2.2
8.0	1.3	1.8	2.3
9.0	1.4	1.9	2.4
10.0	1.5	2.0	2.5
11.0	1.6	2.1	2.6
12.0	1.7	2.2	2.7

where $\tau_{last\,latch}$ is the regeneration time of the last latch, $t_{inverter}$ is the time delay due to inverter of the comparator, t_{DAC} is the time delay due to DAC.

The first part of the loop delay i $(N-1)\,T_s/2$ is well-defined, constant and independent of sampling period (T_S). However, the second part t_{latch} is generally uncontrollable, undesirable and strongly dependent on process parameters. Moreover, this t_{latch} is not constant with respect to the variable sampling period ratio (t_{latch}/T_S is not constant). Where, t_{latch} is varies from $0.2T_S$ to $1.2T_S$ when the sampling frequency change from 2.0GHz to 12.0GHz.

As illustrated in Fig. 3.7, circuit level simulations for an OSR of 64, there is little SNR degradation when the normalized loop delay is between $1.2T_s$ and $1.7T_s$. Thus, we should have techniques to compensate the normalized loop delay variation and maintain it within this acceptable range for all sampling frequencies. However, by varying the sampling frequency from 2.0 to 12.0GHz, the normalized loop delay changes from $1.7T_s$ to $2.7T_s$ when we have 4 toggled latches in the comparator, while it varies from $1.2T_s$ to $2.2T_s$ when we have 3 latches in the comparator, it varies from $0.7T_s$ to $1.7T_s$ when we have 2 latches in the comparator, as shown in Table 3.1. It is clear that there is no fixed number of latches that

satisfies the acceptable loop delay variation range.

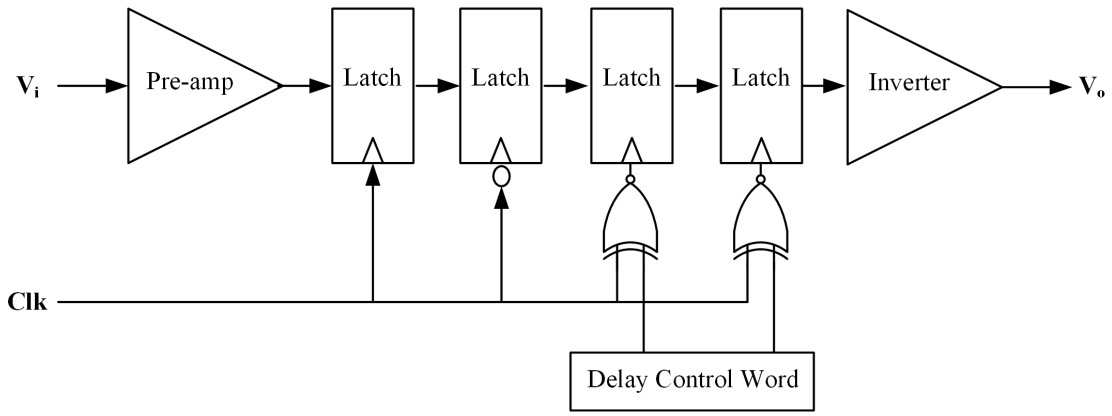

Fig. 3.11: Proposed Comparator Block Diagram.

We propose the loop delay control technique shown in Fig. 3.11. The last two latches are programmable which means that we can change the clock polarity for this two latches. Thus, we can have variable number of toggled latch 2,3, or 4.
In this ADC, we use a programmable loop delay by using 4 latches in the comparator when f_s is equal to 2.0GHz, 3 latches when f_s is less than of equal to 7.0GHz and 2 latches when f_s is higher than 7.0GHz. The delay provided by each toggled latch is $T_s/2$.

3.4.3 Front-end Implementation in CMOS 65nm

The proposed tunable bandpass delta-sigma ADC was fabricated in CMOS 65nm [Sayed16], as shown in Fig. 3.12. The chip measured performance proved to be attractive for spectrum sensing:

- **Center frequency, F_o Tuning Range**: 1.5 – 3.0 GHz
- **Sampling Frequency, F_s** : 6.0 – 12.0 GHz
- **Effective Number of Bits ($ENOB$)**: 8.2 Bits
- **Bandwidth**: 5 MHz
- **Low Power**: 26 $\sim$ 33 mW

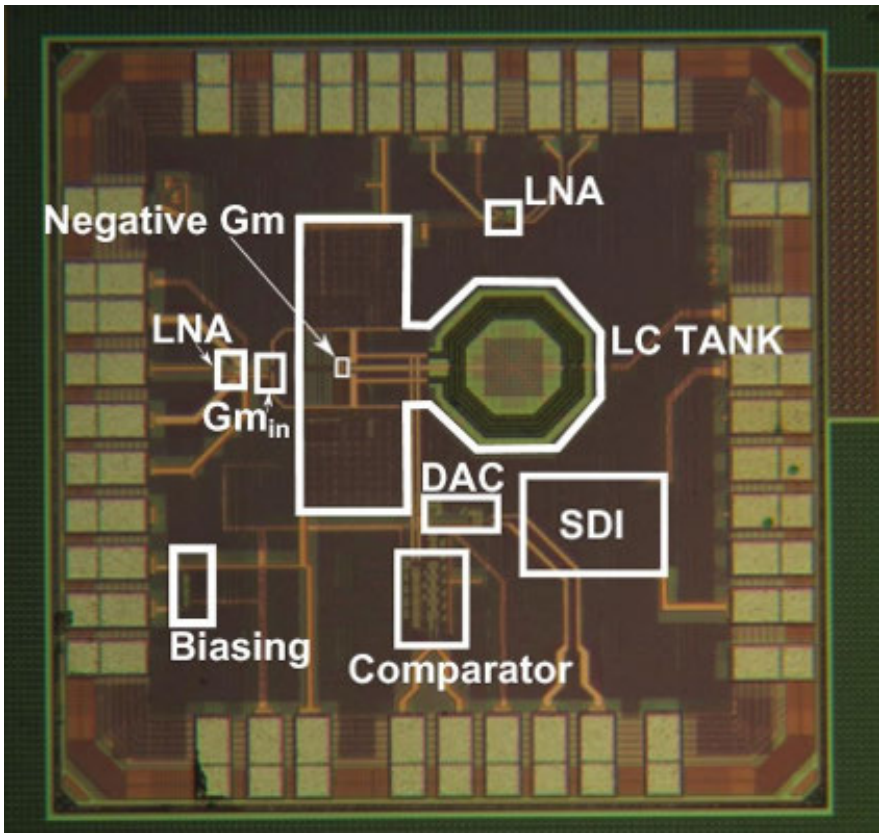

Fig. 3.12: Micrograph of the Fabricated Chip in CMOS 65nm [Sayed16].

- **Small Area**: 0.3 mm2

3.5 Conclusions

In this chapter, we presented an efficient realization of a tunable RF band-pass $\Delta\Sigma$ ADC with wide tuning range. Bandpass RF ADC based architectures were introduced. A tunable band-pass $\Delta\Sigma$ ADCs architecture was proposed. The proposed architecture was fabricated and the measured performance are well suited for spectrum sensing applications.

Chapter 4

Complete Spectrum Sensing System

4.1 Introduction

In this chapter, section 4.2 explain important parameters and metrics for energy detection spectrum sensing. Section 4.3 illustrates the response of a nonlinear system to a multi-channel input. The testing scenarios and hypotheses for available and busy cases are described in section 4.4. The threshold setting methodology is explained in section 4.5. Impact of circuit nonlinearity on the energy detection performance is shown by simulation results in section 4.6. Section 4.7 concludes the chapter.

4.2 Energy Detection Spectrum Sensing

In spectrum sensing, a decision should be taken regarding the availability of a specific frequency band. It's a likelihood problem following Neyman-Pearson test of two hypotheses $\mathcal{H}_0$ and $\mathcal{H}_1$ [Neyman33]. The decision is made to reject $\mathcal{H}_0$ in favor to $\mathcal{H}_1$ if the test resulted in a result higher than a specific threshold value. Energy detection spectrum sensing takes decision based on the energy contained within the band of interest. The available hypothesis $\mathcal{H}_0$ is the case when only noise is received in the band of interest, whether the busy hypothesis $\mathcal{H}_1$ is the case when primary user and noise are received. Equation 4.1 and Figure 4.1 describe these hypotheses mathematically and graphically.

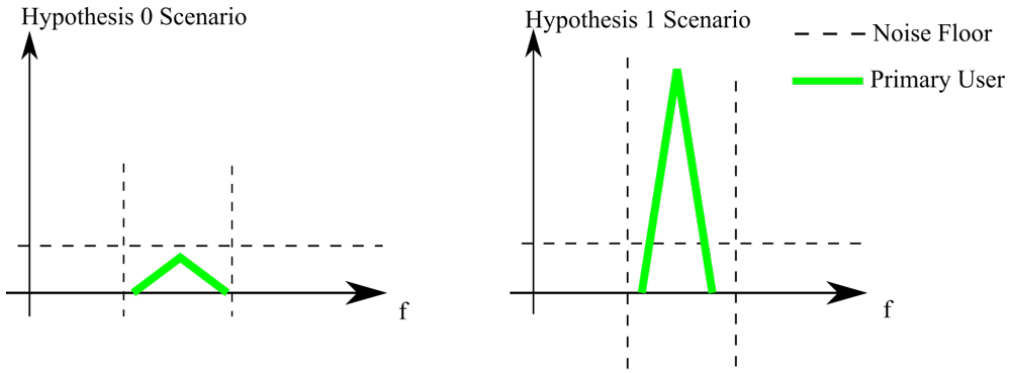

Fig. 4.1: Spectrum Example under Hypotheses $\mathcal{H}_0$ and $\mathcal{H}_1$

$$x(k) = \begin{cases} n(k), & \mathcal{H}_0 \\ n(k) + s(k), & \mathcal{H}_1 \end{cases} \tag{4.1}$$

Two important probabilities are defined for spectrum sensing performance evaluation. First, probability of detection, which is the probability of deciding that the band of interest is unavailable under hypothesis $\mathcal{H}_1$, Equation 4.2. This probability is desired to be as high as possible. Second, probability of false alarm, which is the probability of deciding that the band of interest is unavailable under hypothesis $\mathcal{H}_0$, Equation 4.3. This probability is desired to be as low as possible. Note that, given the two different conditions, the two probabilities are not complementary.

$$P_D = prob\left(\hat{E} \leq \lambda_E | \mathcal{H}_1\right) \tag{4.2}$$

where $\hat{E}$ is the energy received within the band of interest, and λ_E is the energy test threshold.

$$P_{FA} = prob\left(\hat{E} \leq \lambda_E | \mathcal{H}_0\right) \tag{4.3}$$

The probability of false alarm is affected directly by the energy threshold, λ_E. The energy threshold in return is affected by the noise floor and distribution within the band of interest, and the number of samples contributing to the calculation of received energy. The reason that the number of samples is crucial is that it affects the distribution profile of the noise

energy. In this work, a additive white Gaussian noise channel is assumed. Hence, the noise energy distribution is the result of summation of squared Gaussian distributed variables. That resulting distribution known as chi-squared, χ^2_N, where N is the number of samples contributing to received energy calculation. According to central limit theorem, as N increases the chi-squared distribution can be approximated to a Gaussian distribution. This really simplifies the analytical solution of the performance evaluation.

The probability of detection is not only affected by the energy threshold, but more influenced by the signal-to-noise-ratio (SNR) of the signal received. It is desirable to have acceptable probability of detection even under stringently low primary users SNR environment.

To evaluate the performance of spectrum sensing system graphically, curves are normally plotted. The receiver operation characteristics (ROC) curve, and the probability of detection curve. The ROC is a graph showing the probability of false alarm against the probability of detection plotted at a specific SNR. The other set is a graph of probability of detection against SNR plotted for a specific P_{FA}.

4.3 Non-Linear System Response to Multi-Channel Input

Having a multi channel received by a nonlinear system results in intermodulation harmonics components at center frequencies that depends on how much those multi channels are separated. Those extra components highly affects the performance of spectrum sensing receiver. They may cause the sensing decision to be incorrectly busy and increase the false alarm probability. If the false alarm probability to be held fixed at a specific value, then the extra components will cause the detection probability to drop.

A general differential low-noise-amplifier (LNA), which is the main nonlinearity source in an RF $\Delta\Sigma$ based receiver as shown in Fig. 4.2, have this input-output relationship:

$$y = a_1 x + a_3 x^3 \tag{4.4}$$

where y is the LNA output, x is the LNA input, a_1 is the DC gain, only the third harmonic is considered (because the LNA has differential output and second harmonic is negligible),

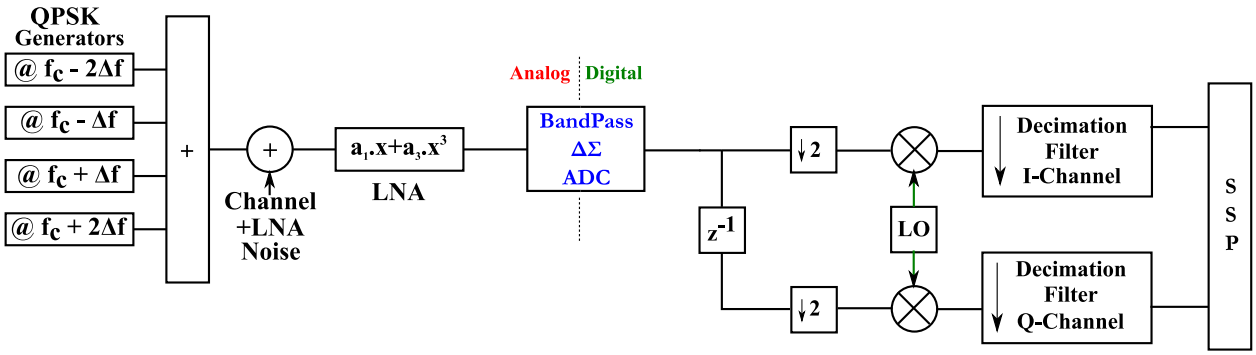

Fig. 4.2: Receiver Model for Simulation with Nonlinear LNA to study its effect on the Performance.

and a_3 is related to a_1 via:

$$a_3 = \frac{4a_1}{3V_{IIP_3}^2} \tag{4.5}$$

where $V_{IIP_3} = 10^{(IIP_3/20)}$

Now, we will check the output of the LNA in two cases, three channel input and four channel input. In case of 3 channel input, as shown in Fig. 4.3, A is the input amplitude, f_c is the center frequency of the band, and Δf is the frequency deviation between different channels, we will have

$$x = A\left(sin(2\pi f_c t) + sin(2\pi(f_c + \Delta f)t) + sin(2\pi(f_c + 2\Delta f)t)\right) \tag{4.6}$$

$$\begin{aligned} y = {} & 0.75a_3A^3sin(2\pi(f_c - 2\Delta f)t) + 2.25a_3A^3sin(2\pi(f_c - \Delta f)t) \\ & + (a_1A + 4.5a_3A^3)sin(2\pi f_c t) + (a_1A + 5.25a_3A^3)sin(2\pi(f_c + \Delta f)t) \\ & + (a_1A + 4.5a_3A^3)sin(2\pi(f_c + 2\Delta f)t) + 2.25a_3A^3sin(2\pi(f_c + 3\Delta f)t) \\ & + 0.75a_3A^3sin(2\pi(f_c + 4\Delta f)t) \end{aligned} \tag{4.7}$$

In case of 4 channel input, as shown in Fig. 4.4, we will have

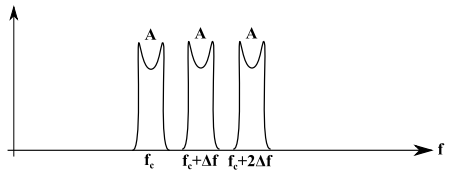

(a) Three Generalized Signals Input to a Non-Linear System

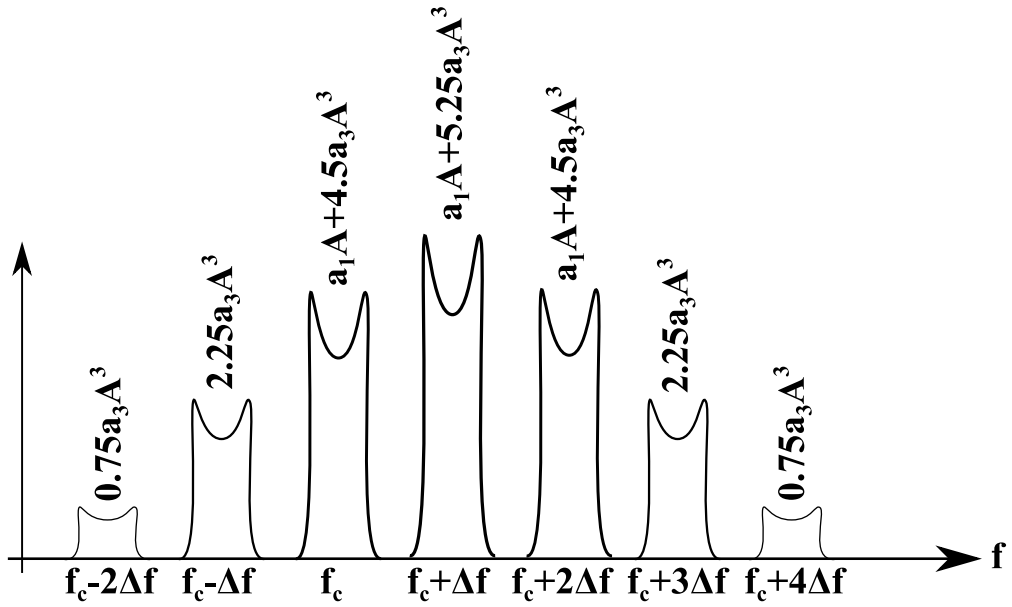

(b) Three Generalized Signals Output from a Non-Linear System

Fig. 4.3: Nonlinearity Effect on a Three Channel Input

$$x = A\left(sin(2\pi f_c t) + sin(2\pi(f_c + \Delta f)t) + sin(2\pi(f_c + 2\Delta f)t) + sin(2\pi(f_c + 3\Delta f)t)\right) \quad (4.8)$$

$$\begin{aligned} y = {} & 0.75a_3A^3 sin(2\pi(f_c - 3\Delta f)t) + 2.25a_3A^3 sin(2\pi(f_c - 2\Delta f)t) \\ & + 4.5a_3A^3 sin(2\pi(f_c - \Delta f)t) + (a_1A + 7.5a_3A^3)sin(2\pi f_c t) \\ & + (a_1A + 9a_3A^3)sin(2\pi(f_c + \Delta f)t) + (a_1A + 9a_3A^3)sin(2\pi(f_c + 2\Delta f)t) \\ & + (a_1A + 7.5a_3A^3)sin(2\pi(f_c + 3\Delta f)t) + 4.5a_3A^3 sin(2\pi(f_c + 4\Delta f)t) \\ & + 2.25a_3A^3 sin(2\pi(f_c + 5\Delta f)t) + 0.75a_3A^3 sin(2\pi(f_c + 6\Delta f)t) \end{aligned} \quad (4.9)$$

The significance of that results is to show the severity of the nonlinearity effect, the number of extra intermodulation distortion components, the frequency position of those components,

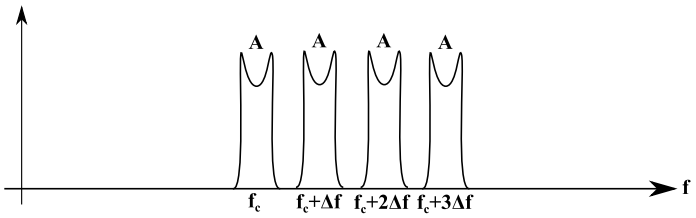

(a) Four Generalized Signals Input to a Non-Linear System

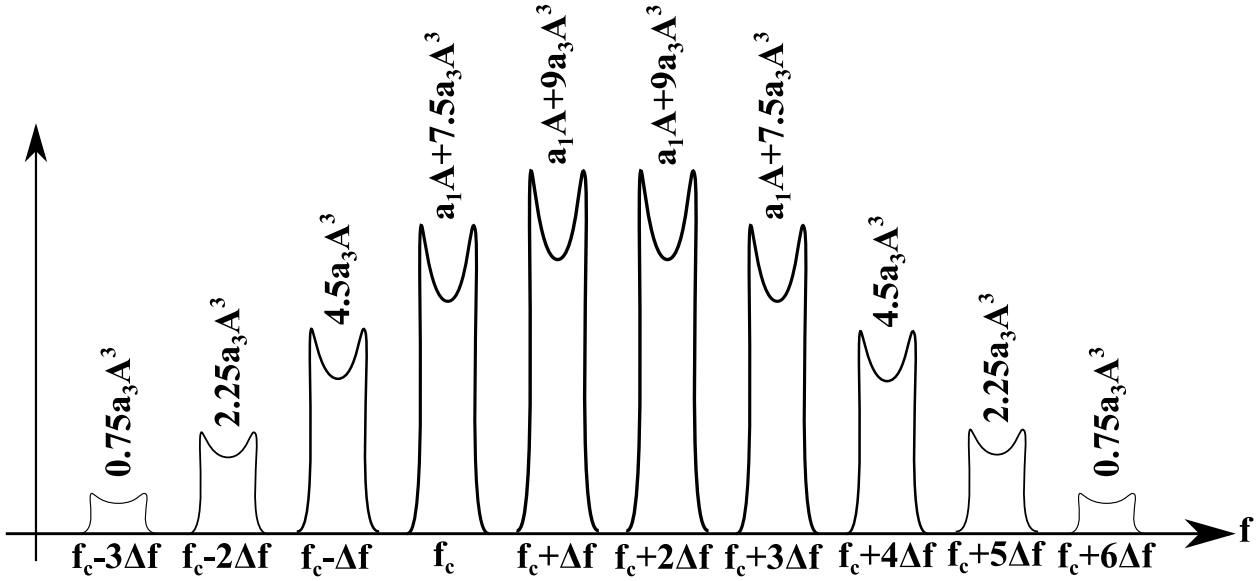

(b) Four Generalized Signals Output from a Non-Linear System

Fig. 4.4: Nonlinearity Effect on a Four Channel Input

and more importantly the amplitude of those components as it will directly affect the energy calculated with the sensed channel or band.

4.4 Testing Hypotheses and Scenarios

As mentioned before, there are two main scenarios. The available scenario; where the band is considered available to be utilized, and the busy scenario; where the band is left unused. Referring to Fig. 4.2, our assumptions are as follows: a band of 30MHz around $f_c = 1GHz$ is assumed to be the band of interest. The nonlinearity of the low-noise amplifiers is chosen $IIP_3 = -22dBm$. The second-order Delta-Sigma ADC is clocked at $f_s = 4f_0 = 4GHz$, oversampling ratio $OSR = 64$, means that OSR=64 is assumed for the $\Delta\Sigma$ modulator and

sampling frequency, $f_s = 4GHz$). The spectrum is shown by fast-fourier transform with 2^19 points and with normalized amplitude. The transmitted signal to establish hypothesis 0, $\mathcal{H}_0$, consists of three adjacent channels and the sensed channel is the first band adjacent to those three occupied channels, as shown in Fig. 4.5. In this way, in a nonlinear system we will have an intermodulation harmonic component that will either increase P_{FA} or decrease P_D. To establish hypothesis 1, $\mathcal{H}_1$, the transmitted signal consists of four channels, and the sensed channel lies onto one of those channels.

Fig. 4.6 and Fig. 4.7 show the simulation results of the spectrum at the $\Delta\Sigma$ ADC input. The results are in accordance with equations 4.7 and 4.9 for the mentioned two scenarios with nonlinear LNA response.

4.5 Threshold Setting Methodology

An energy threshold should be set to decide whether the desired frequency band is busy or available. Fig. 4.8 shows a flow chart of the threshold setting along with plotting the

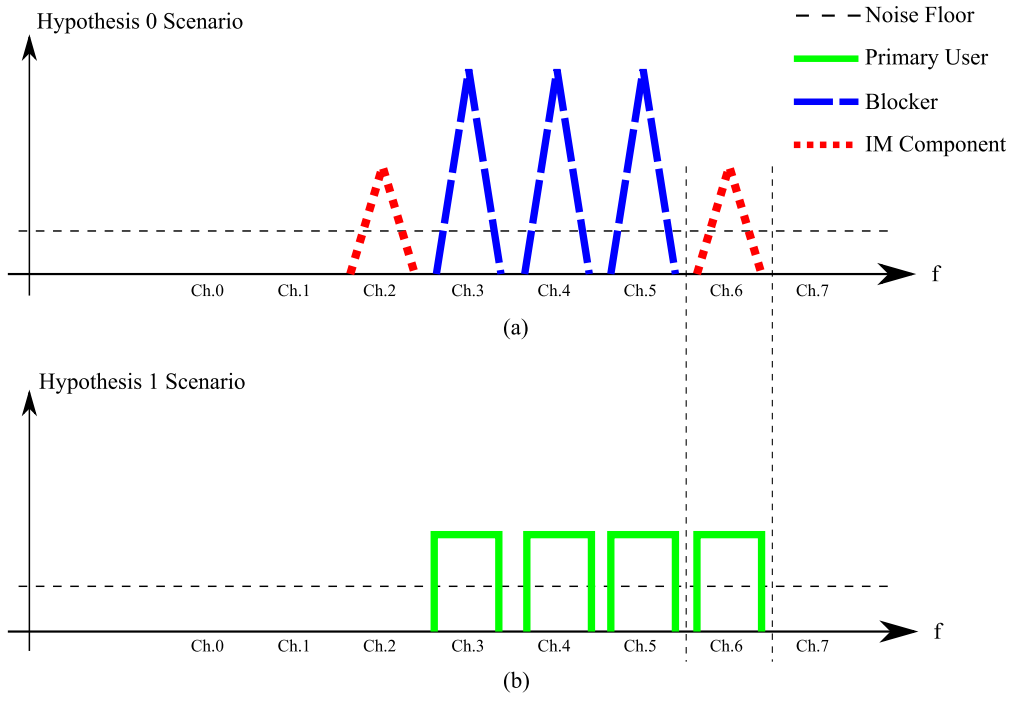

Fig. 4.5: Available and Busy Scenarios to Exploit Nonlinearity Effect.

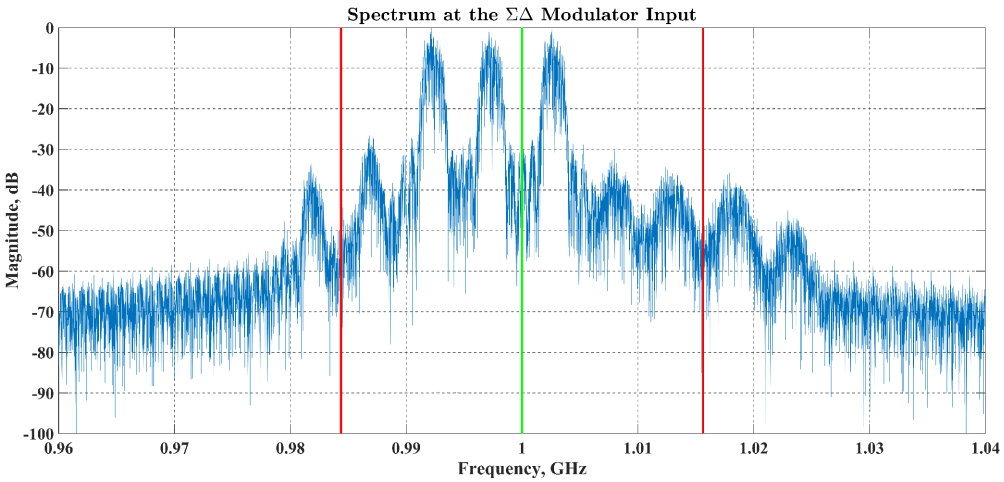

Fig. 4.6: Example of Available Scenario at $\Delta\Sigma$ Modulator input. Number of FFT points is 2^{19}, Nonlinear LNA, $IIP_3 = -22dBm$.

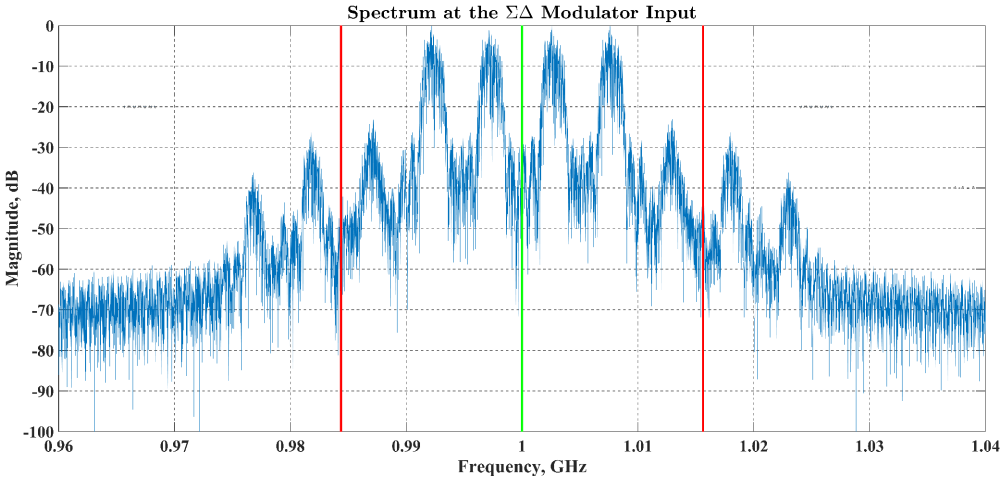

Fig. 4.7: Example of Busy Scenario at $\Delta\Sigma$ Modulator input. Number of FFT points is 2^{19}, Nonlinear LNA, $IIP_3 = -22dBm$.

two evaluation curves. The input parameters, which should be prior to evaluation are: the SNR range, the assumed channel noise level, the assumed nonlinearity specifications, and the desired probability of false alarm. Two sets of acquisition has to be done. One set of acquisition under scenario $\mathcal{H}_0$ that contribute to P_{FA} choice and threshold setting. The other set is under scenario $\mathcal{H}_1$ and contributes to determine the detection probability. The number of acquisitions, L, in every set will determine the resolution, $1/L$, of the determined proba-

bility. So for 1% resolution every set has, at least, 100 different acquisition. The procedure is highly affected by the number of samples acquired and taken into account for energy calculation [Umar14]. In this work, for each channel, the number of samples is at least 128. The set of acquisition under $\mathcal{H}_0$ is first processed to calculate the energy. Those energy values are sorted in ascending order, E_{Ns}. P_{FA} expresses the ratio of those values to be found higher than the threshold - and hence assumed to be busy band and cause a false alarm. So if the number of energy values is L, then the energy value with an index of $(1 - P_{FA}) * L$ in the sorted values should be taken as the threshold. Fig. 4.9 shows an example of calculating probability of detection, we start from the required $P_{FA} = 10\%$, which make the energy value with index 90 chosen to be the energy threshold. then the sorted energy values of the acquisitions under $\mathcal{H}_1$, E_U, is searched for the nearest value, energy with index 8 in this example. Finally, we calculate the $P_D = 100 - 8 = 92\%$. In order to plot P_D vs. SNR, the set of acquisitions under $\mathcal{H}_1$ is repeated for each SNR value. For the ROC, we sweep P_{FA} and for each value the threshold is reset and a new P_D value is calculated. In order to show more clearly the impact of circuit nonlinearity, a third metric is plotted. That metric show the change of P_{FA} with different values of blocker signal SNR. For each value of blocker SNR the set of acquisitions under $\mathcal{H}_0$ is repeated.

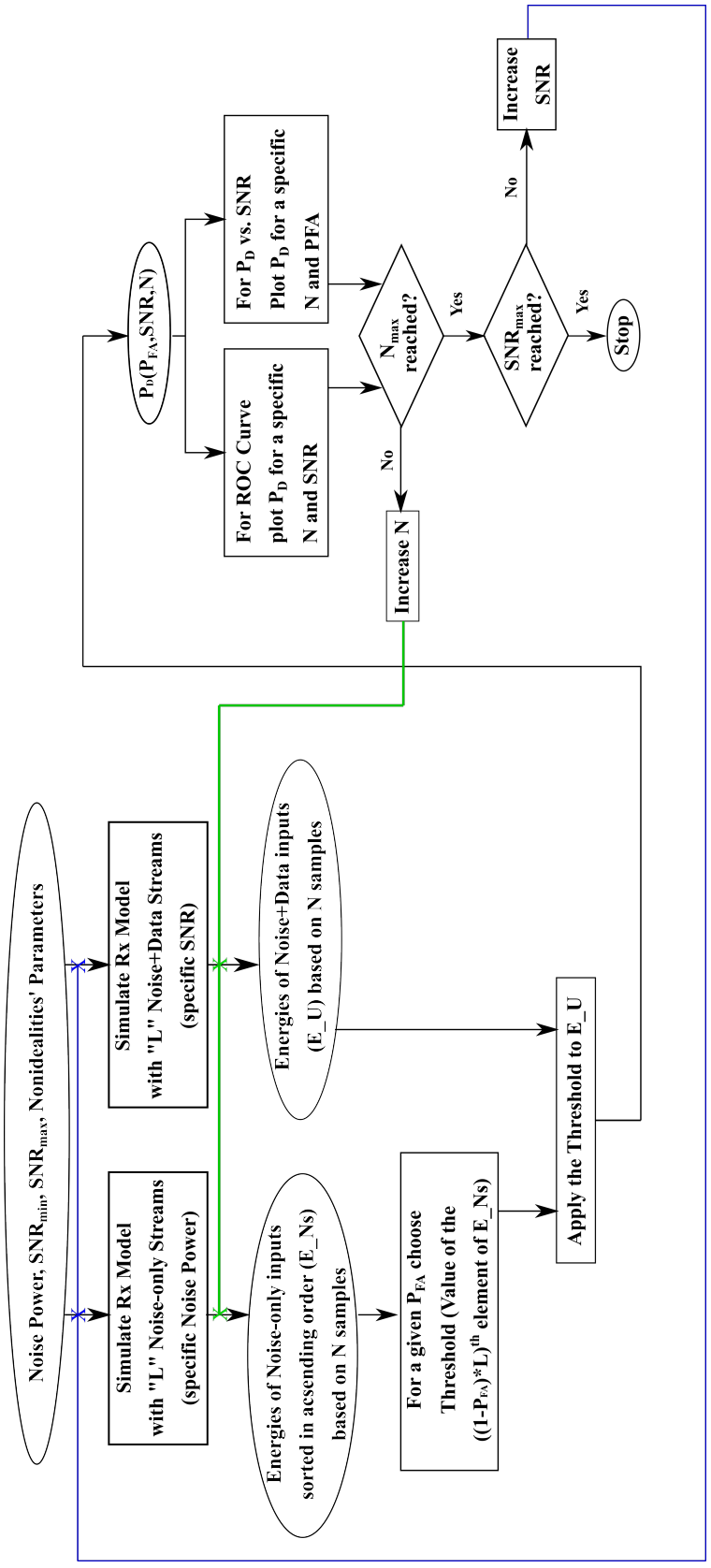

Fig. 4.8: Flow Chart to Set the Energy Threshold and to Plot the Evaluation Curves

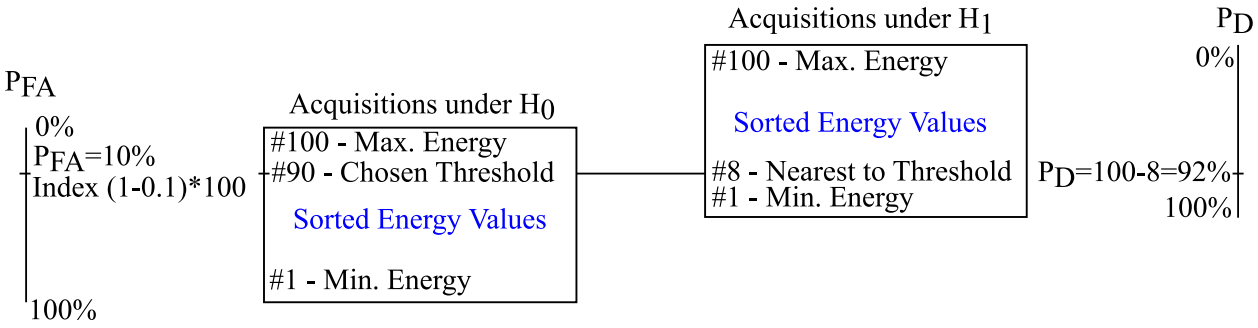

Fig. 4.9: Example showing the calculation of detection probability starting from a specific P_{FA}.

4.6 Simulation Results

4.6.1 P_D vs. SNR

The P_D vs. SNR curve is plotted for a fixed false alarm probability. For each single value of SNR, the system is simulated with at least $L = 100$ input stream under each one of the two hypotheses. Hence, the simulations required for this curve is highly time-consuming. Due to the modeled nonlinearity, the existence of extra components in the spectrum results in increasing the chosen energy threshold. This increase in the threshold, in turn, results in requiring higher SNR of the received PU signal to get the same probability of detection. As shown in Figure 4.10 the nonlinear system (in magenta) shows worse performance.

4.6.2 P_{FA} vs. SNR of Blocker Signals

This curve is introduced only with the study of RF Impairments on Spectrum Sensing. The extra component that affected the performance were the result of adjacent channels. In this graph, the false alarm probability is plotted against the power level of those causing channels (blockers). The nonlinear curve (in magenta), Figure 4.11 shows that the P_{FA} is 22% at the same blocker level that caused the linear system to have 10% of P_{FA}.

4.6.3 ROC

we mentioned before that the usual requirements of a spectrum sensing system is to have higher than 90% of detection probability while having less than 10% of false alarm prob-

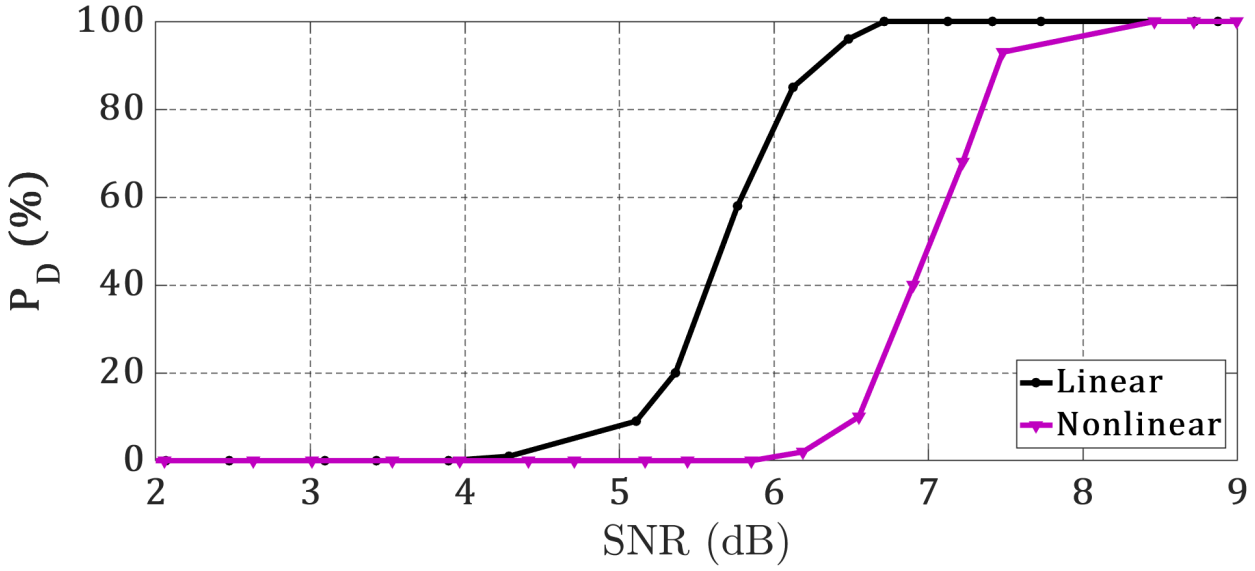

Fig. 4.10: P_D vs SNR (dB) of PU for Linear and Nonlinear Systems. LNA $IIP_3 = -22dBm$ The SNR of the blocker is fixed and the desired $P_{FA} = 10\%$.

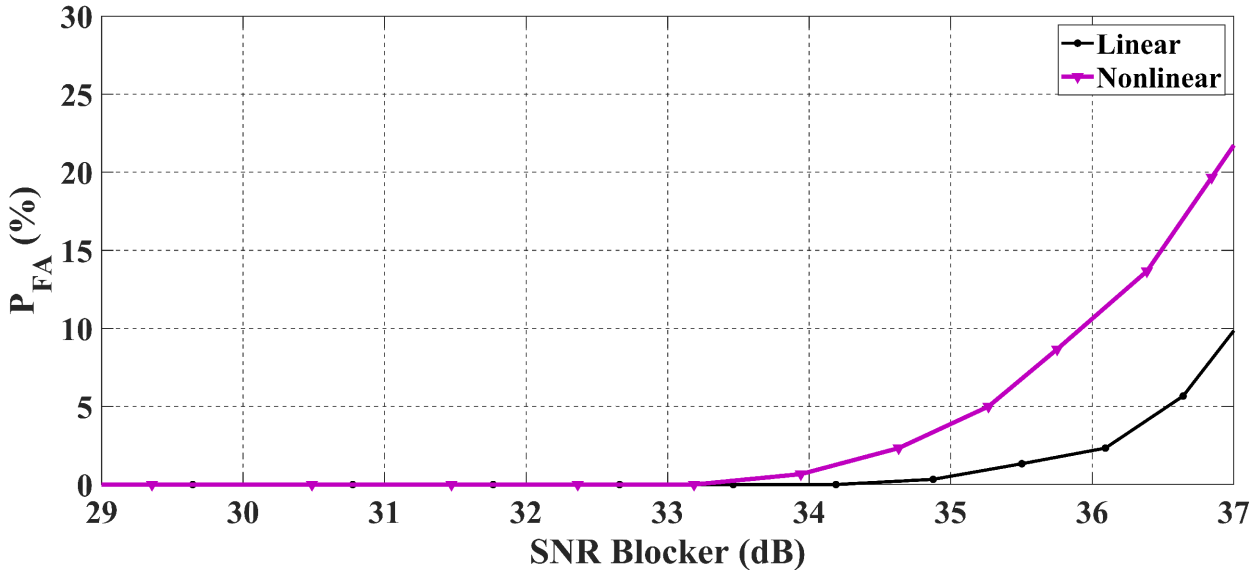

Fig. 4.11: Nonlinearity Effect on P_{FA} when a blocker signal is presented. Fix $P_D = 90\%$. LNA $IIP_3 = -22dBm$

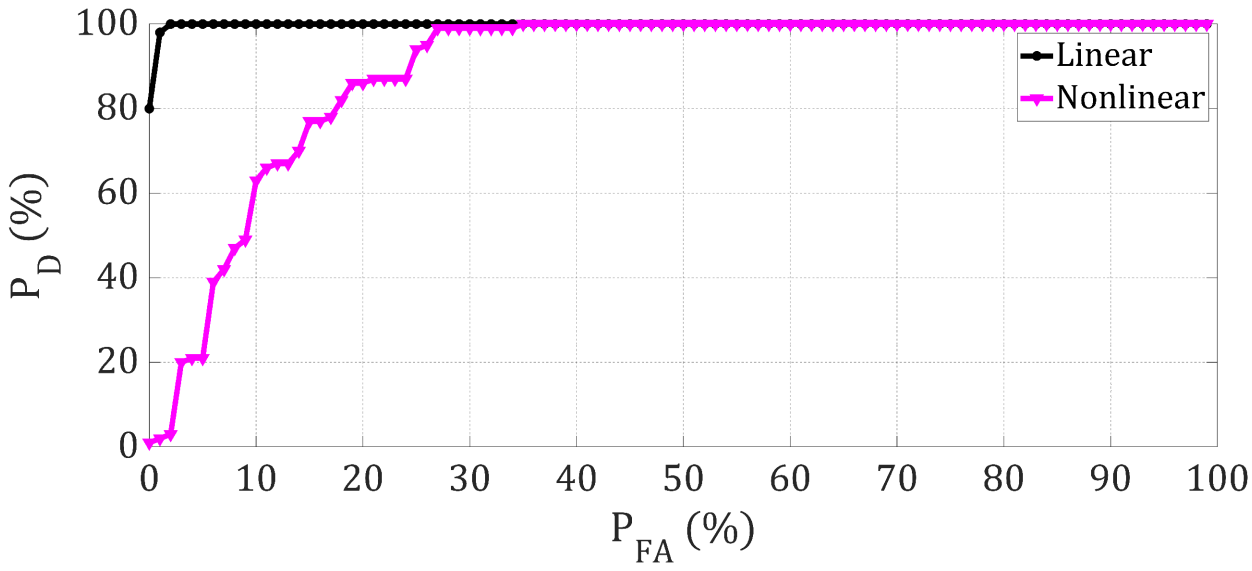

Fig. 4.12: ROC of Ideal and Nonlinear Systems, SNR fix to 5 dB. LNA $IIP_3 = -22dBm$

ability. Figure 4.12 shows that the linear system performance is achieving that while the nonlinear system curve (in magenta) get an unacceptable 56% of detection probability at 10% of false alarm probability.

4.7 Conclusions

In this chapter, the system design of the proposed energy detection spectrum sensing is presented. Energy detection hypotheses and metrics were introduced. The nonlinear system response was discussed. A suitable testing scenarios that emphasize the nonlinearity effect on the performance were chosen. We explained a threshold setting methodology. And finally simulation results shown the impact of circuit nonlinearity on the performance, evaluated by three curves.

Chapter 5

Spectrum Sensing Circuit Design and Implementation

5.1 Introduction

In chapter 3, we mentioned that the analog RF front end (AFE) of a tunable bandpass $\Sigma\Delta$ ADC based receiver has been implemented in a 65nm CMOS technology. In order to implement a complete spectrum sensing receiver with the architecture proposed in chapter 4, a digital backend (DBE) needs to be implemented and process the output of the AFE chip. In this chapter, we present the implementation of the DBE of spectrum sensing receiver on FPGA. The chapter is organized as follows: section 5.2 presents the architecture of the implemented DBE, The down-conversion mixer and decimation filter implementation and validation is discussed in section 5.3. Section 5.4 presents the spectrum sensing processor implemented on the FPGA. Design optimizations were made in section 5.5. A test scenario for spectrum monitoring is presented in section 5.6, and finally section 5.7 concludes the chapter.

5.2 Architecture

The architecture for a bandpass $\Sigma\Delta$ ADC based spectrum sensing receiver is shown in Fig. 5.1a. The targeted implementation of that architecture is as shown in Fig. 5.1b. In this work, we present the standalone implementation of the DBE on FPGA and validation of its functionality. In order to achieve that standalone implementation properly, the AFE chip is operated at the desired sampling (clock) and center (input) frequencies and the chip output is saved by a digital oscilloscope. Also, to show that the implemented digital backend does not reduce the SNR, an ideal front-end output is generated using MATLAB and saved. The output data saved is then loaded into the FPGA's ROM as shown in Fig. 5.2. This ROM feeds the implemented DBE which consists of Digital Down Conversion Mixer, Digital Decimation Filter, Fast Fourier Transform, and finally Energy Detection and Decision.

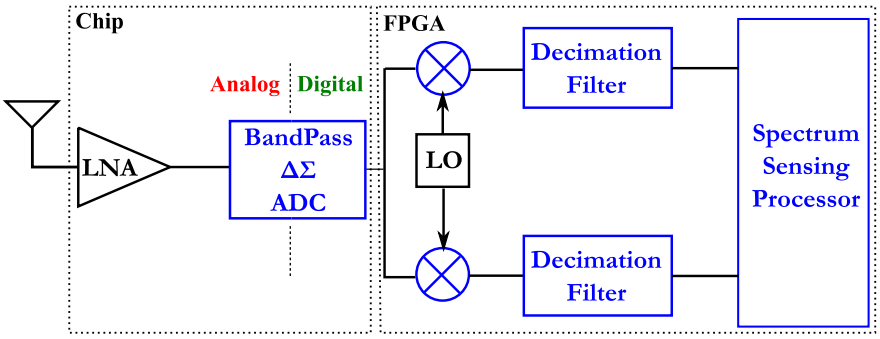

(a) Diagram of the Receiver Architecture

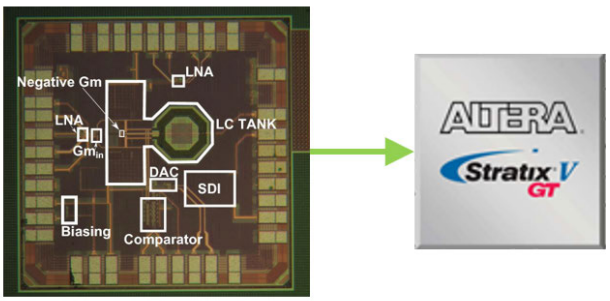

(b) Targeted Implementation of the Receiver, AFE Chip [Sayed16], FPGA [Intel]

Fig. 5.1: Spectrum Sensing Receiver

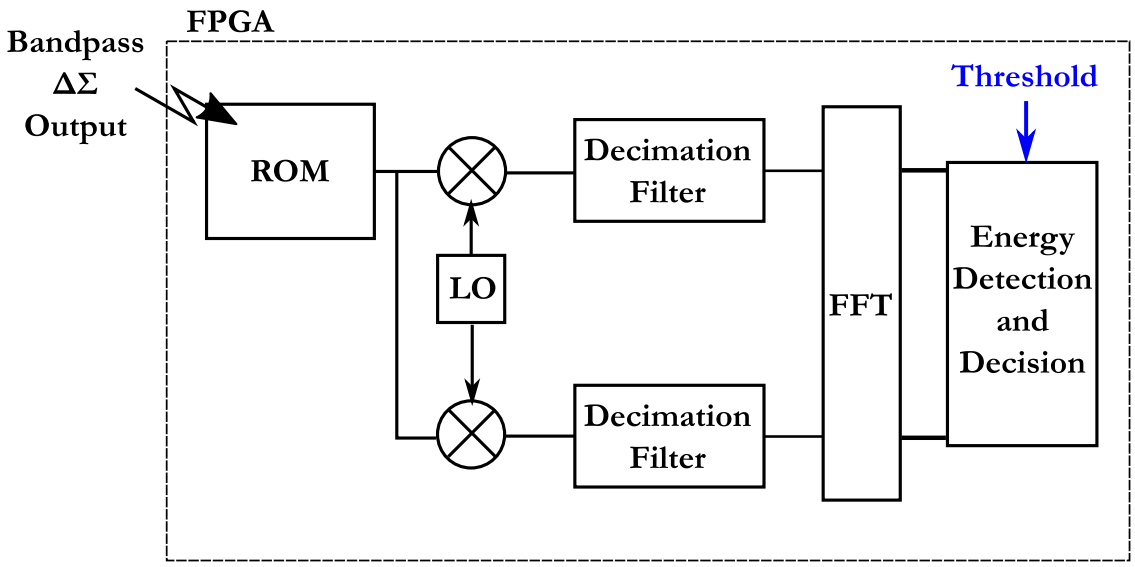

Fig. 5.2: Standalone Implementation of the Digital Backend on FPGA

5.3 Digital Down Converting Mixer and Decimation Filter

5.3.1 Implementation

We mentioned in chapter 3 that the sampling frequency, f_s, is set to be equal to $4f_c, 4f_c/3, ...$, where f_c is the center frequency. In this implementation, we have $f_s = 4f_c/3$, this setting results in having the carrier signal samples at $\{1, 0, -1, 0\}$, which enables subsampling the input data to the mixer, as shown in Fig. 5.4, by two without loss of information. The extra subsampling reduces the speed, and hence power consumption, requirements. On more important gain of that setting of sampling frequency, is that now the mixer multiplies either by 1 or -1 and this can be simplified by building an XOR gate instead of a full multiplier.

The decimation filter designed [Haghighitalab18] for this digital backend is shown in Fig. **??**. The decimation factor ig 64 and carried out through three stages, 16, 2, and 2. The first stage is a comb filter, and the two following stages are HalfBand Filters (HBF). In order to estimate the maximum word length of each stage, the DDC mixer output is assumed to be a bitstream of '1'. In this way, the output of the first stage is is the summation of all of the coefficient values, 8192, so that word length is assumed to be 14 bits. Following the first

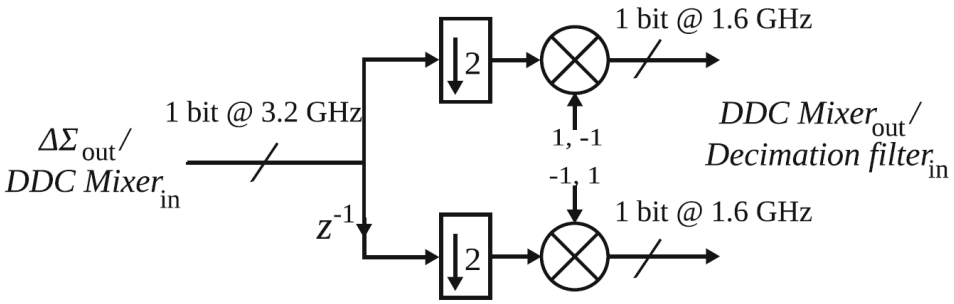

Fig. 5.3: Simplified Implementation of Digital Down Converting Mixer [Haghighitalab18], with Example of RF front-end output at $f_s = 3.2GHz$, which corresponds to $f_c = 2.4GHz$

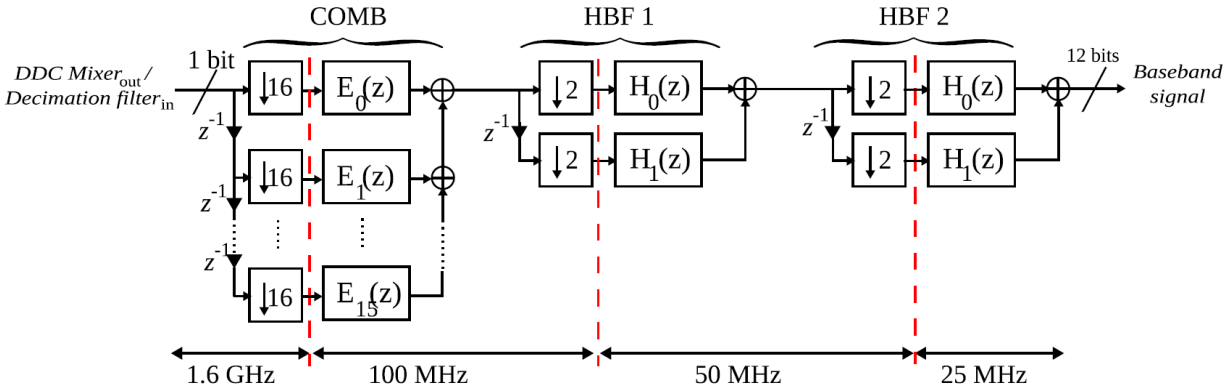

Fig. 5.4: Implementation of Decimation Filter [Haghighitalab18], with Example of RF front-end output at $f_s = 3.2GHz$, which corresponds to $f_c = 2.4GHz$ and baseband signal bandwidth of $25MHz$

stage, each of the HBF's adds, in maximum, 7 bits to that word length. The maximum final output length is 28 bits.

The complete digital backend implementation is shown in fig. 5.5. The implemented design is composed of a ROM, a splitter, digital down conversion (DDC) mixer, and a decimation filter. The data stored in the ROM is an output of the AFE chip and it is stored in 32 bit wide words. The ROM is read by an address counter clocked by a frequency of $f_s/32$, where f_s is sampling frequency of the corresponding AFE chip output. The splitter is to divide the

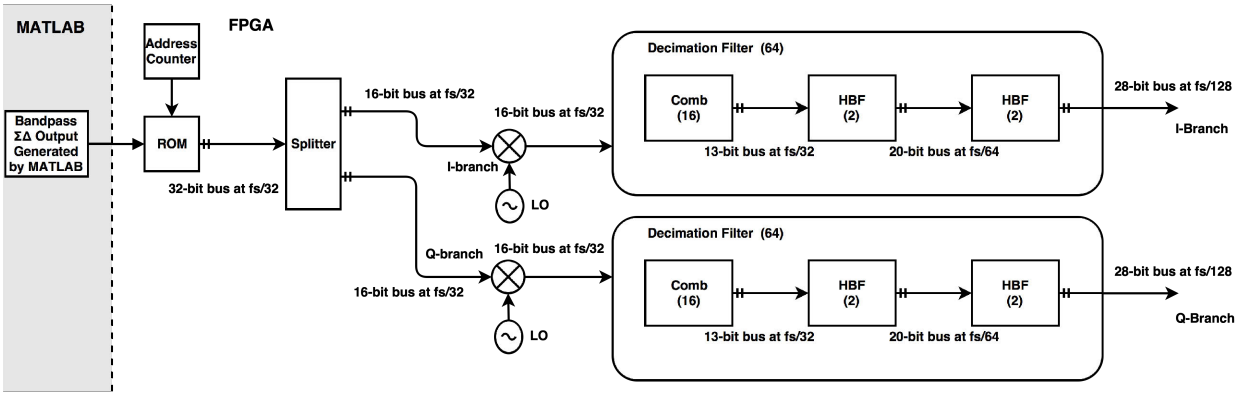

Fig. 5.5: Digital Down Converting Mixer and Decimation Filter FPGA Implementation Architecture

32 bits words into two 16 bits words for I and Q branches. One of the two 16 bits words consists of the odd-numbered bits in the original 32 bits words and the other consists of the even-numbered bits. The DDC mixer is, as discussed in chapter 3, an array of XOR gates. The decimation filter used here is of decimation factor 64. It's composed of three stages, decimation by 16, by 2, and by 2 one more time. The clock frequencies required to operate the filter are: $f_s/32, f_s/64$ and $f_s/128$.

5.3.2 Dynamic Frequency Unit for Frequency Sweeping

A block for sweeping the frequency dynamically [Turk17] is added and integrated with the design shown in Fig. 5.5. The circuit architecture is shown in Fig. 5.6.
This block helps:
- Accelerate the validation process by changing the frequency without the need of recompiling nor re-synthesizing.
- Emulate the frequency sweeping in a spectrum sensing receiver.

The frequency sweep block provides 7 different frequencies (2, 2.18, 2.4, 2.66, 3, 3.4 and 4 GHz)/32 which correspond to the sampling frequency. It has three outputs: clk ($f_s/32$), clk/2 ($f_s/64$), and clk/4 ($f_s/128$). The number of frequencies is a limitation from the FPGA. The frequency selection can be controlled using a finite state machine or by direct input to

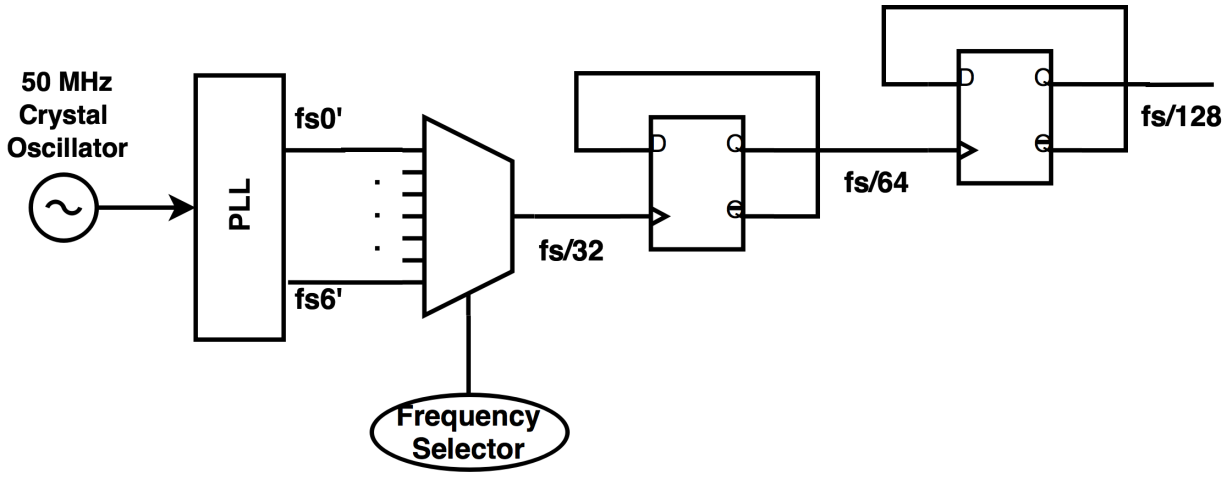

Fig. 5.6: Clock Multiplexing Based Frequency Sweeping with the Clock Dividers

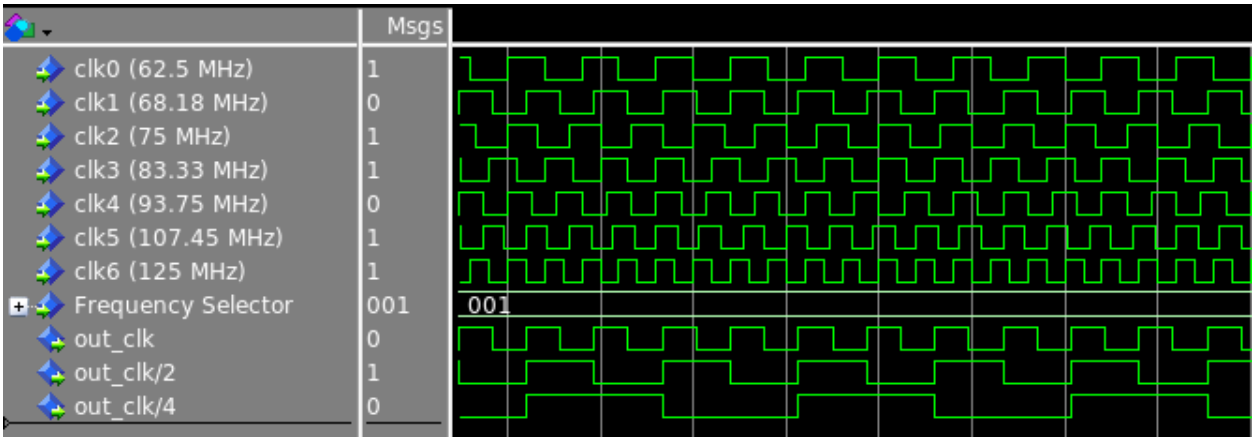

Fig. 5.7: Frequency Sweeping Implemented Circuit Simulation

the multiplexer. The functionality is validated using simulation and the result is presented in Fig. 5.7. The different frequencies are shown in the simulation and the period of each clock frequency is verified. We can see the selection is "001" which corresponds the clk1, so the outputs are clk1, (clk1)/2 and (clk1)/4.

5.3.3 Validation of the Digital Down-Conversion Mixer

In this work, to validate the FPGA implementation, Altera SignalTab Logic Analyzer software tool was used to implement a logic analyzer onto the FPGA in order to probe and

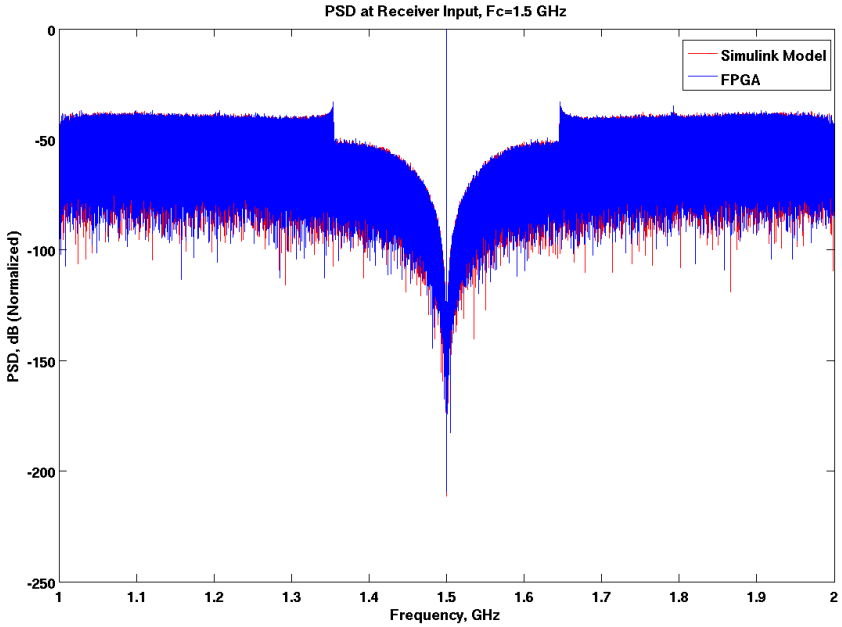

Fig. 5.8: Bandpass $\Sigma\Delta$ ADC Output (f_c=1.5 GHz)

acquire the data at specific nodes for a defined acquisition clock and duration. The functionality of the implemented down converting mixer is verified using MATLAB simulation by comparing the output result from the FPGA to the Simulink model mixer output and calculating the Signal to Noise Ratio (SNR) value. It was chosen to use an ideal system model whose output SNR can reach 70 dB instead of the chip output with an SNR of about 35 dB. The signal used is a sinusoidal and the input to the mixer is registered in a ROM and originally comes from an ideal bandpass $\Sigma\Delta$ output generated by a Simulink model. The Power Spectral Density (PSD) of the output data for a center frequency (f_c) of 1.5 GHz and $f_s = 4 * f_c/3$ of 2 GHz is shown in Fig. 5.8. The down converted ouput from the mixer is shown in Fig. 5.9.

5.3.4 Validation of the Decimation Filter

The output is at a frequency equal to $f_s/128$ where f_s is the sampling frequency and equals to $4/3f_c$. We want to validate the functionality of the filter over the entire range of sampling

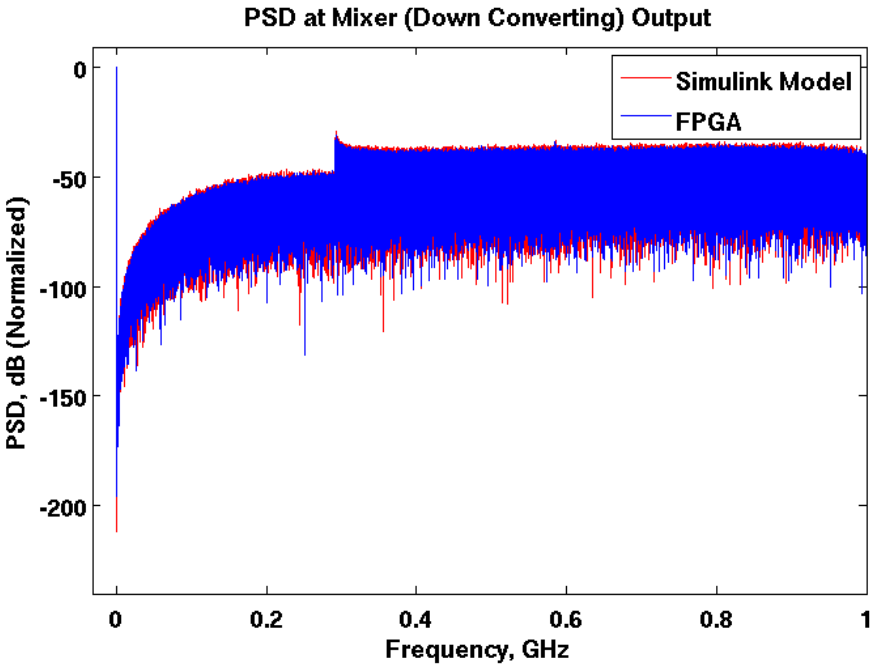

Fig. 5.9: Digital Down Converting Mixer Output

frequencies from 2 to 4 GHz. The dynamic frequency unit is used to accelerate this validation by changing the operating frequency and acquiring data from the output and compare it to the Simulink model result. The SNR of both Simulink and FPGA must be nearly equal. Fig. 5.10 shows the output of the decimation filter of the I-branch for $f_s = 2$ and $4GHz$ along with their SNR value with the same sinusoidal used before. The x-axis is shown in log scale for a better view of the signal and noise levels. The SNR value at the decimation filter output in the Simulink model is equal to 70.26 dB. The result from the FPGA acquisition almost matches the system model with nearly same SNR.

The different SNR results at different sampling frequencies are summarized in Table 5.1. The PSD at the filter's output for the rest of frequencies is shown in Fig. 5.11.

5.4 Spectrum Sensing Baseband DSP Processor

Our spectrum sensing processor is based on frequency domain energy detection. The architecture is presented in Fig. 5.12. It is composed of three main building blocks: an FFT (Fast

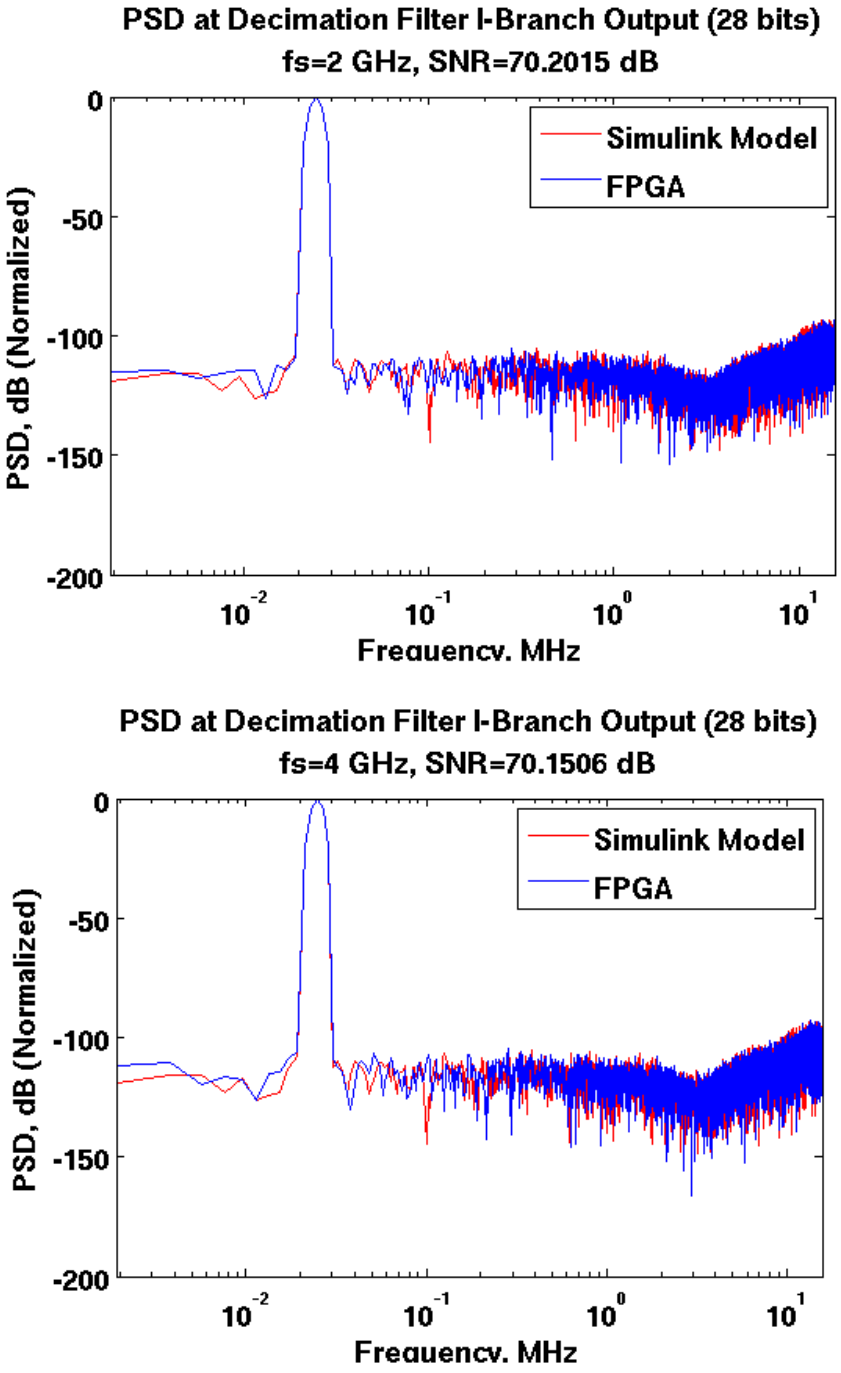

Fig. 5.10: Decimation Filter Output (f_s=2 and 4 GHz)

Fourier Transform), an energy calculation block and a decision taking and monitoring block. Each block will be discussed in the following subsections.

Table 5.1: SNR Values at the Decimation Filter Output

f_s (GHz)	SNR (dB)
2	70.2015
2.18	70.1407
2.4	70.1761
2.66	70.1294
3	70.1631
3.4	70.1318
4	70.1506

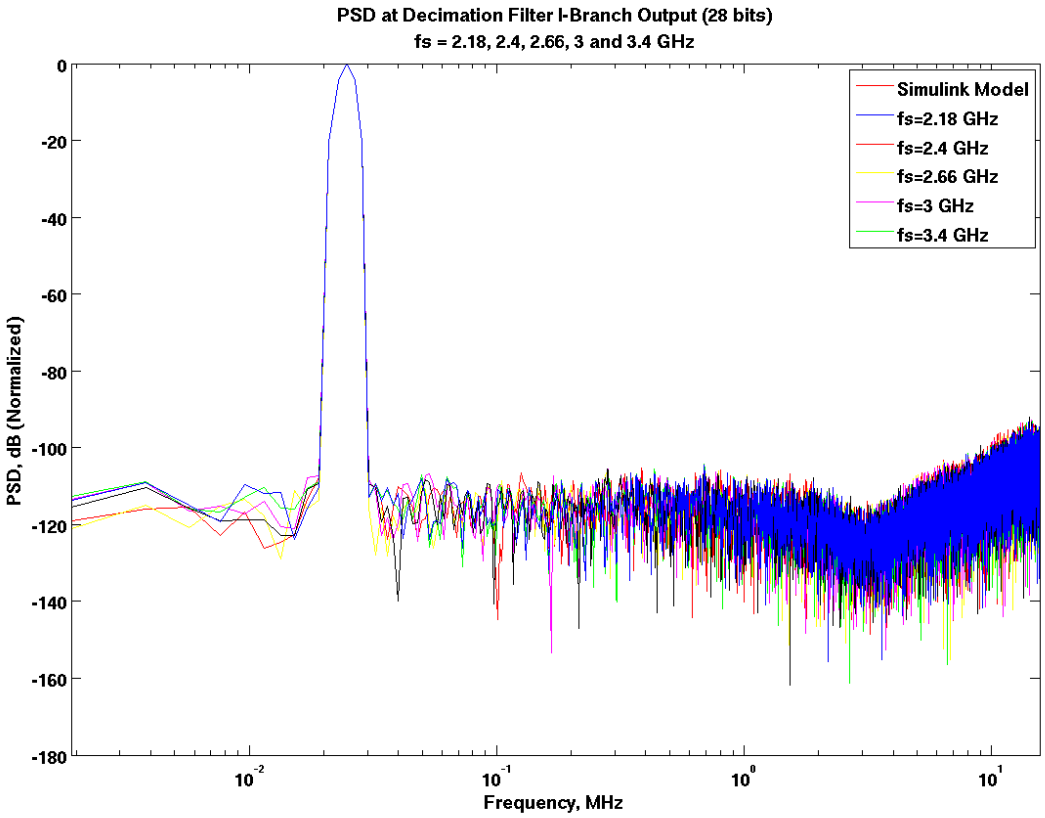

Fig. 5.11: Decimation Filter Output (f_s=2.18, 2.4, 2.66, 3 and 3.4 GHz)

5.4.1 FFT Block

The FFT IP from Altera is used. It is the 16K variable streaming FFT. This FFT has an option to change its number of points dynamically during its operation. The FFT block with

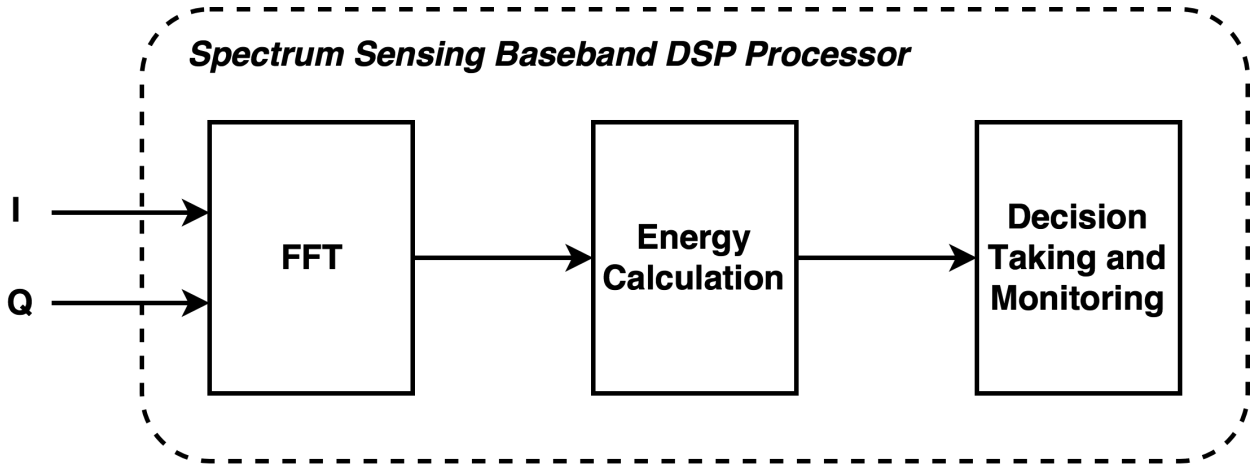

Fig. 5.12: Frequency Domain Energy Detection Spectrum Sensing Processor Architecture

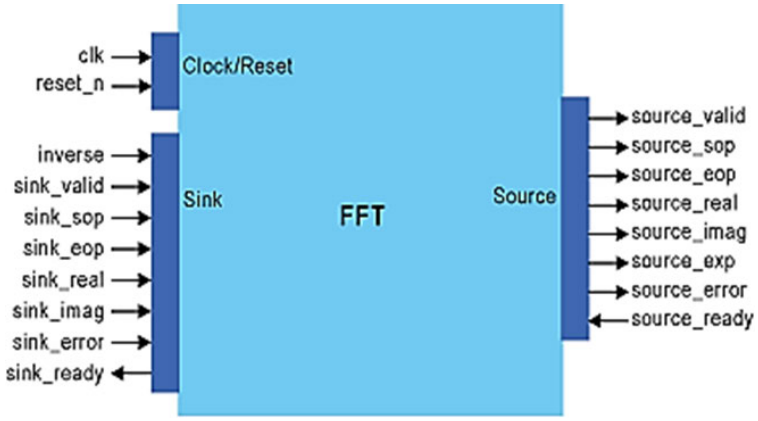

Fig. 5.13: FFT IP Block Inputs and Outputs

its inputs and outputs is presented in Fig. 5.13. It has two inputs which will be connected to the I and Q branches coming from the two decimation filters. The output of the FFT has two branches as well, a real and an imaginary. The block has many control signals that are responsible for the flow of the input data and the operation of the FFT. A controller is designed to provide these signals via finite state machine (FSM). The control is done as follows: we deassert the system reset, the data source asserts *sink_valid* to indicate to the FFT function that valid data is available for input. Then we assert both the *sink_valid* and the *sink_ready* for a successful data transfer. The control flow signals are shown in Fig. 5.14.

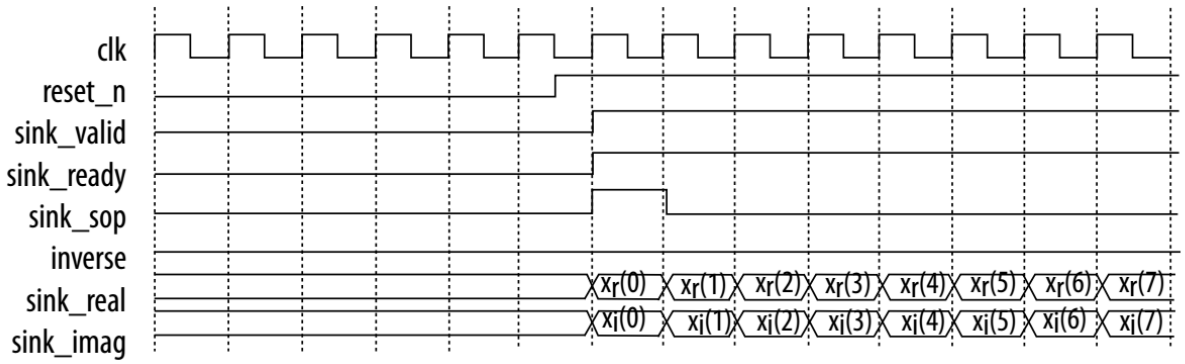

Fig. 5.14: FFT Streaming Input Data Flow Control

The FFT and its controller are then integrated with the previously shown blocks of the design with its input coming from the decimation filter output. The operating frequency of the block is $f_s/128$. The correct functionality of the FFT is verified by comparing the acquired output from the FFT on the FPGA with the FFT performed by MATLAB using the same test signal. The verification was done using two different signals, the usual sinusoidal one and QPSK (Quadrature Phase Shift Keying) one. QPSK is a type of modulation that has four symbols. Each symbol has two bits and is represented by a different phase. The validation results with both of the above mentioned signals are presented in Fig. 5.15.

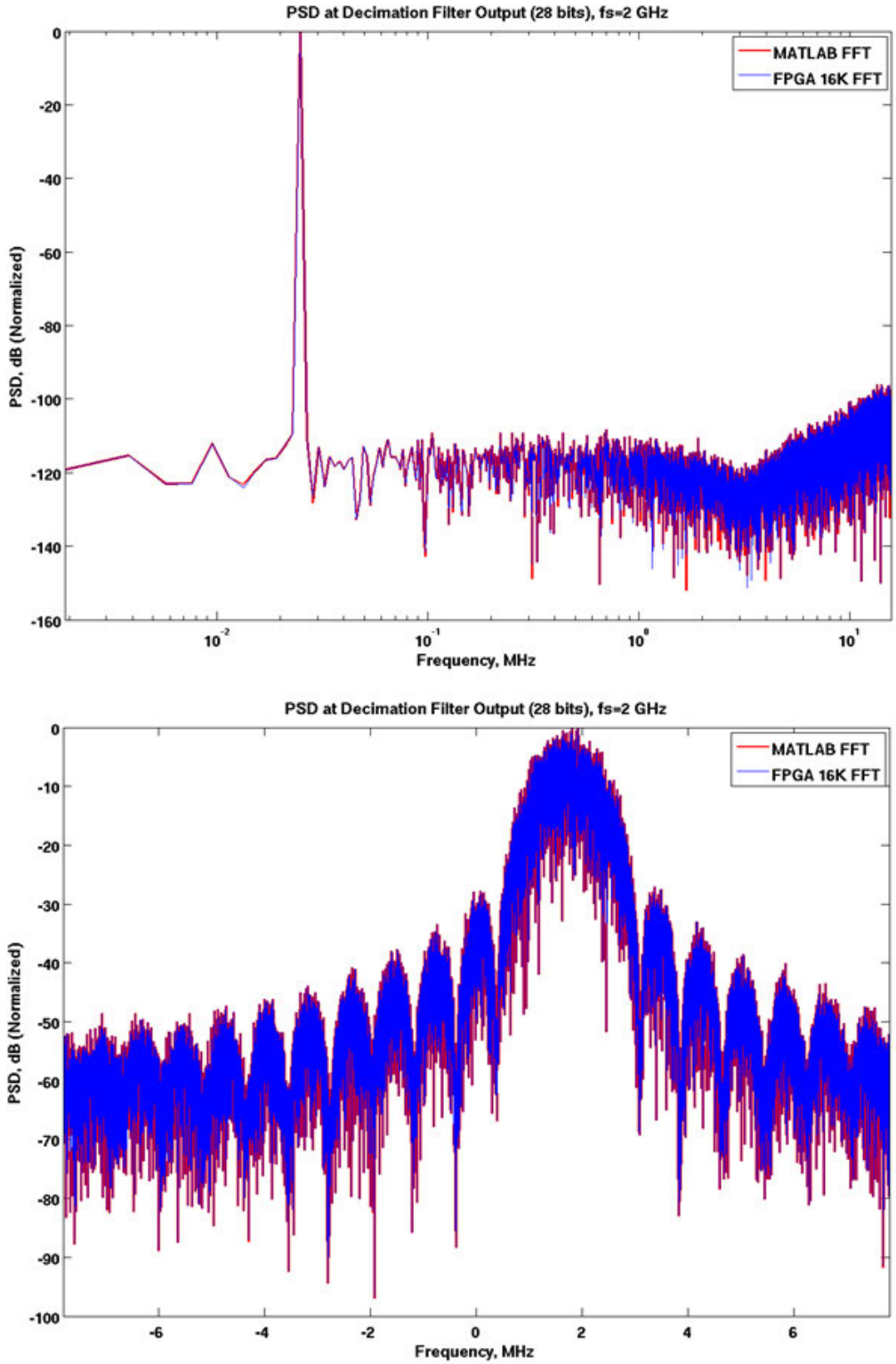

Fig. 5.15: FFT Validation Results Using (a) a Sinusoidal Signal (b) a QPSK Signal

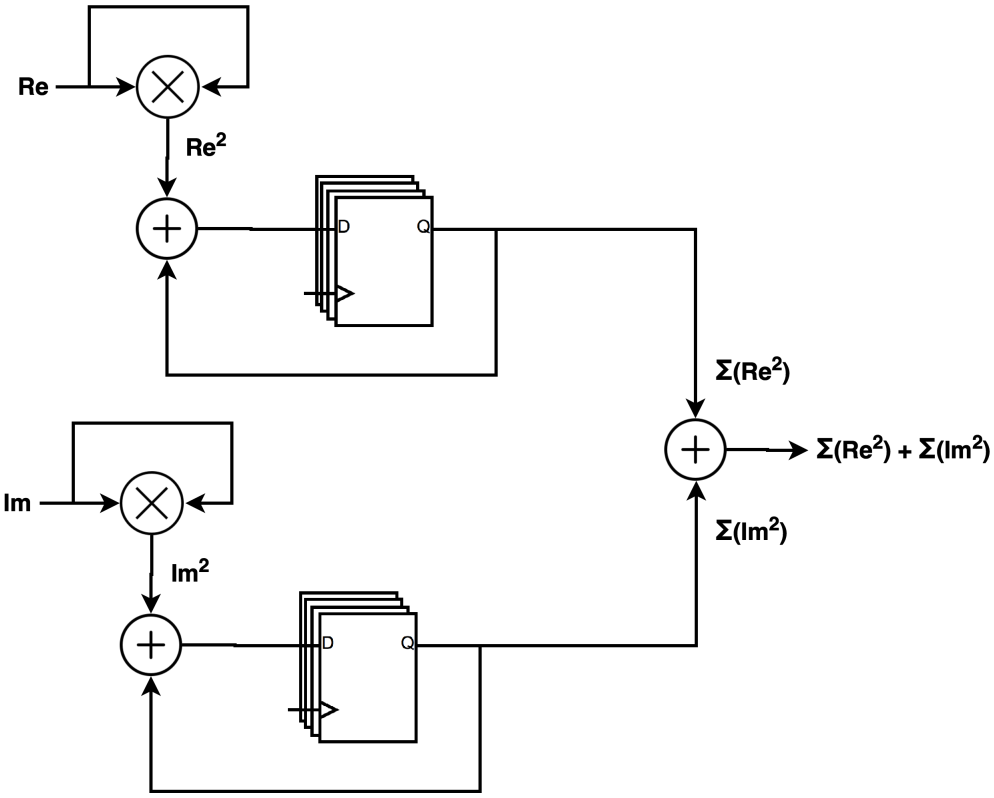

Fig. 5.16: Energy Calculation Circuit

5.4.2 Energy Calculation

The FFT is followed by the energy calculation block. The mathematical formula of the energy calculation is:

$$\begin{aligned} E &= \sum_{k=0}^{N-1} |X(k)|^2 \\ &= \sum_{k=0}^{N-1} \left(\sqrt{(Re(X(k)))^2 + (Im(X(k)))^2} \right)^2 \\ &= \sum_{k=0}^{N-1} (Re(X(k)))^2 + \sum_{k=0}^{N-1} (Im(X(k)))^2 \end{aligned} \tag{5.1}$$

where X is a complex signal composed of the real and imaginary outputs from the FFT. The above formula can be realized with the circuit shown in Fig. 5.16.

This circuit has two multipliers, two accumulators and an adder. It's validated by comparing the calculation done on the FPGA with MATLAB results and it was found that they are equal.

5.4.3 Decision Taking and Monitoring

The last block in the spectrum sensing processor is for comparing the energy value with a certain threshold and takes a decision whether a channel or a whole band is occupied or not.

To evaluate the performance of the algorithm and get some useful information, we need to plot an evaluation curve of P_D and SNR. To plot, we need to determine a value for P_{FA}, so we decided to follow the standard IEEE 802.22 for Wireless Regional Area Network (WRAN) which defines a maximum P_{FA} of 10 %. Then, we run a set of simulation with a lot of different signals where some are noise only and some signal with noise together. The output will P_D in function of SNR and the number of points of the FFT and the threshold in function of the same previous parameters. The evaluation curve is shown in Fig. 5.17.

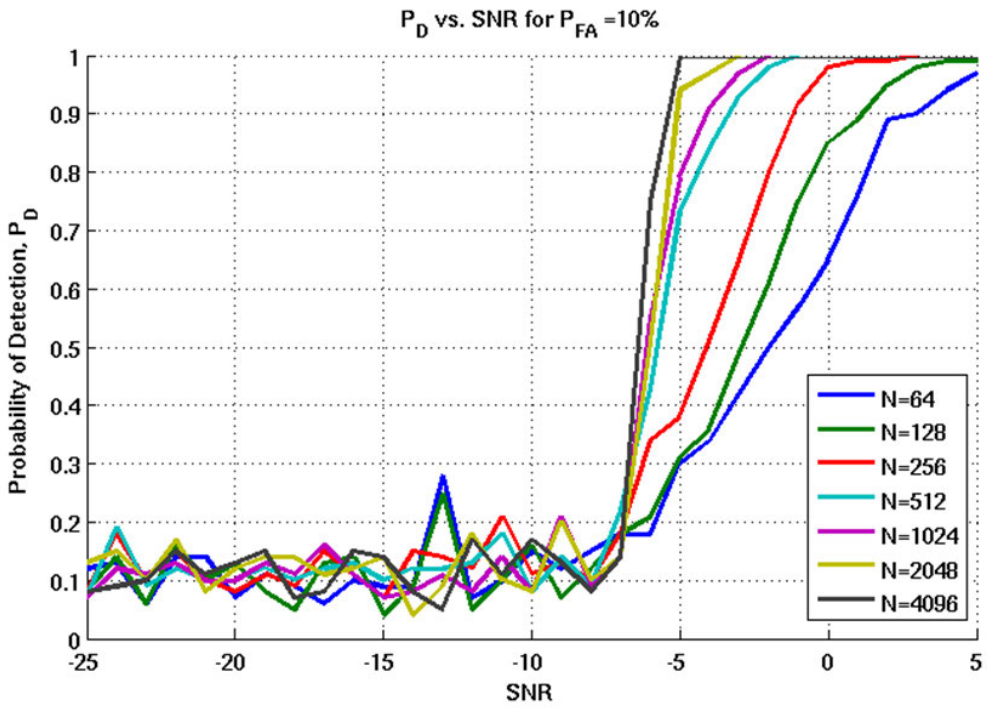

Fig. 5.17: Pd vs. SNR for P_{FA}=10% and different N-Point FFT

P_D is plotted against SNR. Negative SNR values mean that the noise level is higher than the signal itself. Our objective is have P_D reaches 1 when the SNR is equal to 0. This means that we can detect the signal when the noise level and the signal level are the same. For N from 64 to 256, this did not occur but from 512 to 4096, P_D reaches 1 even with a negative SNR. This result indicates to use a 512-point FFT. We can see that the 4 curves representing N from 512 to 4K are very close, so we can use the least of them to reduce complexity and latency.

5.5 Design Optimization

We begin here a phase of optimization to enhance the overall design in terms of area, power consumption and speed.

5.5.1 Reducing the Number of Bits at the Decimation Filter Output

The objective of this optimization is to reduce the number of bits at the decimation filter output because it will increase after passing by the FFT block and then all the multiplication, the accumulation and addition. The theoretical required number of bits is 28, the dedicated multipliers in the FPGA used are 18 by 18 multipliers. The truncation effect will be shown in Fig. 5.18 by calculating the SNR while truncating the number of bits.

The above plot shows the SNR against the number of bits from 1 bit up to the complete 28-bit output we are using. The result shows that starting from 18 bits, the SNR start to stabilizes at 70 dB. Fig. 5.19 shows the PSD of the decimation filter output with 28, 18, 16, and 12 bits words. No difference can be noticed between 28 bits and 18 bits but for 16 and 12 bits, we can observe that the noise level begins to increase a lot. These results do validate our choice of truncating the decimation filter output and using only 18 bits.

5.5.2 Custom 512-Point FFT

The Altera FFT IP has a significant drawback. It can only be used with the FPGA and the Quartus II software. This means that it will not be suitable for a future ASIC implementation.

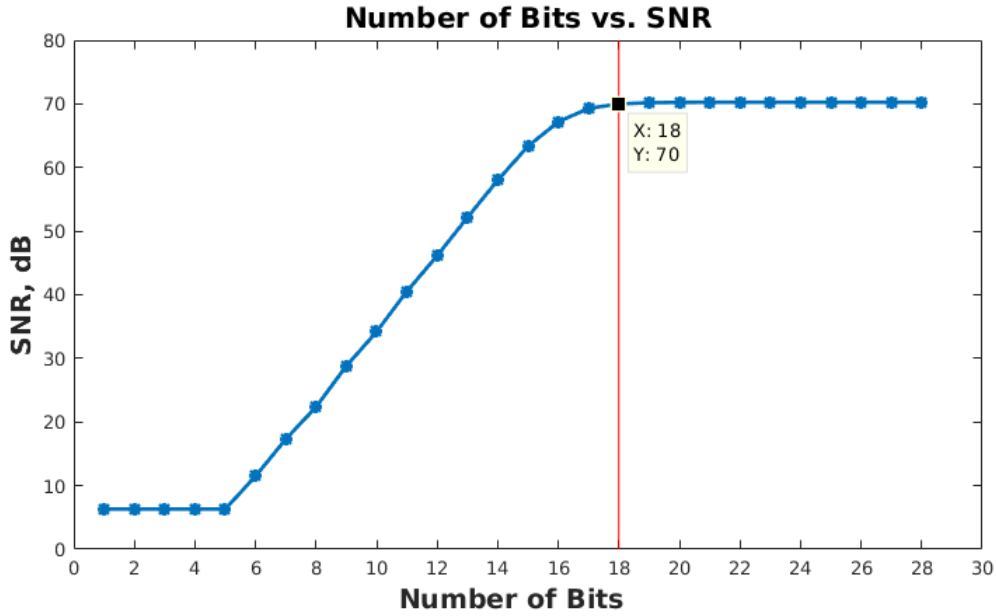

Fig. 5.18: Number of Bits vs. SNR

Table 5.2: FPGA Utilization

Number of Adaptive Look-Up Tables (ALUT)	9459
Number of DSP Blocks	15
# of Dedicated Logic Registers	13517

HDL coder tool from MATLAB is used to generate the VHDL files of an optimized 512-point FFT. This tool can convert some simulinks blocks to HDL files. To start using the tool, we need at the beginning to build a system that contains the block to be converted which is the FFT. Fig. 5.20 presents the Simulink model that was built and used.

For a successful conversion from SIMULINK to FPGA, many configurations have to be made such as using fixed point instead of floating point representation, well defined sampling time, etc. After getting the VHDL files from tool, we replaced the FFT IP and the validation process was repeated successfully. This FFT has also a controller that is somehow similar to the previously used. A great advantage from this FFT is the latency. It has a lower latency than the IP one (1078 vs. 1102 clock cycles). The utilization results of the optimized design are summarized in Table 5.2.

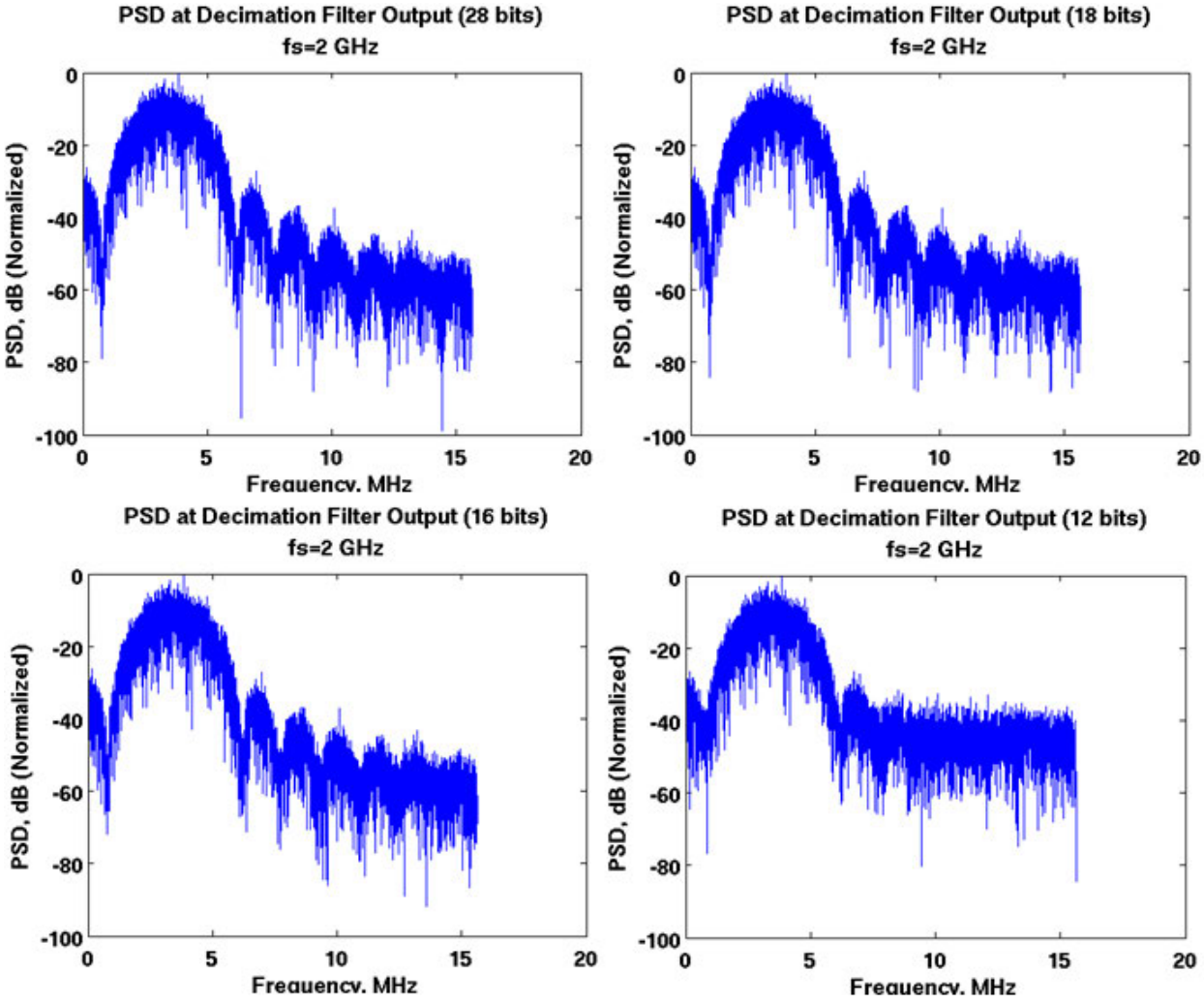

Fig. 5.19: Result of Reducing the Number of bits at the Decimation Filter Output on a QPSK Signal

5.6 Test Scenario

Finally, we will demonstrate a test scenario for the whole design on the FPGA. Fig. 5.21 presents a spectrum from 1.5 to 3 GHz which corresponds to f_s from 2 to 4 GHz. At seven different frequencies there are seven different signals, sinusoidal and QPSK. Each signal is stored on a ROM and we change the frequency using the dynamic frequency sweeping unit.

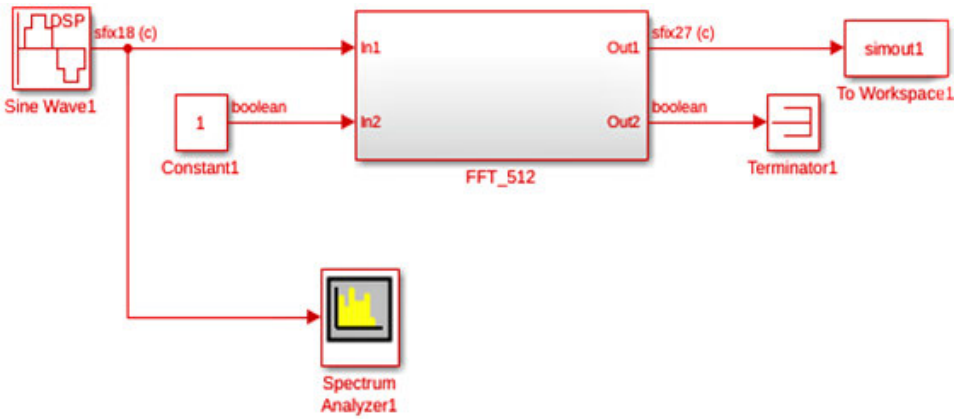

Fig. 5.20: Simulink Fixed-Point FFT Model

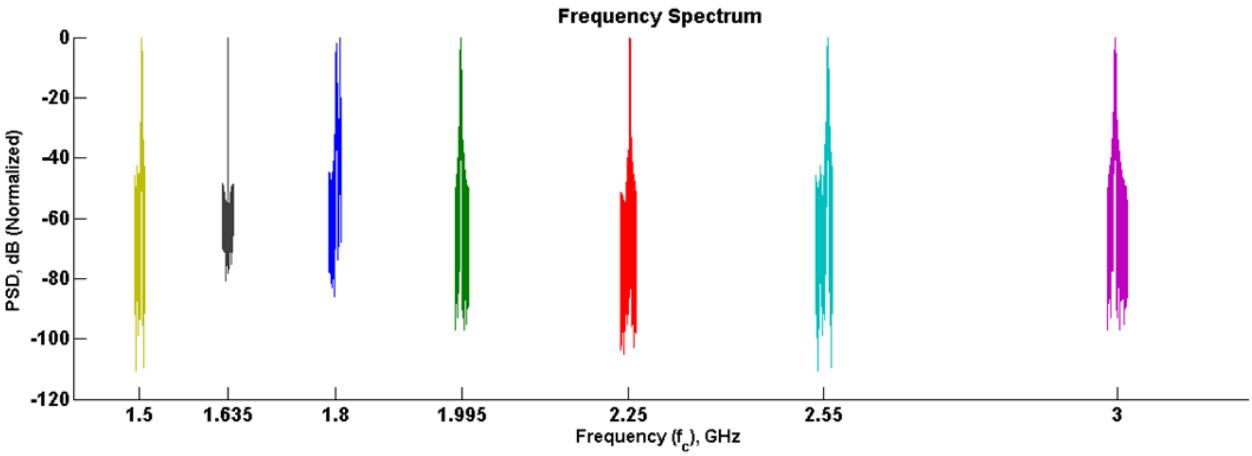

Fig. 5.21: A Frequency Spectrum from 1.5 to 3 GHz with 7 Different Signals

We chose the signal at f_c=1.8 GHz to be our test signal. It is shown in Fig. 5.22 and we can see that it has 2 different QPSK signals. The sampling frequency f_s is 2.4 GHz, the bandwidth is 18.75 MHz. It is also channelized into 8 sub-bands.

The acquisition result from the FPGA is shown in Fig. 5.23. We have the FFT real and imaginary outputs, the frequency selection which is 2 and it corresponds to f_s=2.4 GHz. We have also the calculated energy, the different sub-bands or channels and the occupied flag. The numbering of the channels starts by 5 because the normally, the first N/2 outputs of

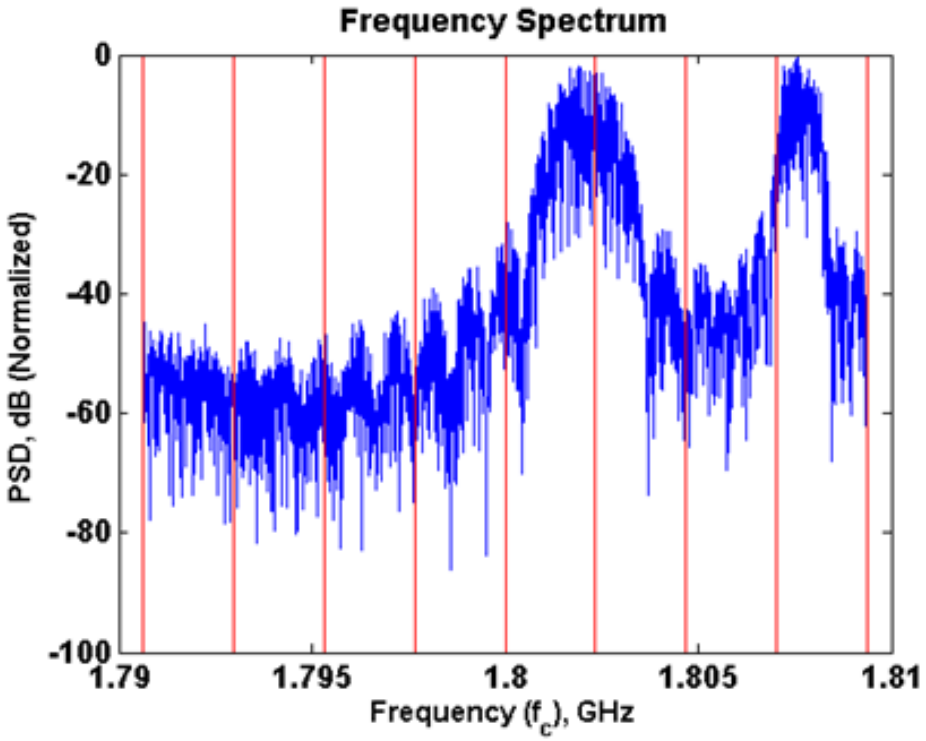

Fig. 5.22: QPSK Test Signal, 8 subbands (channels) centered around $f_0 = 1.8GHz$, data is transmitted on channels 5, 6, and 8

the FFT represents the positive frequencies and the other represent the negative frequencies. The occupied flag is asserted for sub-bands 5, 6 and 8 as expected.

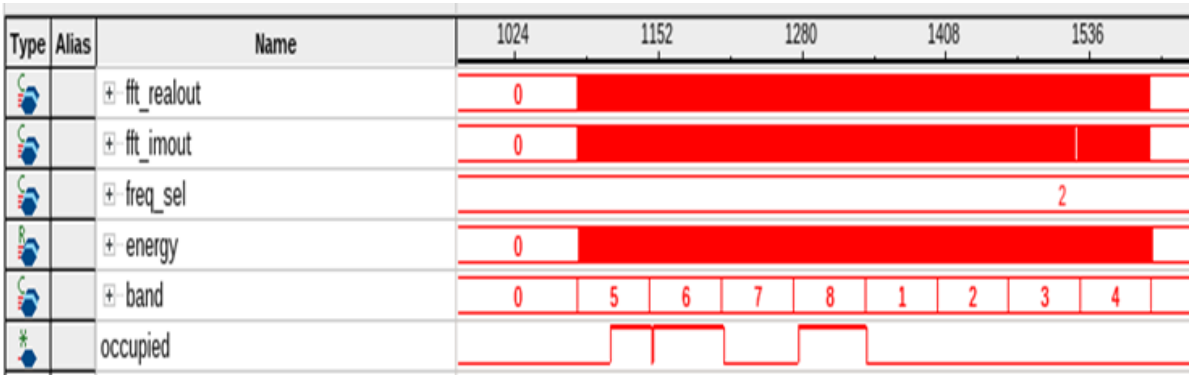

Fig. 5.23: Test Scenario FPGA Acquisition Result. The circuit is capable of detecting that channels 5, 6, and 8 are busy.

5.7 Conclusions

In this chapter the digital back end (DBE) of the proposed architecture in chapter 4 is implemented to process the output of the AFE chip presented in chapter 3. We presented the architecture of the implemented DBE. The down-conversion mixer and decimation filter implementation and validation was discussed. We also showed the spectrum sensing processor implementation. Design optimizations were made. Finally, a test scenario of spectrum monitoring was presented to validate the implementation.

Chapter 6

Impact of I/Q Imbalance on the Spectrum Sensing Performance

6.1 Introduction

In this chapter, we perform hardware measurements to study the impact of I/Q imbalance on spectrum sensing algorithm based on energy detection. The organization is as follows: in Section 6.2.1, we present the scenarios and assumptions for spectrum occupation used to develop this work. The measurement setup as well as calibrations of the AFE and its relative mismatch are presented in section 6.3 . Section 6.4 discusses the measurements results. Conclusions are presented in Section 6.5.

6.2 Scenarios and Assumptions for Spectrum Occupation

6.2.1 Spectrum Sensing Technique

Energy detection can be made in time-domain or frequency-domain. In this work, frequency-domain energy detection is favored for its higher decision resolution [Yucek09a]. The Spectrum-to-be-Sensed is divided to several multi-channel bands and sub-bands as illustrated in Fig.6.1.

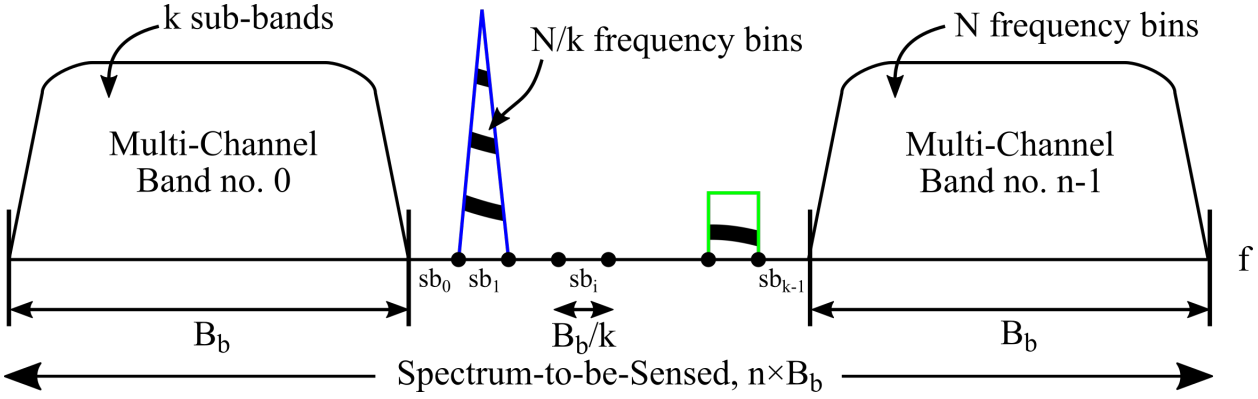

Fig. 6.1: The Spectrum-to-be-Sensed is divided into n multi-channel bands. Each band contains k sub-bands. Energy estimation is performed using an N-point FFT per band and is used to detect the spectrum occupation of each sub-band.

The frequency-domain energy estimation procedure used in this study can be summarized in the following steps:

- Split the Spectrum-to-be-Sensed to n multi-channel bands, each having a bandwidth, B_b.
- Down-convert sequentially each multi-channel band.
- Perform an N-Point FFT of each band to obtain an estimation of the Power Spectral Density (PSD):

$$S_b(f) = |\mathcal{F}\{x(t)\}|^2, \tag{6.1}$$

  where $x(t)$ is the sampled time-domain signal.
- Split $S_b(f)$ into k_{sb} sub-bands, each having a bandwidth, $B_{sb} = B_b/k_{sb}$.
- Sum the PSD frequency bins of sub-band number i, in order to obtain an estimation of the energy, $\hat{E}_{sb_i}$, in this sub-band:

$$\hat{E}_{sb_i} = \sum_{N/k_{sb}} S_{sb_i}(f), \tag{6.2}$$

  where $S_{sb_i}(f)$ is the PSD of sub-band number i. Note that i is the index of the sensed sub-band and in the range $\{0..k_{sb}-1\}$.

In frequency-domain energy-detection, there are three metrics to be considered:

- **Sensing-Resolution:** In order to increase the sensing-resolution, the number of sub-bands, k_{sb}, should be high. The highest sensing-resolution is achieved when the number of sub-bands, k_{sb}, is equal to the number of transmitted channels, k_{ch}, in the band.
- **Sensing-Accuracy:** According to the central limit theory [Umar14], to assume a Gaussian distribution of energy, the number of bins per channel, N/k_{sb}, should be high. This is an important parameter for an accurate energy detection.
- **Sensing-Time:** As shown in Fig.6.2, assuming the acquisition, FFT and energy calculation operations are pipelined, it can be shown that the total Spectrum-Sensing time, T_{sense}, is equal to:

$$T_{sense} = (n-1)\ \max(T_{acq}, T_{FFT}, T_{EC}) + T_{acq} + T_{FFT} + T_{EC}, \tag{6.3}$$

  where T_{Acq} is the multi-channel band acquisition-time, T_{FFT} is the duration of the N-point FFT computation and T_{EC} is the duration of the energy calculation.

From the aforementioned, it is clear that we need an FFT with a large N in order to achieve a high decision-resolution. On the other hand, a large N would lead to a long sensing-time. In this work, we have chosen to perform the calculations on a relatively narrow-band in order to achieve a reasonable sensing-time.

In the following, we summarize all the parameters we used in this spectrum-sensing energy-detection procedure:

- Spectrum-to-be-Sensed: $StbS$ = 0.3 - 3 = 2.7 GHz
- Multi-channel Band bandwidth: B_b = 20 MHz
- Number of Bands: $n = StbS/B_b$ = 135
- Number of transmitted channels per band: $k_{ch} = 8$
- Number of sub-bands: $k_{sb} = 8$
- Number of FFT-points: $N = 1024$
- Sampling frequency: F_s = 40 MHz
- Multi-channel band acquisition duration,
  $T_{Acq} = N/F_s = 25.6\ \mu s$,

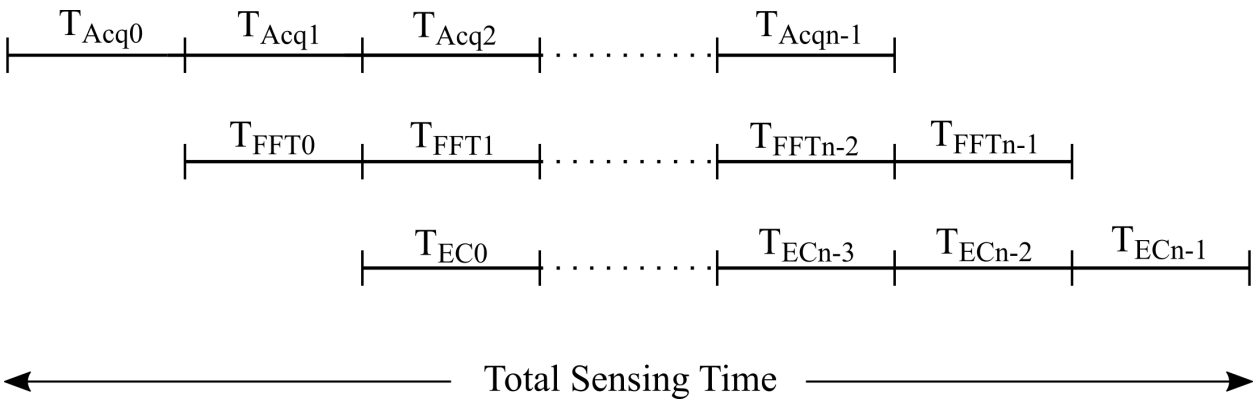

Fig. 6.2: The total Spectrum-Sensing time is equal to the sum of all multi-channel bands acquisition-time, nT_{Acq}, the duration of the N-point FFT computation T_{FFT} and the duration of the energy calculation T_{EC}.

- FFT computation duration, $T_{FFT} = 8.2\ \mu s$,
- Energy calculation duration, $T_{EC} = 7.6\ \mu s$,
- Multi-channel band Sensing-Time, $T_{sense_{band}} = 41.4\ \mu s$,
- Total Sensing Time, $T_{sense} = 3.47$ ms.

6.2.2 Test Hypotheses

In order to evaluate the Spectrum Sensing metrics, P_D, P_{FA} and RoC, for the targeted SDR receiver, we need to define two hypotheses. One hypothesis, denoted $\mathcal{H}_0$, for the case where the sensed channel is unoccupied by a PU and another hypothesis, denoted $\mathcal{H}_1$, for the case where the sensed channel is occupied by a PU. The probability of detection, P_D, is the probability of deciding that a channel is occupied by a PU given that $\mathcal{H}_1$ is true. P_D can then be described as follows:

$$P_D = P(\hat{E}_{sb} \geq \lambda_E | \mathcal{H}_1) \tag{6.4}$$

where λ_E is the threshold energy value. On the other hand, the probability of false alarm, P_{FA}, is the probability of deciding that a channel is occupied by a PU given that $\mathcal{H}_0$ is true. P_{FA} can then be described as follows:

$$P_{FA} = P(\hat{E}_{sb} \geq \lambda_E | \mathcal{H}_0) \tag{6.5}$$

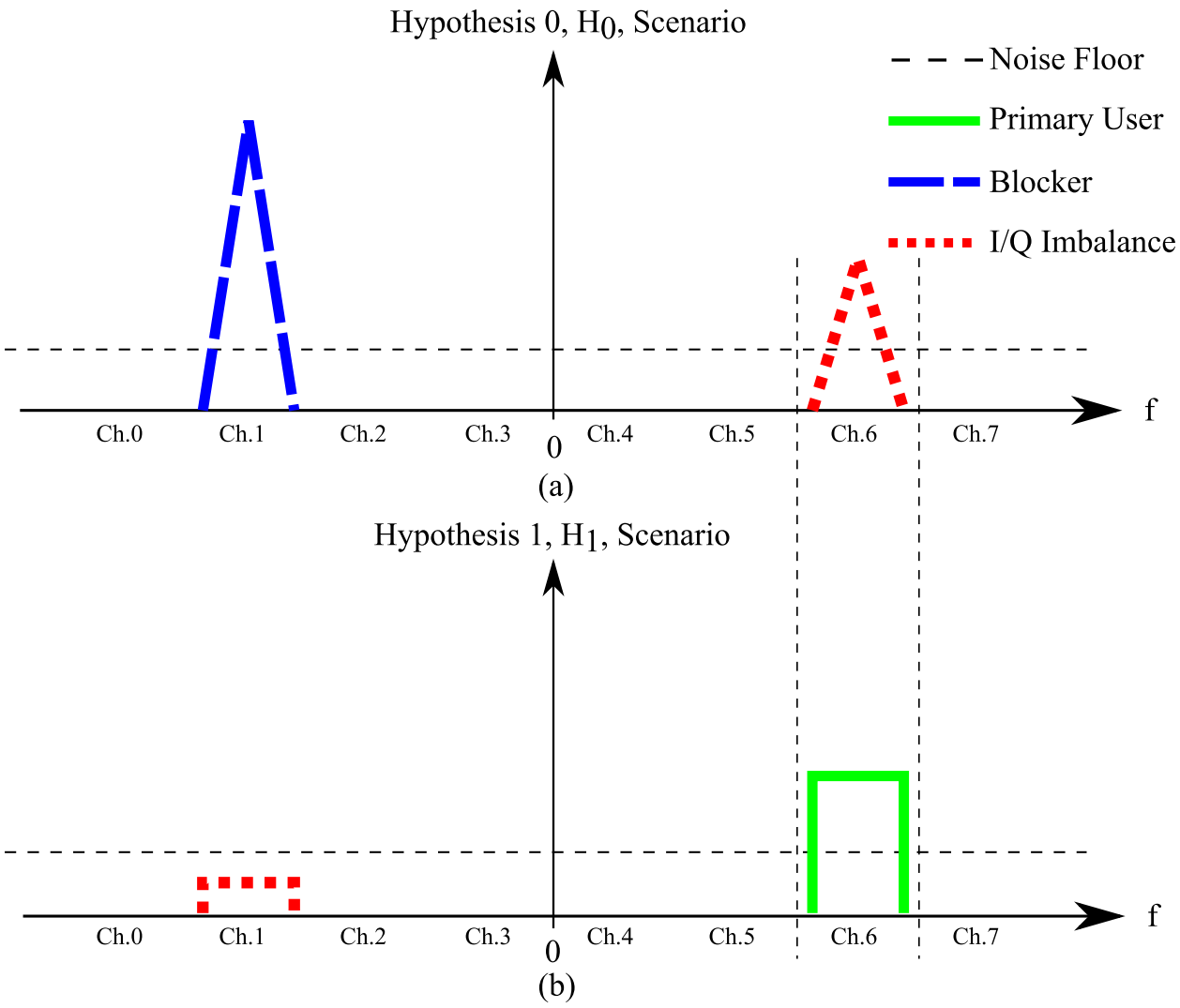

Fig. 6.3: Spectral representation of a) $\mathcal{H}_0$ scenario, where the signal at Ch.1 is a PU blocker signal to the channel to be sensed at Ch.6 because of its I/Q Imbalance component, b) $\mathcal{H}_1$ scenarios with no blocker signal at Ch.1 and a PU at Ch.6.

Fig.6.3 shows an example where the two hypotheses $\mathcal{H}_0$ and $\mathcal{H}_1$ are defined for the case where the sensed channel is no. 6:

- $\mathcal{H}_0$: Channel 6, Ch.6, is unoccupied by a PU signal, but it contains an image of a blocker signal located at Channel 1, Ch.1. This image is due to an I/Q Imbalance in the RF receiver. This scenario is shown in Fig.6.3(a).

- $\mathcal{H}_1$: Channel 6, Ch.6, is occupied by a PU signal and there is no blocker signal at Channel 1, Ch.1. This scenario is shown in Fig.6.3(b).

The calculation of the energy threshold value, λ_E, is crucial for the evaluation of energy-detection metrics. In this paper, we used the Constant False Alarm Ratio (CFAR) method to calculate λ_E [**?**]. In this method, the threshold is chosen in order to achieve a preset P_{FA} value. The calculation procedure is performed through an estimate from repeated stimuli. These stimuli are performed in the $\mathcal{H}_0$ scenario, shown in Fig.6.3(a).

A QPSK signal is transmitted at Ch.1, the mirror frequency of the sensed channel Ch.6. The transmitted signal have the same power in all stimuli. The measured received energy at Ch.6 will be different for each stimulus due to the randomness of channel and circuit noise. The threshold value is then determined in order to achieve the desired preset P_{FA}. It is worth noting that these measurements are performed on an SDR transceiver fully compensated for I/Q imbalances. It then expected, that the image at Ch.6, due to the transmitted signal at Ch.1, would be well below the noise floor. The determined threshold is then used to calculate P_D using stimuli performed in the $\mathcal{H}_1$ scenario, shown in Fig.6.3(b).

6.3 SDR Transceiver Calibration

The measurements were performed using the bladeRF SDR platform with an LMS6002 RF transceiver [nuand18]. In order to get reliable results the platform needs to be calibrated. In this work, the considered RF impairments of the transceiver are the following: DC offset, I/Q Imbalance, and amplifier gain of both the transmitter and receiver. All the mentioned impairments are frequency-dependent and the circuit needs to be calibrated for each center frequency within the operation range. The DC offset of both the transmitter and receiver is calibrated automatically by the board via a command when programming it. The following subsections present how the amplifier gain of AFE of both the transmitter and the receiver as well as the I/Q imbalance are calibrated.

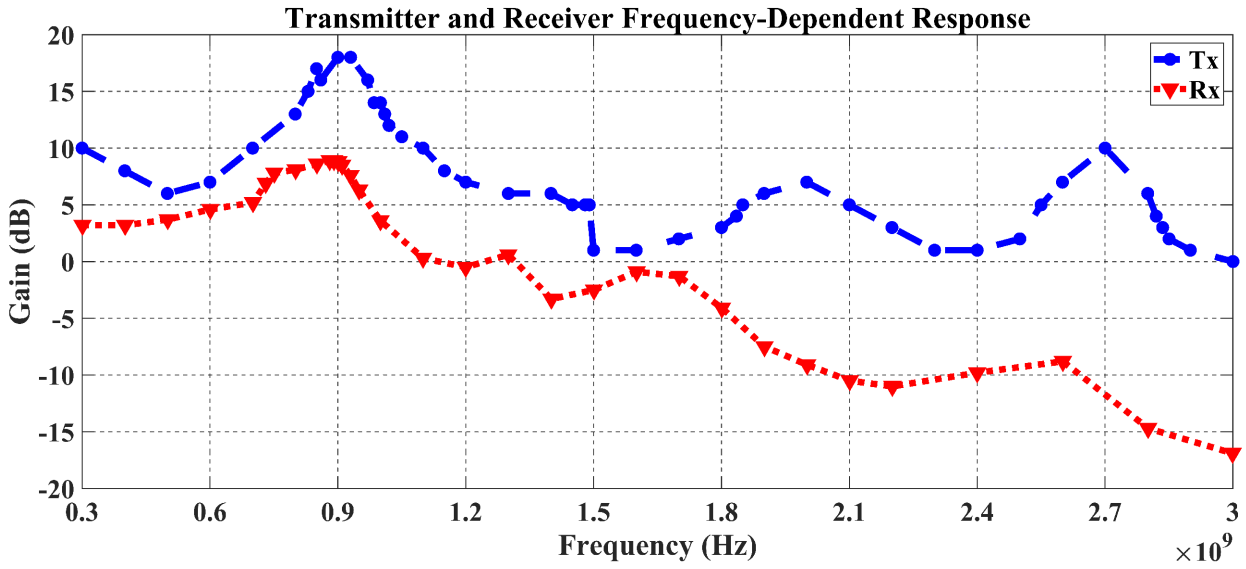

Fig. 6.4: Transmitter and Receiver Frequency-Dependent Response. Results of BladeRF board at transmitted power= -32dBm and injected power= -38dBm

6.3.1 Transmitter and Receiver Gain

It is crucial to calibrate the board and equalize the transmitter power output and the receiver power input, which are frequency dependent for the transceiver in the SDR. An RF signal generator *(Agilent E4432B)*, was used to apply a signal with a constant power over the complete frequency range of the Blade-RF receiver. Similarly, the transmitter was configured to send a constant signal power over the over the complete frequency range of the Blade-RF. The transmitted signal was viewed by the aid of Spectrum Analyzer *(Rhode&Schwarz FPL1003)*. In order to compensate for the frequency dependent gain, shown in Fig. 6.4, a digital gain is added for each frequency to provide a constant power over the complete spectrum.

Fig. 6.5 show the acquired spectrum, over 24-hour duration, without calibration as opposed to Fig. 6.6 which shows gain-calibrated receiver acquired spectrum. It can be seen that at specific frequencies the receiver gain is positive which may cause the probability of false alarm to increase and at other frequencies the receiver gain is negative which may

decrease the probability of detection. Both conditions are indesirable for Spectrum Sensing application.

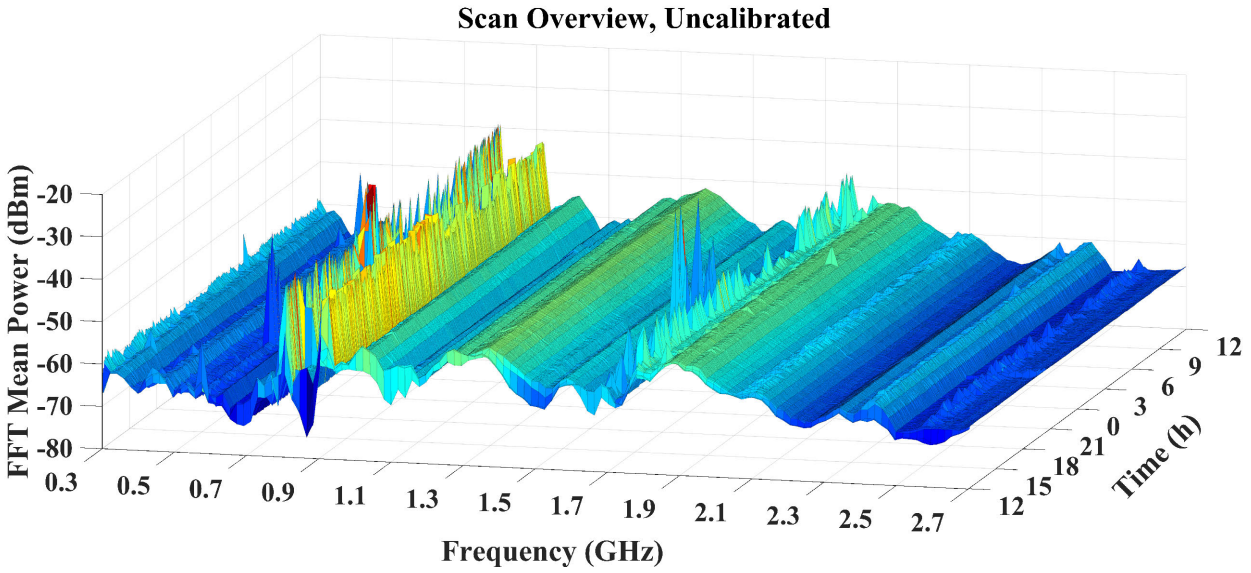

Fig. 6.5: 24 hours spectrum scan with blade-rf SDR, Uncalibrated, from 300 MHz to 3.0 GHz, power measurement (dBm).

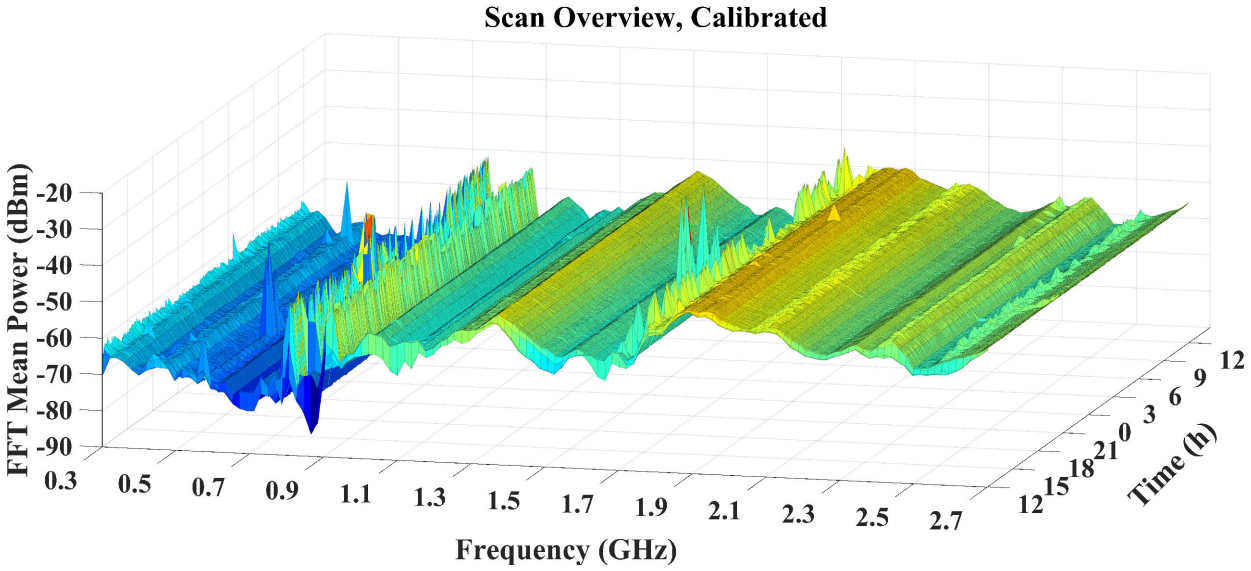

Fig. 6.6: 24 hours spectrum scan with blade-rf SDR, Calibrated, from 300 MHz to 3.0 GHz, power measurement (dBm).

6.3.2 I/Q Imbalance

The imbalance between the I/Q receiver gains α_{RI} and α_{RQ} is the Rx gain imbalance, ρ_{Rx}:

$$\rho_{Rx} = |1 - \frac{\alpha_{RQ}}{\alpha_{RI}}| \tag{6.6}$$

and the imbalance between I/Q receiver phases ϕ_{RI} and ϕ_{RQ} is the Rx phase imbalance θ_{Rx}:

$$\theta_{Rx} = |\phi_{RI} - \phi_{RQ}| \tag{6.7}$$

In the same fashion for the transmitter, ρ_{Tx} and θ_{Tx} can be defined.

As shown in Fig. 6.7, the transceiver has an internal loopback mode. This mode does not include the low-noise amplifier (LNA) of the receiver nor the power amplifier (PA) of the transmitter. Therefore, the internal loopback mode is chosen to calibrate the I/Q imbalance.

The QPSK baseband transmit signal, $x_{TBB}(t)$, shown in Fig. 6.7, is prepared using MATLAB, then it is uploaded to the SDR's LMS6002 transmitter. The digital baseband signal received, $x_{RBB}(t)$, is stored and processed by MATLAB. The $x_{RBB}(t)$ signal contains the I/Q imbalance effects introduced by the AFE of the transmitter and the AFE of the receiver.

Using the internal loopback mode it is possible to independently estimate the transmitter and the receiver RF impairments [Nassery12]. This can be done, as shown in Fig. 6.7, by operating the transmitter and the receiver at different carrier frequencies: ω_{ct} and ω_{cr} respectively.

As shown in Fig. 6.8, receiving a single tone, designated "Tx Signal", will be accompanied by multiple undesired tones due to nonidealities. The Transmitter is programmed to operate with a carrier frequency, ω_{ct}, of 2.4 GHz and the transmitted signal is a sinusoid at 1.25 MHz. The receiver carrier frequency, ω_{cr}, is shifted by 3.75 MHz with respect to the transmitter. As shown in Fig. 6.8, the correctly received signal will be at 5 MHz (3.75+1.25 MHz) and the undesirable tones are:

- Receiver DC offset component at 0 Hz,
- Transmitter I/Q Imbalance component at 2.5 MHz (3.75-1.25 MHz),
- Receiver I/Q imbalance at -5 MHz (-3.75-1.25 MHz).

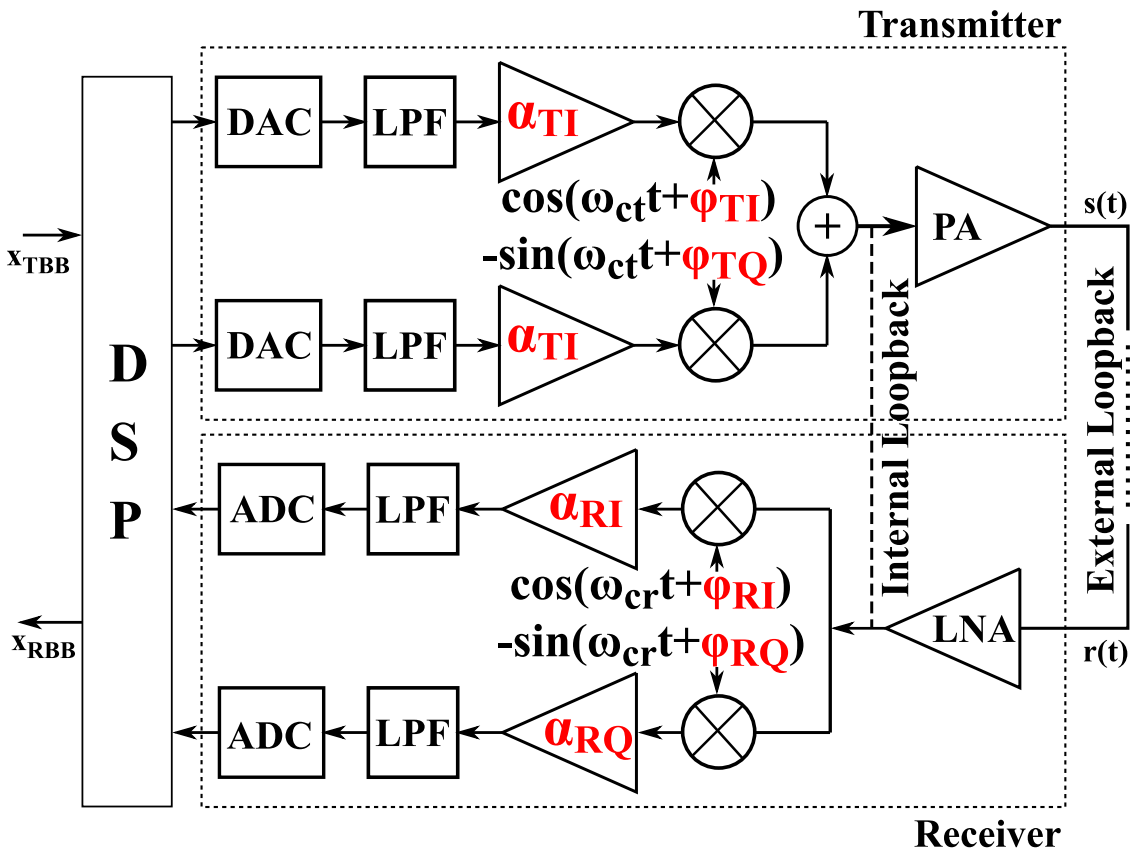

Fig. 6.7: The RF analog front-end of a Software Defined Radio Transceiver including gain and phase I/Q mismatch, DC-offset and frequency dependent gains. Normally $\omega_{ct} = \omega_{cr} = \omega_0$ the desired carrier frequence

In order to calibrate the I/Q Imbalance, the bladeRF board has a compensation circuit implemented in a Field-Programmable Gate Array (FPGA) to pre-process, in case of transmission, or post-process, in case of reception. Using this hardware we can compensate the gain and phase mismatch values: ρ and ϕ respectively, of the receiver and the transmitter [Diaz-Rizo18]. This compensation can be done using four parameters varying the mismatch within a defined range. The calibration range is $\pm 10°$ for phase difference, and $\pm 100\%$ for gain attenuation with 8192 steps for each parameter. The values that minimize the I/Q imbalance for the transmitter and the receiver are found and used for calibration. In addition to the automatic DC-offset calibration, the transmission of sinusoidal signal through the I/Q-mismatch calibrated transceiver is shown in Fig. 6.8. The calibrated settings showed 5 dB

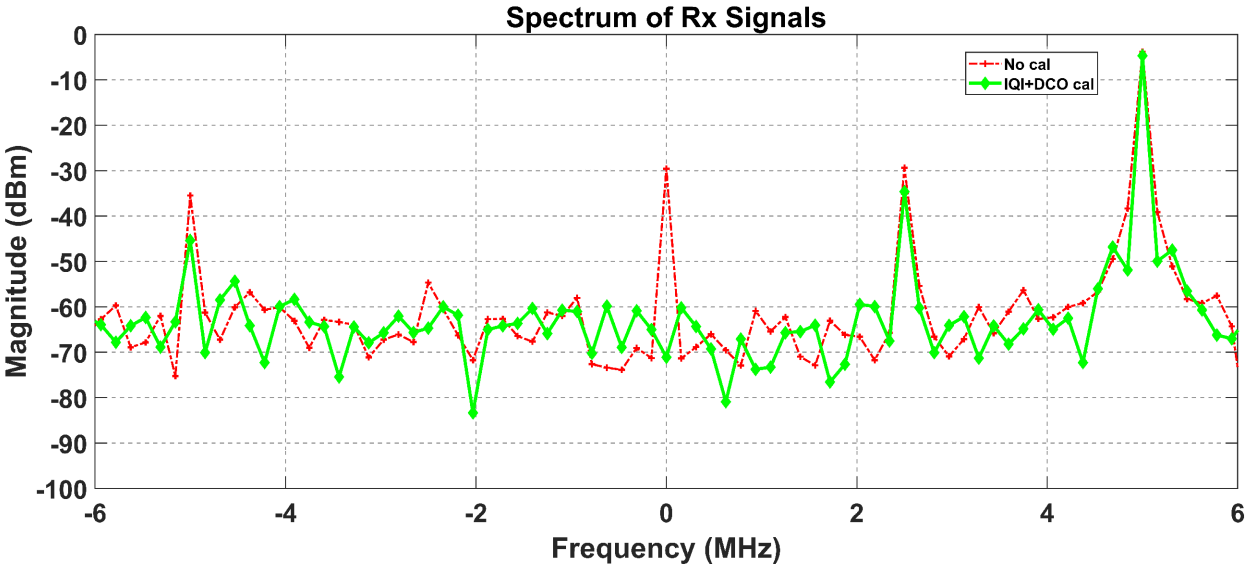

Fig. 6.8: Baseband spectrum of a received sinusoidal signal before and after DC-offset and I/Q imbalance calibration

improvement in the transmitter I/Q imbalance component and 10 dB improvement in the receiver I/Q imbalance component.

6.4 Measurements Results

In this section we present the effect of I/Q imbalance on the performance of Energy Detection. The Spectrum sensing performance is evaluated via the probability of Detection, P_D, the probabilty of False Alarm, P_{FA} and the Receiver Operating Characteristics, RoC. As shown in Section 7.3.1, it is possible to set the receiver to have a specific mismatch for gain and phase and to study its impact on the overall performance of spectrum sensing. From the calibration procedure described in the previous section, the settings producing the lowest I/Q imbalance are considered the reference mismatch value. All reported mismatch values are relative to this reference.

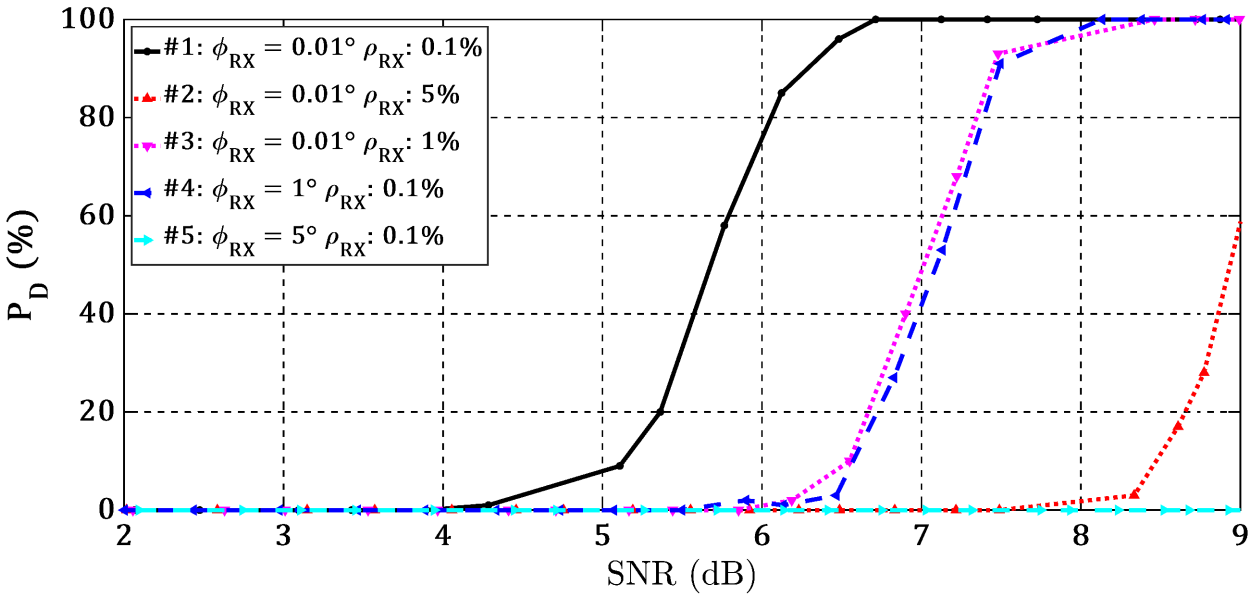

Fig. 6.9: P_D vs SNR (dB) of PU for various imbalance values (gain and phase). The SNR of the blocker is fixed and the desired $P_{FA} = 10\%$.

6.4.1 Probability of Detection vs Signal SNR

Figure 6.9 shows the probability of detection, P_D, in function of the Signal-to-Noise Ratio (SNR) of the sensed channel. The noise power is estimated by measuring the received signal power while the transmitter is idle. The signal power is computed as the difference between the received signal power while the transmitter is active and the noise power. In Figure 6.9, the SNR at which the P_D drops to unacceptable range is called the SNR wall. Having a lower SNR wall is desired as it translates to that the system is able to perform even in low SNR environment. The best curve is for the case with almost full compensation of gain and phase mismatch. The $\{\rho_{RX} = 0.1\%, \phi_{RX} = 1°\}$ and $\{\rho_{RX} = 1\%, \phi_{RX} = 0.01°\}$ curves - which can be considered acceptable - represent a full compensation in one mismatch with a low mismatch in the other quantity. A large mismatch in one quantity is sufficent to dramatically degrade the performance.

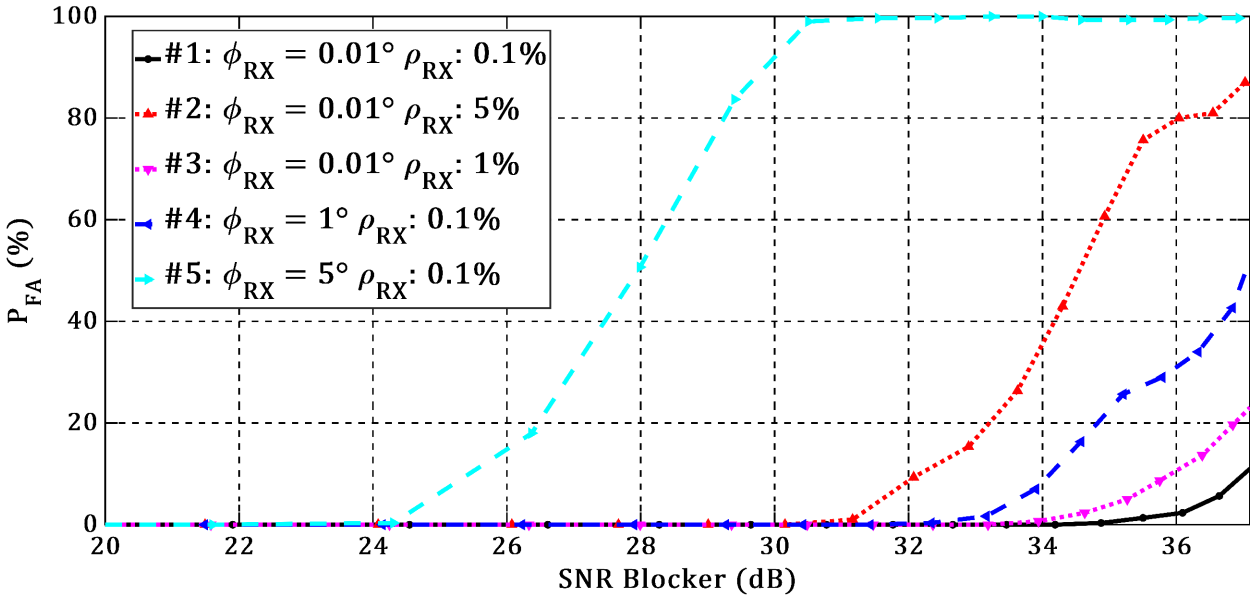

Fig. 6.10: I/Q Imbalance on P_{FA} when a blocker signal is presented, The SNR of the blocker is said ($SNR_{Blocker}$). Fix $P_D = 90\%$.

6.4.2 Probability of False Alarm vs Blocker SNR

Figure 6.10 shows the receivers performance under I/Q Imbalance when a blocker signal at the mirror frequency is presented. The higher the SNR of the blocker (image channel) the more vulnerable the system is to has a high false alarm probability. Again the calibrated curve shows the best performance with respect to Image to Noise Ratio (INR) and the $\{\rho_{RX} = 0.1\%, \phi_{RX} = 1°\}$ and $\{\rho_{RX} = 1\%, \phi_{RX} = 0.01°\}$ curves can be considered acceptable.

6.4.3 Receiver Operating Charactersitics

The ROC curve allows us to choose the threshold that achieves the needs of the application. This performance metric shows the trade-off between P_D and P_{FA} given a SNR value. The detector performance can be optimized by maximizing the value of P_D and minimizing P_{FA} [Fawcett01]. So having the curve at the top left corner is desired. As the other metrics the calibrated curve is the optimum, the $\{\rho_{RX} = 0.1\%, \phi_{RX} = 1°\}$ curve still falls in the $P_D >$ 90%-$P_{FA} < 10\%$ region but even the $\{\rho_{RX} = 1\%, \phi_{RX} = 0.01°\}$ curve is not acceptable. The ROC shows more vulnerability to gain mismatch. All measurements performed at 3GHz. It

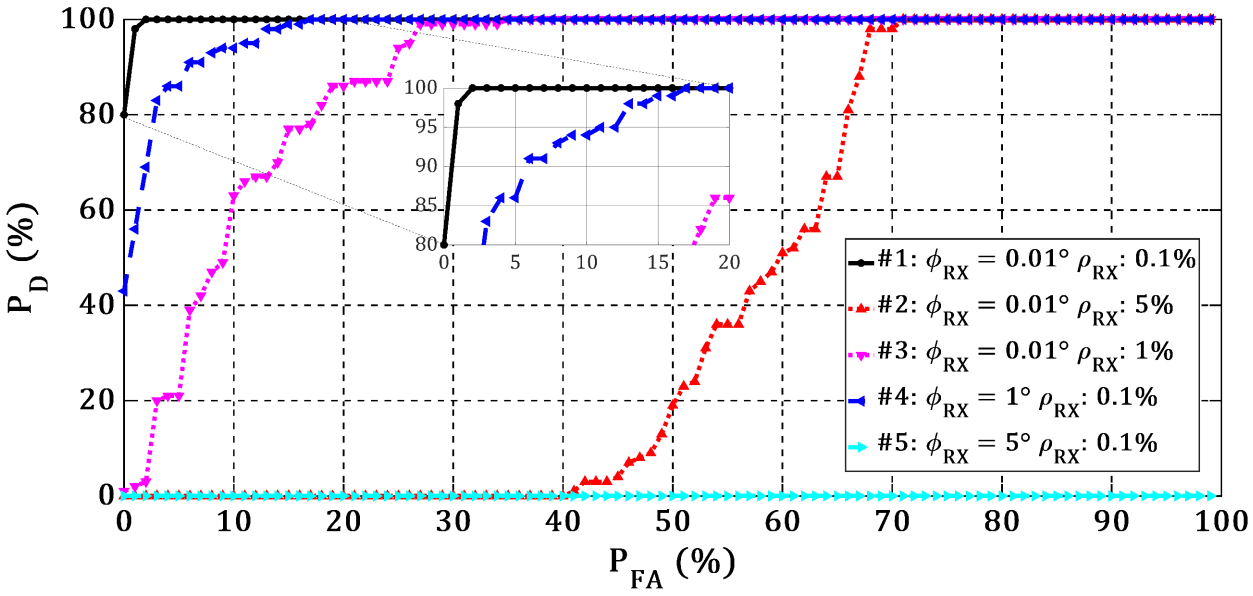

Fig. 6.11: ROC curves for different receiver I/Q Imbalance values, transmitter is calibrated for all. The receiver amplification gain is -4 dB and the transmitter is 30 dB, SNR fix to 6.31 dB.

should be emphasized that each center frequency setting requires a different set of calibration parameters.

6.5 Conclusion

This chapter reports a study of the impact of the I/Q imbalance on the SDR platform performing energy detection for a spectrum sensing application. A pipelined sensing procedure was presented, with 41.4 $/mu$ S sensing time for a 20 MHz band and aggregated 3.47 mS sensing time for 2.7 GHz band. Calibrations were made to the SDR platform used in this study to equalize the frequency-dependent AFE gain of both the transmitter and receiver as well as to compensate the gain and phase mismatch. The same calibration methodology was used to set the phase and gain mismatch to different specific values and evaluate the spectrum sensing performance at each setting. The scenarios of the two energy detection hypotheses were chosen to exploit the I/Q imbalance effect on the performance. The settings with higher I/Q Imbalance increased misdetections (decreased P_D) because the threshold to

detect a busy channel is selected higher in order to obtain a desired P_{FA}. There is a noted vulnerbilty to gain mismatch more than that to phase mismatch, and in cases with high mismatch in either quantity the performance is rendered unacceptable even if the offset of the other quantity is fully compensated.

Chapter 7

RF-EMF Exposure Effect on the Physiological Parameters of Neonates

7.1 Introduction

The term neonate refers to any newborn aged less than 28 days [Organization19b]. The World Health Organization (WHO) reported this neonatal period to be the most vulnerable period in childhood for all newborns; however, infants born prematurely (before 36 weeks of gestational age) or with a low birth weight (less than 2.5 kg) are at even higher risk [Organization19b]. High-risk neonates require medical assistance and continual monitoring; therefore, they are placed in the Neonatal Intensive Care Unit (NICU), where they can spend anywhere from a few weeks to several months depending on their condition. Because of their prematurity, and therefore their rapid development, these infants are especially susceptible to environmental factors, which may affect their internal homeostatic balance and normal growth development [Knobel07, Nair03, Darcy08, Antonucci09]. They are kept in sterile incubators that regulate temperature, humidity, light, and noise exposure; however, most do not control or monitor radiofrequency electromagnetic-field (RF-EMF) exposure [Antonucci09].

RF-EMF waves are created by electrical wiring, wireless communications devices, and electronic equipment to name a few sources, meaning that humans are exposed to them in

their lives daily. The most widely used international standards for exposure limits are set by the IEEE Standards Association under the C95.1 standard, which measures RF-EMF dosimetry based on a specific absorption rate score [IEEE19].

The NICU is a high RF-EMF environment because of the medical equipment in use; sources include wireless communication devices, incubator motors and warming systems, and medical devices such as syringe pumps [Calvente17]. The effects of RF-EMF exposure on neonates are not well understood, and studies have not yet proved or disproved a correlation between RF-EMF exposure and variations in neonatal physiological parameters.

In a 2008 study, Bellieni *et al.* found that RF-EMFs produced by incubator warming system motors affected neonatal heart rate variability [Bellieni08]. A literature review conducted in 2019 found that RF-EMF levels produced by incubator motors and experienced by the infants were reported at levels high enough to affect melatonin production [Bellieni19]. Studies have shown conflicting evidence on the association between the incidence of childhood leukemia and RF-EMF exposure in early childhood [Calvente10, Söderberg02]. Recently, Calvente *et al.* conducted a study to confirm that RF-EMF levels measured in an NICU were below International Commission on Non-Ionizing Radiation Protection (INCIRP) reference levels for adults; however, they recommended adopting a prudent avoidance strategy around neonates until further research can characterize RF-EMF levels and adverse health effects in infants [Calvente17]. The WHO developed the International EMF project to monitor scientific literature on health effects correlated to exposure to RF-EMFs, as well as proposed a research agenda to guide research and funding in this area based on identified needs [Organization19a]. The WHO's research agenda identified that research into the developmental and adverse health effects of RF-EMF exposure in children was a high-priority need [Organization19a].

This chapter discusses the design and architecture of a system intended to monitor the RF-EMF environment in an NICU, and in parallel collect physiological data of neonatal patients. These physiological and RF-EMF data could then be analyzed to determine correlations between fluctuations in the spectrum and physiological variations in the patient.

Fig. 7.1: Simultaneous Measurement of RF signals and the Physiological Parameters of Neonates.

7.2 System Architecture

Two data acquisition systems were implemented in this project to separately collect RF-EMF spectrum-scanning data and neonate physiological data in parallel. Both systems were designed to collect data over several hours and then compile the data on one central computer for signal processing and statistical analysis. Fig. 7.1 illustrates the entire architecture of both systems.

7.2.1 Physiological Data Acquisition System

Data collection was conducted in the NICU of Antoine-Béclère Hospital in Clamart, France. To acquire the physiological data of neonates, it was necessary to tap into the monitoring system already in place in this NICU. All the incubators continuously measure several physiological parameters of each neonate and send the data to the central nursing station (CNS). The parameters collected and used in the present study are heart rate (HR), respiration rate, oxygen saturation, and time in apnea (AP) [Lofts18]. The CNS communicates with the hospital network using a Health Level 7 (HL7) standardized messaging system; therefore, this study developed a system in accordance with the HL7 protocol to access and transfer physiological data from the CNS to a central analysis computer [International19].

The NICE at Antoine-Béclère Hospital uses Nihon Kohden CNS monitors to visualize the physiological parameters of patients in nearby rooms in real time. These monitors continuously record data but only save the past 120 hours of each patient; thus, a system was built to interface with the hospital network and receive data through HL7 messages, which was to be saved in a database for future analysis. This HL7 acquisition system also allowed for enhanced data visualization capabilities than was possible directly on the Nihon Kohden monitors, such as simultaneous visualization of multiple parameters at high resolution.

Alongside collecting physiological data from the hospital system, a manual logging system was developed for the NICU nurses to record certain events that occurred during data collection [Bellieni08].

Furthermore, a timesheet was used to record when infants were crying, feeding, and sleeping; when parents were visiting; when nurses were in the room; and other abnormal events. These timestamped logs could then be used to explain certain variations in the RF-EMF data, such as an increase in the 4G bandwidth when parents entered the room with cellphones. They could also be used to understand the physiological data; for example, an increase in an infant's HR may be explained by periods of crying.

7.2.2 RF-EMF Data Acquisition System

The second data acquisition system is used to monitor variations in the electromagnetic spectrum in the NICU environment. A Nuand bladeRF software-defined radio (SDR) board was configured and programmed as a spectrum-sensing device [nuand18]. It was selected as the RF receiving device because of its frequency band range and the ability to set the channel width. This board has a frequency range that covers the ultra-high frequency band, from 0.3 to 3.8 GHz. This band range was selected because it contains most of the frequencies of interest and that would be present in the hospital environment. The system was tested in a lab while exposed to controlled wireless communications devices to determine the expected power levels for various transmitting and receiving functions. This was also done to ensure that the device was sensing each function in the correct frequency band.

Using the bladeRF board and an antenna, with a range from 0.7 to 2.6 GHz, it took approximately 5 minutes to scan the full extent of the spectrum; therefore, a MATLAB [MathWorks18] script was created to repeatedly run a scan every 5 minutes for an extended period [Lofts18]. The scanning laptop, bladeRF board, and antenna would then be left in a patient's room for 12-24 hours to scan the spectrum while simultaneously collecting physiological data through the HL7 acquisition system. Because of the bladeRF board's internal architecture, an I/Q imbalance, DC offset, and frequency dependent amplifier gain existed on the receiver chain that needed to be calibrated for. These calibrations were incorporated into the MATLAB spectrum scanning script, the calibration curve for which can be seen in Fig. 6.4.

7.3 Data Analysis

For data analysis, two sets of parameters are defined:

1. Spectrum Parameters
   - Average power in the range 0.3-2.7 GHz
   - 2G band average power

- 3G band average power
- 4G band average power
- WiFi band average power

2. Physiological Parameters
   - Heart Rate
   - Respiration Rate
   - Time in Apnea
   - Oxygen Saturation

7.3.1 Preliminary Data Visualization

Three rounds of data collection have currently been completed, each on a different patient and at different times. The first was completed for 10 hours to ensure that the system operated properly; the second was performed for 20 hours; and the third was performed for 24 hours. The units of the collected data were dBm; thus, the RF-EMF data were plotted to show the changing power levels at each frequency over the recorded time, as shown in Fig. 7.2. Fig. 7.3 presents a spectrogram with labeled bands of the frequency spectrum being measured.

Subsequently, statistical analysis was performed to mathematically determine cross correlations between physiological and spectrum parameters, as well as to uncover patterns across different rounds of data collection. Statistical properties of each parameter were also analyzed and compared across separate rounds of data collection [Smith19].

7.3.2 Statistical Analysis Method

To more thoroughly analyze the effects of the RF spectrum, the collected spectrum data were split into five different parameters. The power in the 2G, 3G, 4G, and Wi-Fi spectrum bands were isolated as parameters, as was the average power across all frequencies. The statistical analysis of the project data was undertaken in RStudio [RStudio Team15]. The data collected in this study were time-series data, and therefore the first step in the analysis was to determine the time-series characteristics of each parameter. It was assumed that

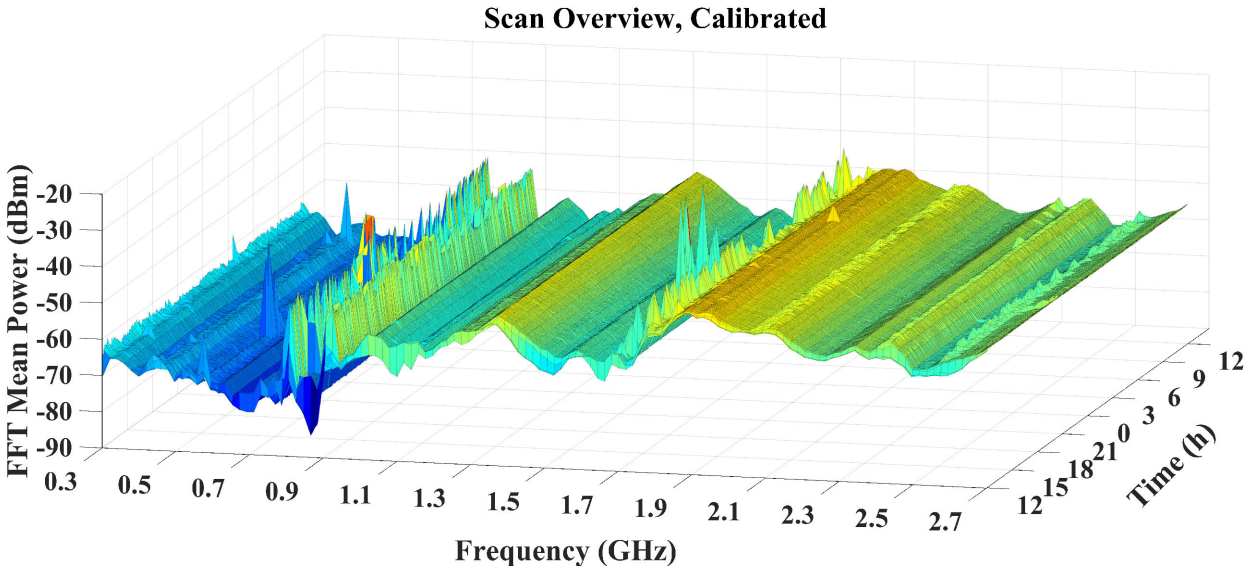

Fig. 7.2: 24-hour calibrated spectrum scan surface plot.

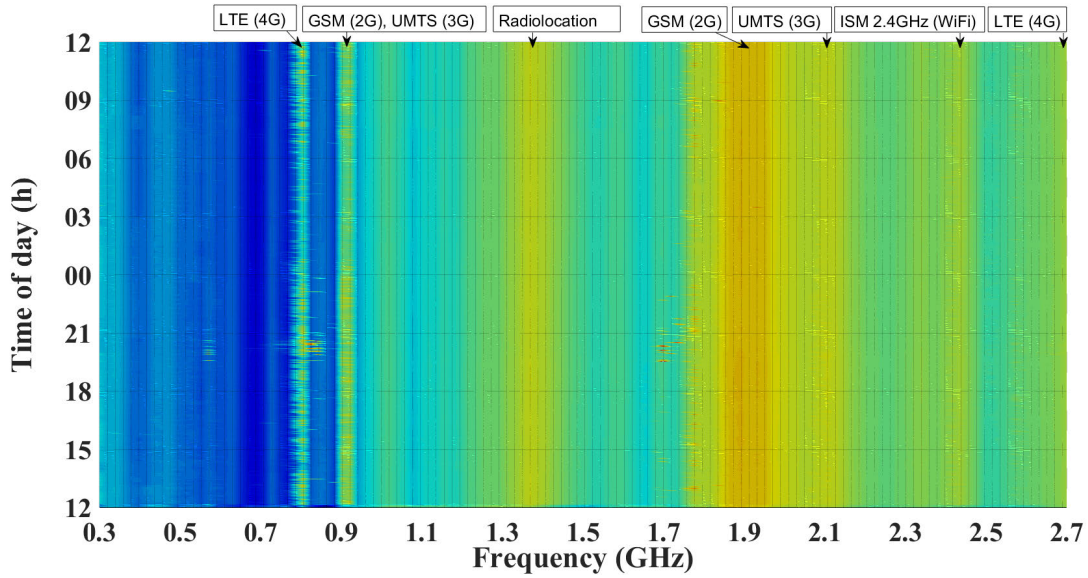

Fig. 7.3: 24-hour scan showing spectrogram of measured frequency bands.

because the data collection times were in the order of hours and no consistent cyclical activity existed in the NICU, no significant seasonality would be present, which was confirmed visually.

Next, the data were analyzed using both an augmented Dickey-Fuller (ADF) test for unit root presence and a Kwiatkowski-Phillips–Schmidt-Shin (KPSS) test for level and trend sta-

Table 7.1: Stationarity results of ADF and KPSS tests for collected data sets before data transformation.

	1sr Data collected	**2nd Data collected**
HR	Non-stationary	Non-stationary
RESP	Stationary	Stationary
APSEC	Stationary	Stationary
SPO2	Stationary	Stationary
Average	Non-stationary	Non-stationary
2G	Stationary	Stationary
3G	Non-stationary	Non-stationary
4G	Non-stationary	Stationary
Wifi	Stationary	Stationary

tionarity [To19a, To19b], as reported in Table 7.1. Both tests indicated that in both the first two rounds of data collection, the HR, average spectrum, and 3G parameters were non-stationary with a 5% alpha level. The 4G parameter was non-stationary in the first round of data collection and stationary in the second, and all other parameters were consistently stationary. This indicated that the 3G parameter consistently contained time sensitive variations, meaning that most activity in the RF spectrum occurred in the 3G band and some in 4G. Fig. 7.4 demonstrates the autocorrelation and trend plots of three parameters in the first set of data collection. Normally, having the autocorrelation coefficients between -0.2 and 0.2 expresses stationarity of the signal. The statistical properties that indicate stationarity and non-stationarity, such as time varying mean and standard deviation, autocorrelation, and trend lines, can be visualized in these plots.

To make all the parameters stationary, a difference transformation was performed, which is given in (7.1):

$$y(t) = x(t) - x(t-1) \tag{7.1}$$

where $y(t)$ is the newly differenced parameter and $x(t)$ is the parameter undergoing transformation [Bourke19]. Figs. 7.5 and 7.6 present autocorrelation plots of the HR data taken during the first data collection before and after transformation. It should be noted that the autocorrelation plots for each parameter were highly similar between different data collection

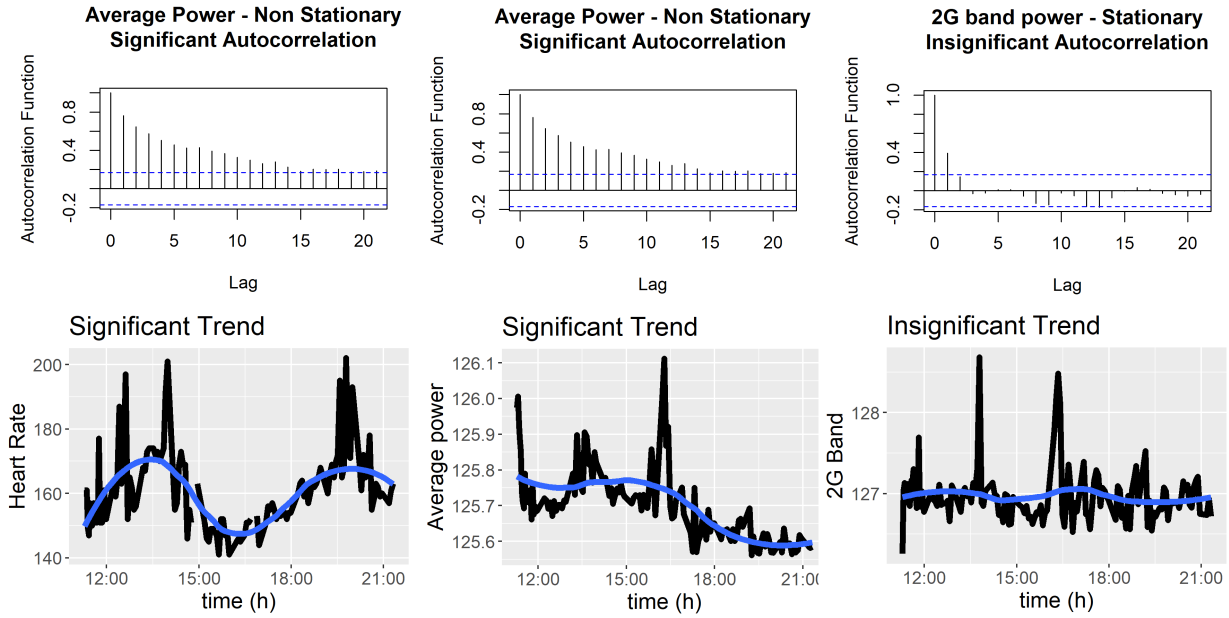

Fig. 7.4: Shows 3 parameters of the first set of collected data, the HR, average power, and 2G power. The first two are non-stationary while the third is stationary, respectively. Differences in the statistical properties of these stationary and non-stationary parameters such as trends, autocorrelation, and time varying mean and standard deviation can be observed.

rounds. The transformation was performed on all parameters whether they were originally stationary or not for consistency when correlation analysis was performed.

Subsequently, the differenced parameters were tested again with the ADF and KPSS tests and determined to be both level and trend stationary [To19a, To19b]. Once stationary, each of the spectrum parameters was cross correlated with each of the physiological parameters to determine the strength of correlation between them at differing time lags. The cross correlation is given in (7.2):

$$r(d) = \frac{\sum_i [(x_i - \mu_x) * (y_{i-d} - \mu_y)]}{\sqrt{\sum_i (x_i - \mu_x)^2} \sqrt{\sum_i (y_{i-d} - \mu_y)^2}} \tag{7.2}$$

where r is the correlation coefficient at time lag d, and μ_x and μ_y are the means of each series respectively [Bourke19, Grogan19, Brownlee19, Statistical Methods19].

After all the parameters are transformed, they all became stationary. Cross-correlation analysis now can be performed, as presented in the next section.

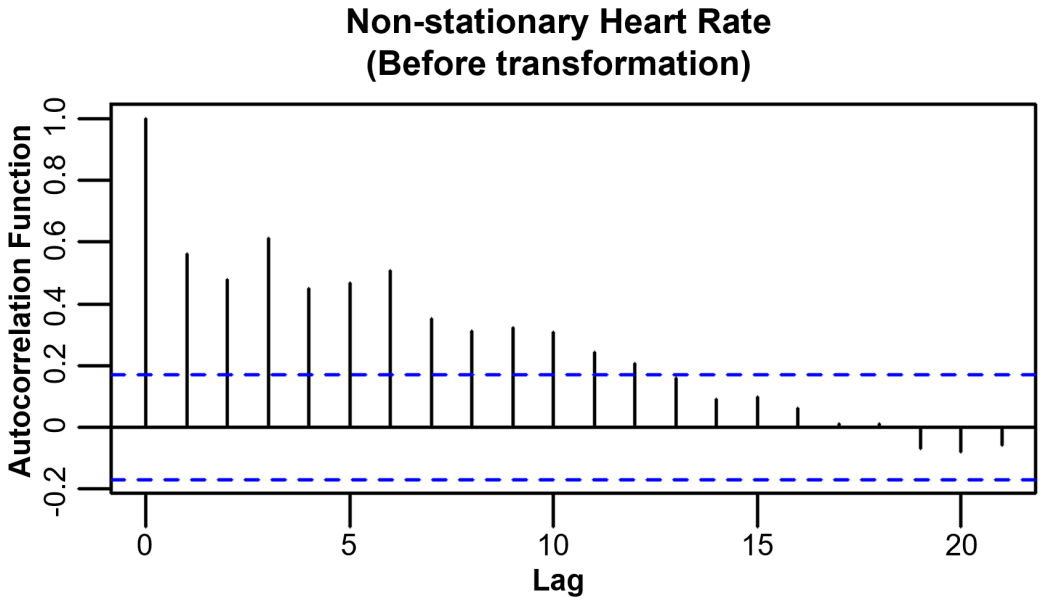

Fig. 7.5: Non-stationary heart rate data before transformation, as many of the autocrrelation coefficients are out of -0.2 and 0.2 range.

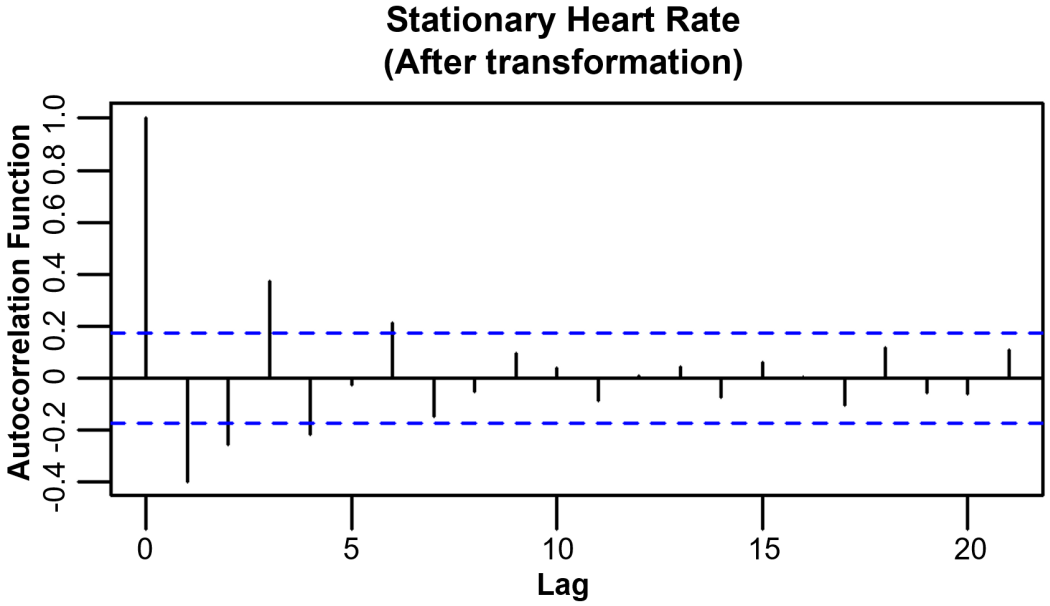

Fig. 7.6: Stationary heart rate data after transformation, as all of the autocrrelation coefficients are within -0.2 and 0.2.

7.4 Results

Figs. 7.7 to 7.11 show the results of the cross-correlation analysis for the first collected data set. Each plot corresponds to a spectrum parameter and the four lines on each plot correspond to each of the physiological parameters correlated against that spectrum parameter. Notably, all plots show both the positive and negative time lags, because the method of plotting a negative time lag would imply causation by the physiological parameters, and a positive time lag would imply causation by the spectrum. For the purposes of this study, finding correlations was focused on the positive time lag, but both were analyzed to demostrate that no spurious correlation occurred either way.

Figs. 7.7 to 7.11 reveal that no significant correlation existed between any of the physiological and spectrum parameters. This was consistently found in the second dataset collected for 20 hours: the correlations between all parameters consistently stayed between the -0.2 and 0.2 coefficient bounds and never exceeded a coefficient magnitude of 0.4.

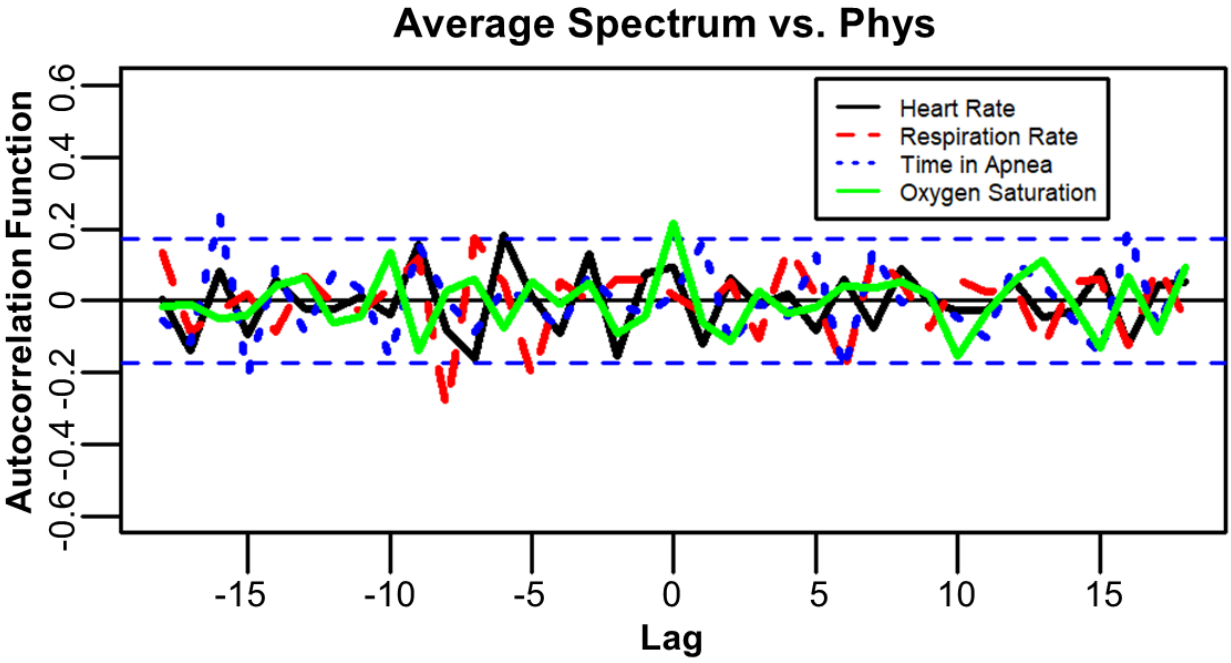

Fig. 7.7: Average spectrum correlated to physiological parameters.

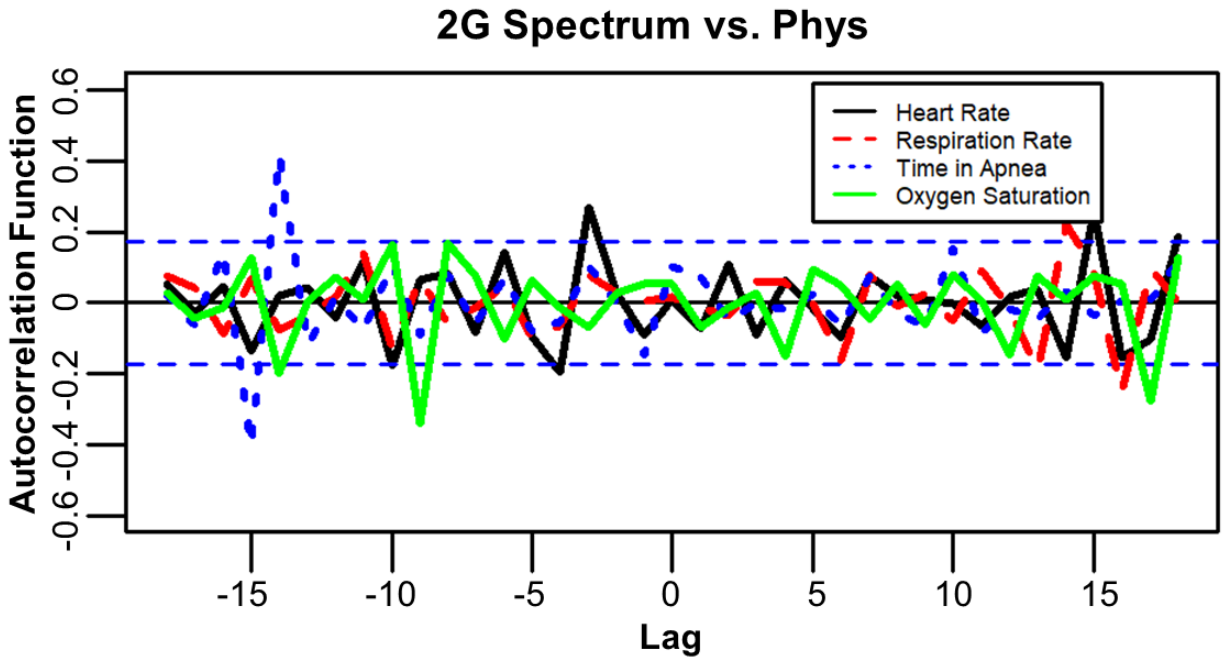

Fig. 7.8: 2G spectrum correlated to physiological parameters.

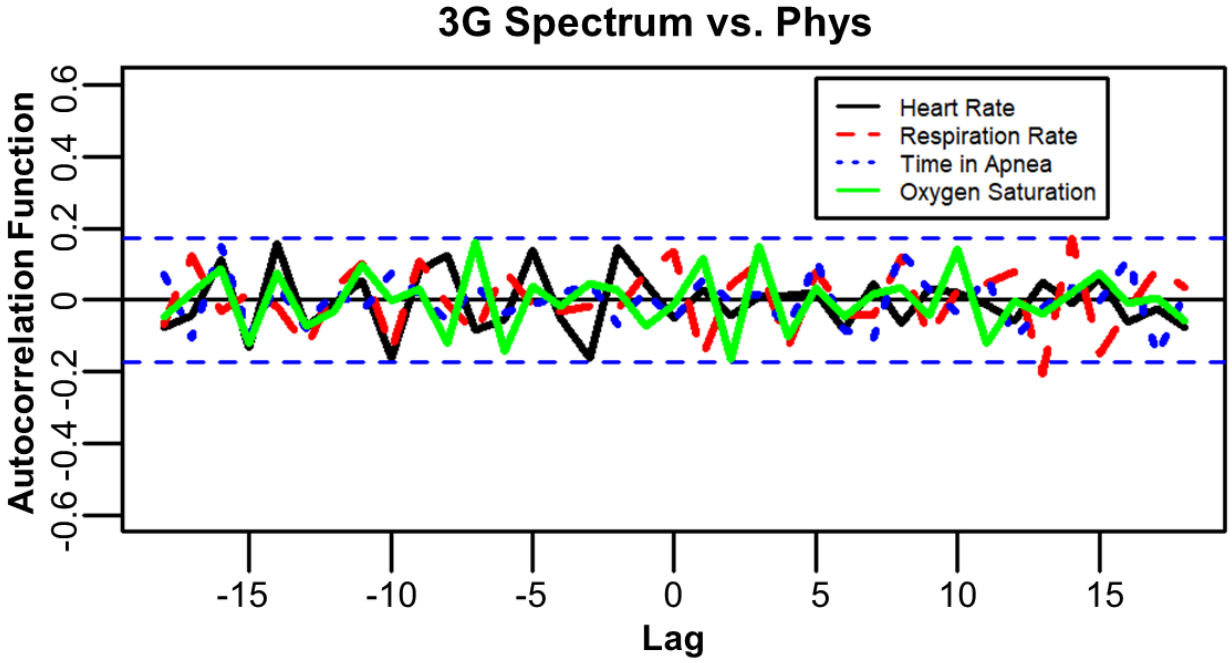

Fig. 7.9: 3G spectrum correlated to physiological parameters.

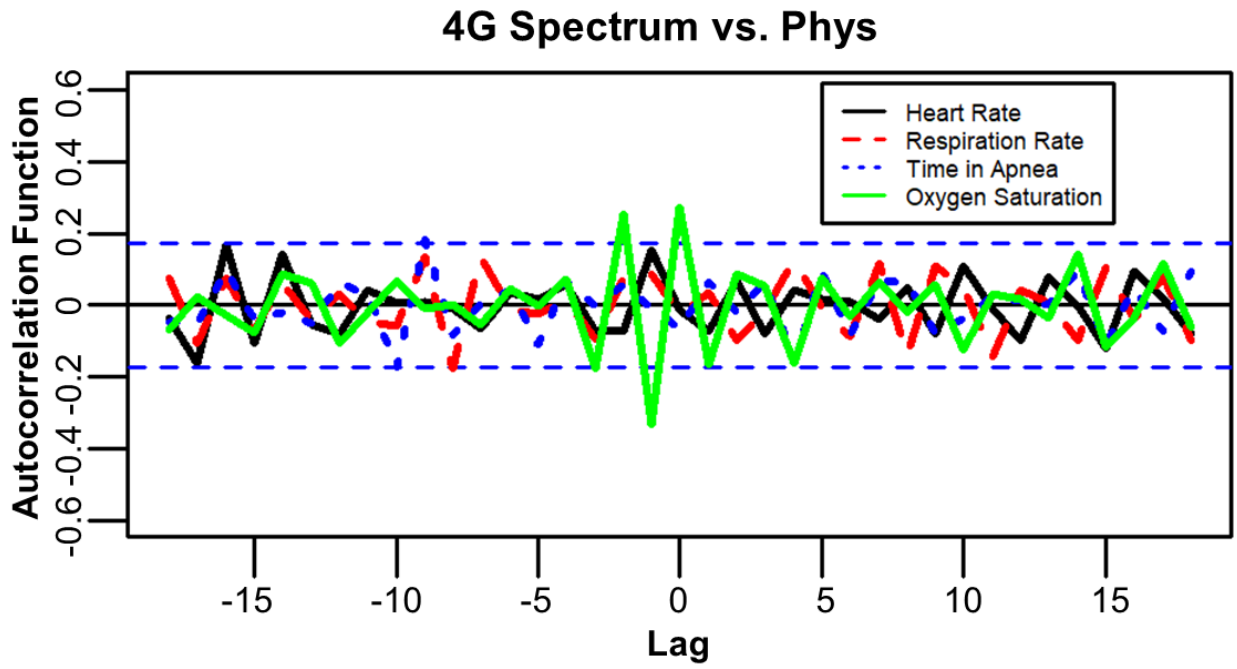

Fig. 7.10: 4G spectrum correlated to physiological parameters.

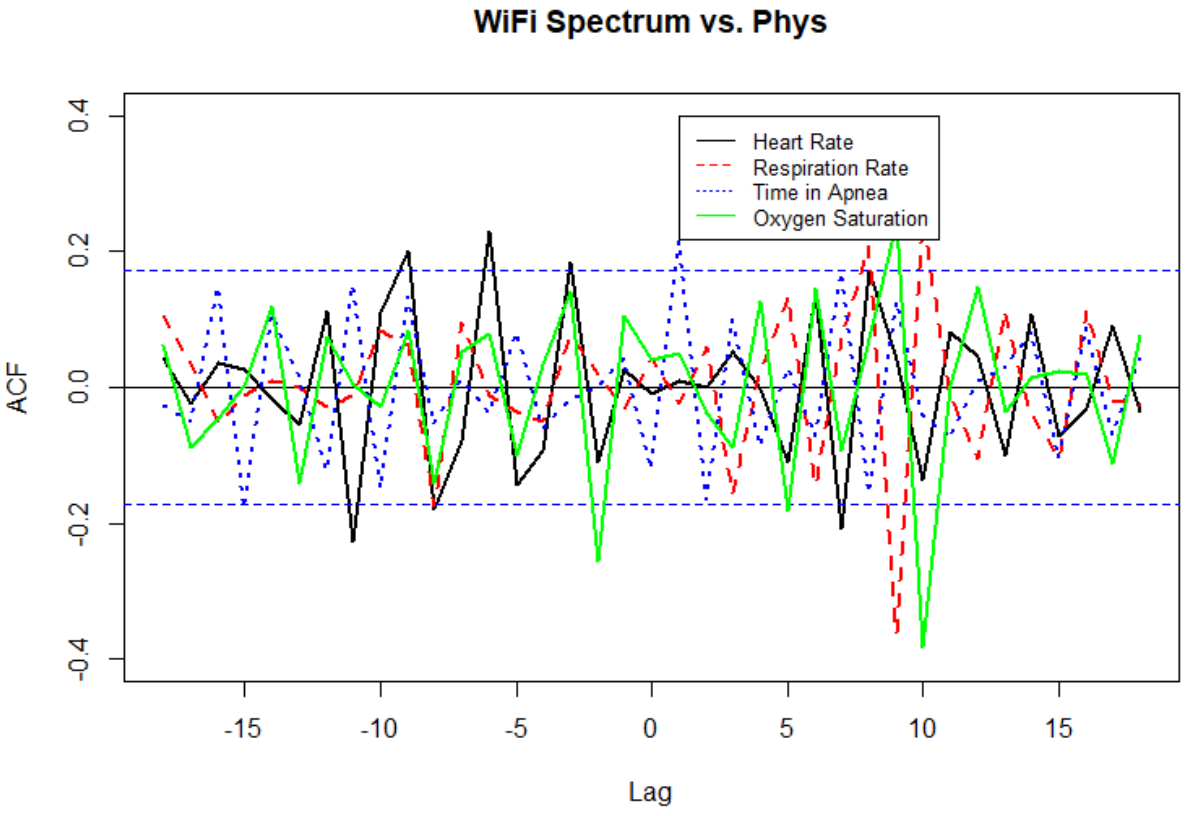

Fig. 7.11: Wi-Fi spectrum correlated to physiological parameters.

7.5 Discussion

Our study showed no correlation between the spectrum parameters and the neonates' physiological parameters. It should be noted however that we did not expose the neonates to any specific RF-EMF signals, they were only exposed to the ambient RF-EMF which is relatively weak in a hospital environment, specially a neonates intensive care unit.

This study recommends that future studies analyze the entire NICU hospital wing for RF-EMF exposure levels, as well as compare exposure inside and outside of the incubators. Calvente *et al.* proposed a method for mapping RF power levels throughout a hospital wing to determine if the room layout affected exposure and how power levels differed in patients' rooms compared with at nursing stations [Calvente10]. It should also be noted that because of the vulnerability of the neonates under study, exposure levels were only monitorable outside of their incubators. Therefore, measurements should be made to compare power levels inside and outside of an empty incubator to determine whether any shielding effects occur from the incubator itself.

In addition future studies are recommended to measure and analyze further physiological statuses of neonates in the NICU. Obtaining raw electrocardiogram and respiratory cycle signals rather than parameters already calculated at the hospital would provide more information concerning neonates' health status, as well as allow the use of signal processing and feature detection methods when the physiological data are analyzed. Moreover, information about each neonate's individual condition would provide insights into how to more effectively analyze their physiological signals in relation to spectrum fluctuations. In this case, patient confidentiality in terms of medical information must be discussed with the hospital and appropriate consent must be obtained.

7.6 Conclusions

Relevant studies have not been able to conclude the effects of RF-EMF exposure on neonatal health and development. This system was designed to monitor neonates' physiological data as well as their exposure to different RF-EMF frequencies over an extended period. The

system was implemented for four tests that range from 10 to 26 hours in duration and the data were plotted for visual analysis. Statistical testing was then performed to characterize the time-series data, determine the stationarity of the parameters. A difference tansformation was applied to all parameters to enforce stationarity and then cross-correlation analysis was performed. In all rounds, the analysis revealed no consistent correlation between any of the parameters over a magnitude of a 0.2 correlation coefficient.

Chapter 8

Conclusions and Future Directions

In chapter 3, we presented an efficient realization of a tunable RF band-pass $\Delta\Sigma$ ADC with wide tuning range. Bandpass RF ADC based architectures were introduced. A tunable band-pass $\Delta\Sigma$ ADCs architecture was proposed. The proposed architecture was fabricated and the measured performance are well suited for spectrum sensing applications.

In chapter 5 the digital back end (DBE) of the proposed architecture in chapter 4 was implemented to process the output of the AFE chip presented in chapter 3. The down-conversion mixer and decimation filter implementation and validation were discussed. We also showed the spectrum sensing processor implementation. Design optimizations were made. Finally, a test scenario of spectrum monitoring was presented to validate the implementation.

Chapter 6 reports a study of the impact of the I/Q imbalance on the SDR platform performing energy detection for a spectrum sensing application. A pipelined sensing procedure was presented, with 41.4 μS sensing time for a 20 MHz band and aggregated 3.47 mS sensing time for 2.7 GHz band. Calibrations were made to the SDR platform used in this study to equalize the frequency-dependent AFE gain of both the transmitter and receiver as well as to compensate the gain and phase mismatch. The same calibration methodology was used to set the phase and gain mismatch to different specific values and evaluate the spectrum sensing performance at each setting. The scenarios of the two energy detection hypotheses were chosen to exploit the I/Q imbalance effect on the performance. The settings with higher I/Q Imbalance increased mis-detections (decreased P_D) because the threshold

to detect a busy channel is selected higher in order to obtain a desired P_{FA}. There is a noted vulnerability to gain mismatch more than that to phase mismatch, and in cases with high mismatch in either quantity the performance is rendered unacceptable even if the offset of the other quantity is fully compensated.

In chapter 7 we presented a setup to monitor neonates' physiological data as well as their exposure to different RF–EMF frequencies over an extended period. The system was implemented for four tests that range from 10 to 26 hours in duration and the data were plotted for visual analysis. Statistical testing was then performed to characterize the time-series data, determine the stationarity of the parameters. A difference tansformation was applied to all parameters to enforce stationarity and then cross-correlation analysis was performed. In all rounds, the analysis revealed no consistent correlation between any of the parameters over a magnitude of a 0.2 correlation coefficient.

There are several interesting future directions to the work presented in this thesis:

- Integrating the whole spectrum sensing system, the RF front-end presented in chapter 3 and the digital backend implemented in chapter 5.
- Extending the digital backend implementation (chapter 5) to include hybrid spectrum sensing algorithm of energy detection and cyclostationary feature detection.
- The SDR platform utilized in chapter 6 has an internal loopback mode with choice among different nodes at the transmitter and receiver analog front-ends, this is can be used to have different levels of circuit nonlinearity, and report hardware measurements with the impact of nonlinearity on spectrum sensing performance.
- Recent publications, such as [Kulin18], uses deep machine learning to classify RF signals. A comparative study can be beneficial to show the pros and cons of machine-learning-based architectures compared to spectrum sensing based on Energy Detection.

List of Publications

1. Tamer Badran, and Hassan Aboushady. "Delta-Sigma Modulator based Spectrum Sensing Transceiver." In 2016 IEEE International Conference on Electronics, Circuits and Systems (ICECS), pp. 443-443. IEEE, 2016.
2. Hassan Aboushady, Tamer Badran, and Alhassan Sayed. "Tunable Bandpass Sigma-Delta Modulator", January 7, 2020. US Patent 10,530,385.
3. Tamer Badran, Alan R. Diaz-Rizo, Alexandre Mendy, Shadi Turk, Naceur Malouch, Ramon Parra-Michel, and Hassan Aboushady. "Energy-Detection Spectrum Sensing using an SDR Transceiver and the Effect of the I/Q imbalance on its Performance". submitted to IEEE Transactions on Circuits and Systems II: Brief Papers.
4. Tamer Badran and Hassan Aboushady. "Energy-Detection Spectrum-Sensing receiver based on $\Delta\Sigma$ ADC RF Front-end and Study of the Circuit Nonlinearity Effect on its Performance". to be submitted to IEEE Transactions on Circuits and Systems I: Regular Papers.
5. Tamer Badran, Shadi Turk, and Hassan Aboushady. "A Wideband Energy Detection Spectrum Sensing Receiver". to be submitted to IEEE Transactions on Cognitive Communications and Networks.

References

[Aboushady02] H. Aboushady. *Design for reuse of current-mode continuous-time sigma-delta analog-to-digital converters*. PhD thesis, Sorbonne University, Paris, France, 2002.

[Aboushady20] Hassan Aboushady, Tamer Badran, and Alhassan Sayed. Sigma-delta modulator, January 7 2020. US Patent 10,530,385.

[Alom17] Md Zulfikar Alom, Tapan Kumar Godder, Mohammad Nayeem Morshed, and Asmaa Maali. Enhanced spectrum sensing based on energy detection in cognitive radio network using adaptive threshold. In *2017 International Conference on Networking, Systems and Security (NSysS)*, pages 138–143. IEEE, 2017.

[Ambede17] Abhishek Ambede, A Prasad Vinod, and Shanker Shreejith. Efficient fpga implementation of a variable digital filter based spectrum sensing scheme for cognitive iot systems. In *2017 Global Internet of Things Summit (GIoTS)*, pages 1–4. IEEE, 2017.

[Antonucci09] Roberto Antonucci, Annalisa Porcella, and Vassilios Fanos. The infant incubator in the neonatal intensive care unit: unresolved issues and future developments. *Journal of perinatal medicine*, 37(6):587–598, 2009.

[Anushiya18] P Anushiya and M Suganthi. Energy detection based spectrum sensing data mining for safety-message delivery in cr enabled vanet. In *2018 2nd International Conference on Inventive Systems and Control (ICISC)*, pages 1130–1133. IEEE, 2018.

[Ashley06] Steven Ashley. Cognitive radio. *Scientific American*, 294(3):66–73, 2006.

[Ashry13] Ahmed Ashry and Hassan Aboushady. A 4th order 3.6 gs/s rf/spl sigma//spl delta/adc with a fom of 1 pj/bit. *IEEE Transactions on Circuits and Systems I: Regular Papers*, 60(10):2606–2617, 2013.

[Badran16] Tamer Badran and Hassan Aboushady. Delta-sigma modulator based spectrum sensing transceiver. In *2016 IEEE International Conference on Electronics, Circuits and Systems (ICECS)*, pages 443–443. IEEE, 2016.

[Badran20a] Tamer Badran and Hassan Aboushady. Energy-detection spectrum-sensing receiver based on $\delta\sigma$ adc rf front-end and study of the circuit nonlinearity effect on its performance. *IEEE Transactions on Circuits and Systems I: Regular Papers*, 2020. To be Submitted.

[Badran20b] Tamer Badran, Alán R. Díaz-Rizo, Alexandre Mendy, Shadi Turk, Naceur Malouch, Ramon Parra-Michel, and Hassan Aboushady. Energy-detection spectrum-sensing using an sdr transceiver and the effect of the i/q imbalance on its performance. *IEEE Transactions on Circuits and Systems II: Brief Papers*, 2020. Submitted, Pending Acceptance.

[Badran20c] Tamer Badran, Shadi Turk, Leonardo Orozco, Ramon Parra-Michel, and Hassan Aboushady. A complete wideband energy detection spectrum sensing receiver. *IEEE Transactions on Cognitive Communications and Networks*, 2020. To be Submitted.

[Beilleau09] Nicolas Beilleau, Hassan Aboushady, Franck Montaudon, and Andreia Cathelin. A 1.3 v 26mw 3.2 gs/s undersampled lc bandpass $\sigma\delta$ adc for a sdr ism-band receiver in 130nm cmos. In *2009 IEEE Radio Frequency Integrated Circuits Symposium*, pages 383–386. IEEE, 2009.

[Belfort17] Diomadson R Belfort, Sebastian YC Catunda, and Hassan Aboushady. 4th order capacitively-coupled lc-based $\sigma\delta$ modulator. *Microelectronics Journal*, 62:99–107, 2017.

[Bellieni08] CV Bellieni, M Acampa, M Maffei, S Maffei, S Perrone, I Pinto, N Stacchini, and G Buonocore. Electromagnetic fields produced by incubators influence heart rate variability in newborns. *Archives of Disease in Childhood-Fetal and Neonatal Edition*, 93(4):F298–F301, 2008.

[Bellieni19] Carlo Valerio Bellieni, Valentina Nardi, Giuseppe Buonocore, Sandra Di Fabio, Iole Pinto, and Alberto Verrotti. Electromagnetic fields in neonatal incubators: the reasons for an alert. *The Journal of Maternal-Fetal & Neonatal Medicine*, 32(4):695–699, 2019.

[Bluetooth10] SIG Bluetooth. Bluetooth core specification version 4.0. *Specification of the Bluetooth System*, 1:7, 2010.

[Boulogeorgos16] Alexandros-Apostolos A Boulogeorgos, Nestor D Chatzidiamantis, and George K Karagiannidis. Energy detection spectrum sensing under rf imperfections. *IEEE Transactions on Communications*, 64(7):2754–2766, 2016.

[Bourke19] P. Bourke. Cross correlation. `http://paulbourke.net/miscellaneous/correlate/`, Accessed: 2019.

[Brownlee19] J. Brownlee. How to remove trends and seasonality with a difference transform in python. `https://machinelearningmastery.com/remove-trends-seasonality-difference-transform-python/`, Accessed: 2019.

[Calvente10] I Calvente, MF Fernandez, J Villalba, N Olea, and MI Nunez. Exposure to electromagnetic fields (non-ionizing radiation) and its relationship with childhood leukemia: a systematic review. *Science of the total environment*, 408(16):3062–3069, 2010.

[Calvente17] I Calvente, A Vázquez-Pérez, MF Fernández, MI Núñez, and A Múñoz-Hoyos. Radiofrequency exposure in the neonatal medium care unit. *Environmental research*, 152:66–72, 2017.

[Chatziantoniou15] Eleftherios Chatziantoniou, Ben Allen, and Vladan Velisavljevic. Threshold optimization for energy detection-based spectrum sensing over hyper-rayleigh fading channels. *IEEE Communications Letters*, 19(6):1077–1080, 2015.

[Cherry00] J.A. Cherry, W.M. Snelgrove, and Weinan Gao. On the design of a fourth-order continuous-time LC delta-sigma modulator for UHF A/D conversion. 47(6):518–530, June 2000.

[Chhagan18] Charan Chhagan et al. Double threshold-based energy detection spectrum sensing scheme by considering the sensing history in confusion region. In *2018 5th International Conference on Signal Processing and Integrated Networks (SPIN)*, pages 518–521. IEEE, 2018.

[Cohen17] Deborah Cohen and Yonina C Eldar. Sub-nyquist cyclostationary detection for cognitive radio. *IEEE Transactions on Signal Processing*, 65(11):3004–3019, 2017.

[Darcy08] Ashley E Darcy, Lauren E Hancock, and Emily J Ware. A descriptive study of noise in the neonatal intensive care unit: ambient levels and perceptions of contributing factors. *Advances in Neonatal Care*, 8(5):S16–S26, 2008.

[Das15] Soumyadip Das and Sumitra Mukhopadhyay. Soc fpga implementation of energy based cooperative spectrum sensing algorithm for cognitive radio. In *2015 6th International Conference on Computers and Devices for Communication (CODEC)*, pages 1–4. IEEE, 2015.

[Diaz-Rizo18] Alan-Rodrigo Diaz-Rizo. Correction of I/Q Imbalance in Software Defined Radio Transceivers, 2018. M.Sc. Thesis, CINVESTAV, Guadalajara, Mexico.

[Ejaz18] W. Ejaz and M. Ibnkahla. Multiband spectrum sensing and resource allocation for iot in cognitive 5g networks. *IEEE Internet of Things Journal*, 5(1):150–163, Feb 2018.

[Elanagai17] G Elanagai and C Jayasri. Implementation of network security based data hauling by collaborative spectrum sensing in cognitive radio network. In *2017 International Conference on Innovations in Information, Embedded and Communication Systems (ICIIECS)*, pages 1–5. IEEE, 2017.

[Fawcett01] T. Fawcett. Using rule sets to maximize roc performance. In *Proceedings 2001 IEEE International Conference on Data Mining*, pages 131–138, Nov 2001.

[Fouda17] Mona A Fouda, Adly S Tag Eldien, and Hala AK Mansour. Fpga based energy detection spectrum sensing for cognitive radios under noise uncertainty. In *2017 12th International Conference on Computer Engineering and Systems (ICCES)*, pages 584–591. IEEE, 2017.

[Gokceoglu14] A. Gokceoglu, S. Dikmese, M. Valkama, and M. Renfors. Energy detection under iq imbalance with single- and multi-channel direct-conversion receiver: Analysis and mitigation. *IEEE Journal on Selected Areas in Communications*, 32(3):411–424, March 2014.

[Grogan19] M. Grogan. Cross-correlation of currency pairs in r (ccf). `https://towardsdatascience.com/cross-correlation-of-currency-pairs-in-r-ccf-d27eec2d4b91`, Accessed: 2019.

[Gupta12] Subhanshu Gupta, Daibashish Gangopadhyay, Hasnain Lakdawala, Jacques C Rudell, and David J Allstot. A 0.8–2 ghz fully-integrated qpll-timed direct-rf-sampling bandpass $\sigma\delta$ adc in 0.13 μ cmos. *IEEE Journal of Solid-State Circuits*, 47(5):1141–1153, 2012.

[Haghighitalab18] Delaram Haghighitalab, Diomadson Belfort, Alp Kiliç, Aziz Benlarbi-Delaï, and Hassan Aboushady. A 2.4 ghz ism-band highly digitized receiver based on a variable gain lna and a subsampled $\sigma\delta$ adc. *Analog Integrated Circuits and Signal Processing*, 95(2):259–270, 2018.

[IEE19] Approved Draft Standard for Information Technology - Local and Metropolitan Area Networks - Specific Requirements - Part 22: Cognitive Radio Wireless Regional Area Networks (WRAN) Medium Access Control (MAC) and Physical Layer (PHY) Specifications: Policies

and Procedures for Operation in the Bands that Allow Spectrum Sharing where the Communications Devices may Opportunistically Operate in the Spectrum of the Primary Service. Standard, Institute of Electrical and Electronics Engineers, 2019.

[IEEE19] IEEE. Ieee c95.1-2019 - ieee approved draft standard for safety levels with respect to human exposure to electric, magnetic and electromagnetic fields, 0 hz to 300 ghz. `https://standards.ieee.org/standard/C95_1-2019.html`, Accessed: 2019.

[Imana17] E. Y. Imana, T. Yang, and J. H. Reed. Suppressing the effects of aliasing and iq imbalance on multiband spectrum sensing. *IEEE Transactions on Vehicular Technology*, 66(2):1074–1086, Feb 2017.

[Intel] Intel. Transceiver signal integrity development kit, stratix v gt edition. `https://www.intel.com/content/www/us/en/programmable/products/boards_and_kits/dev-kits/altera/kit-sv-gt-si.html`.

[International19] HL7 International. Hl7 information. `https://www.hl7.org/about/index.cfm?ref=common`, Accessed: 2019.

[Ishwerya17] P Ishwerya, S Geethu, and G Lakshminarayanan. An efficient hybrid spectrum sensing architecture on fpga. In *2017 International Conference on Wireless Communications, Signal Processing and Networking (WiSPNET)*, pages 662–665. IEEE, 2017.

[ISO12] ISO/IEC/IEEE International Standard - Information technology–Telecommunications and information exchange between systems Local and metropolitan area networks–Specific requirements Part 11: Wireless LAN Medium Access Control (MAC) and Physical Layer (PHY) Specifications. Standard, International Organization for Standardization, 2012.

[Ivanov18] Antoni Ivanov, Albena Mihovska, Krasimir Tonchev, and Vladimir Poulkov. Real-time adaptive spectrum sensing for cyclostationary and energy detectors. *IEEE Aerospace and Electronic Systems Magazine*, 33(5-6):20–33, 2018.

[Karimi19] Mohammad Karimi, Seyed Mohammad Sajad Sadough, and Mohammad Torabi. Optimal cognitive radio spectrum access with joint spectrum sensing and power allocation. *IEEE Wireless Communications Letters*, 9(1):8–11, 2019.

[Kent III07] Samuel D Kent III, Lloyd F Linder, and Khiem V Cai. Mixed technology mems/sige bicmos digitalized analog front end with direct rf sampling, March 6 2007. US Patent 7,187,735.

[Khalid19] Waqas Khalid and Heejung Yu. Sensing and utilization of spectrum with cooperation interference for full-duplex cognitive radio networks. In *2019 Eleventh International Conference on Ubiquitous and Future Networks (ICUFN)*, pages 598–600. IEEE, 2019.

[Knobel07] Robin Knobel and Diane Holditch-Davis. Thermoregulation and heat loss prevention after birth and during neonatal intensive-care unit stabilization of extremely low-birthweight infants. *Journal of Obstetric, Gynecologic, & Neonatal Nursing*, 36(3):280–287, 2007.

[Kulin18] Merima Kulin, Tarik Kazaz, Ingrid Moerman, and Eli De Poorter. End-to-end learning from spectrum data: A deep learning approach for wireless signal identification in spectrum monitoring applications. *IEEE Access*, 6:18484–18501, 2018.

[Kumar17] KA Arun Kumar. Fpga implementation of spectrum sensing engine for cognitive radios. In *2017 International Conference on Networks & Advances in Computational Technologies (NetACT)*, pages 116–119. IEEE, 2017.

[Lai13] Jin Lai, Eryk Dutkiewicz, Ren Ping Liu, and Rein Vesilo. Opportunistic spectrum access with two channel sensing in cognitive radio networks. *IEEE transactions on mobile computing*, 14(1):126–138, 2013.

[Li17] Xiaohua Li, Jian Zheng, and Mingjian Zhang. Compressive sensing based spectrum sharing and coexistence for machine-to-machine communications. In *2017 IEEE International Conference on Acoustics, Speech and Signal Processing (ICASSP)*, pages 3604–3608. IEEE, 2017.

[Liu17] Xia Liu, Zhimin Zeng, and Caili Guo. Cyclostationary spectrum sensing based channel estimation using complex exponential basis expansion model in cognitive vehicular networks. In *2017 20th International Symposium on Wireless Personal Multimedia Communications (WPMC)*, pages 167–172. IEEE, 2017.

[Liu19] Hang Liu, Xu Zhu, and Takeo Fujii. Cyclostationary based full-duplex spectrum sensing using adversarial training for convolutional neural networks. In *2019 International Conference on Artificial Intelligence in Information and Communication (ICAIIC)*, pages 369–374. IEEE, 2019.

[Lofts18] Andrew Lofts. RF-EMF Measurement using Software Defined Radio Receivers, 2018. Internship Report, University of Waterloo, Canada, Sorbonne University, Paris, France.

[Lv15] Qing Lv and Feifei Gao. Matched filter based spectrum sensing and power level recognition with multiple antennas. In *2015 IEEE China Summit and International Conference on Signal and Information Processing (ChinaSIP)*, pages 305–309. IEEE, 2015.

[Mahendru19] Garima Mahendru, Anil K Shukla, P Banerjee, and LM Patnaik. Adaptive double threshold based spectrum sensing to overcome sensing failure in presence of noise uncertainty. In *2019 6th International Conference on Signal Processing and Integrated Networks (SPIN)*, pages 466–471. IEEE, 2019.

[Martens12] Ewout Martens, André Bourdoux, Aissa Couvreur, Robert Fasthuber, Peter Van Wesemael, Geert Van der Plas, Jan Craninckx, and Julien Ryckaert. Rf-to-baseband digitization in 40 nm cmos with rf bandpass $\delta\sigma$ modulator and polyphase decimation filter. *IEEE Journal of Solid-State Circuits*, 47(4):990–1002, 2012.

[Mathew19] Libin K Mathew, AP Vinod, and AS Madhukumar. A cyclic prefix assisted spectrum sensing method for aeronautical communication systems. In *2019 IEEE International Symposium on Circuits and Systems (ISCAS)*, pages 1–5. IEEE, 2019.

[MathWorks18] MathWorks. *MATLAB Software.* MathWorks, Inc., Natick, MA, 2018.

[Medina18] Euler Edson Apaza Medina and Silvio Ernesto Barbin. Performance of spectrum sensing based on energy detection for cognitive radios. In *2018 IEEE-APS Topical Conference on Antennas and Propagation in Wireless Communications (APWC)*, pages 948–951. IEEE, 2018.

[Nair03] MNG Nair, Girish Gupta, and SK Jatana. Nicu environment: Can we be ignorant? *Medical Journal, Armed Forces India*, 59(2):93, 2003.

[Nasrallah17] A Nasrallah, A Hamza, G Baudoin, B Toufik, and A M Zoubir. Simple improved mean energy detection in spectrum sensing for cognitive radio. In *2017 5th International Conference on Electrical Engineering-Boumerdes (ICEE-B)*, pages 1–4. IEEE, 2017.

[Nassery12] A. Nassery and S. Ozev. An analytical technique for characterization of transceiver iq imbalances in the loop-back mode. In *2012 Design, Automation Test in Europe Conference Exhibition (DATE)*, pages 1084–1089, March 2012.

[Neyman33] Jerzy Neyman and Egon Sharpe Pearson. Ix. on the problem of the most efficient tests of statistical hypotheses. *Philosophical Transactions of the Royal Society of London. Series A, Containing Papers of a Mathematical or Physical Character*, 231(694-706):289–337, 1933.

[nuand18] nuand. bladerf - the usb 3.0 superspeed software defined radio. `http://nuand.com/`, 2018.

[Orduyilmaz19] Adnan Orduyilmaz, Mehmet Ispir, Mahmut Serin, and Murat Efe. Ultra wideband spectrum sensing for cognitive electronic warfare applications. In *2019 IEEE Radar Conference (RadarConf)*, pages 1–6. IEEE, 2019.

[Organization19a] World Health Organization. Electromagnetic fields and public health. `https://www.who.int/peh-emf/publications/facts/fs304/en/`, Accessed: 2019.

[Organization19b] World Health Organization. Neonatal mortality. `https://www.who.int/gho/child_health/mortality/neonatal_text/en/`, Accessed: 24-Jun-2019.

[Pineault17] Nicolas Pineault. *The Non-Tinfoil Guide to EMFs: How to Fix Our Stupid Use of Technology*. CreateSpace Independent Publishing Platform, 2017.

[Qing18] Lyu Qing, Han Guangyao, and Fu Xiaomei. Physical layer security in multi-hop af relay network based on compressed sensing. *IEEE Communications Letters*, 22(9):1882–1885, 2018.

[Ramírez18] GA Ramírez, MA Saavedra, and JL Araque. Analysis of an energy detection algorithm for spectrum sensing. In *2018 IEEE-APS Topical Conference on Antennas and Propagation in Wireless Communications (APWC)*, pages 924–927. IEEE, 2018.

[Rawat16] Danda B Rawat. Roar: An architecture for real-time opportunistic spectrum access in cloud-assisted cognitive radio networks. In *2016 13th IEEE Annual Consumer Communications & Networking Conference (CCNC)*, pages 936–941. IEEE, 2016.

[Razavi11] Behzad Razavi. *RF Microelectronics*. Prentice Hall, Los Angeles, California, 2011.

[Rebeiz13] Eric Rebeiz, Ali Shahed Hagh Ghadam, Mikko Valkama, and Danijela Cabric. Suppressing rf front-end nonlinearities in wideband spectrum sensing. In *8th International Conference on Cognitive Radio Oriented Wireless Networks*, pages 87–92. IEEE, 2013.

[Rebeiz15] Eric Rebeiz, Ali Shahed Hagh Ghadam, Mikko Valkama, and Danijela Cabric. Spectrum sensing under rf non-linearities: Performance analysis and dsp-enhanced receivers. *IEEE Transactions on Signal Processing*, 63(8):1950–1964, 2015.

[Rodriguez-Avila14] R. Rodriguez-Avila, G. Nunez-Vega, R. Parra-Michel, M. E. Guzman, and D. L. Torres-Roman. A frequency-selective i/q imbalance analysis technique. *IEEE Transactions on Wireless Communications*, 13(4):1854–1861, April 2014.

[RStudio Team15] RStudio Team. *RStudio: Integrated Development Environment for R*. RStudio, Inc., Boston, MA, 2015.

[Safatly14] Lise Safatly, Ali El-Hajj, and Karim Y Kabalan. Blind and robust spectrum sensing based on rf impairments mitigation for cognitive radio receivers. In *2014 International Conference on High Performance Computing & Simulation (HPCS)*, pages 820–824. IEEE, 2014.

[Sayed16] Alhassan Sayed. *RF Front End Receiver for Cognitive Radio based on $\Sigma\Delta$ Analog-to-Digital Converter*. PhD thesis, Sorbonne University, Paris, France, 2016.

[Schreier99] R. Schreier. The delta-sigma toolbox for matlab. *Oregon State University*, November 1999.

[Schreier05] Richard Schreier, Gabor C Temes, et al. *Understanding delta-sigma data converters*, volume 74. IEEE press Piscataway, NJ, 2005.

[Sengupta19] Anisha Sengupta, Sudipta Chattopadhyay, Suman Roy Ghatak, and Vaishna Biswas. Two-stage spectrum sensing model for varying snr conditions in cognitive radio network. In *2019 International Conference on Electrical, Electronics and Computer Engineering (UPCON)*, pages 1–6. IEEE, 2019.

[Shibata12] Hajime Shibata, Richard Schreier, Wenhua Yang, Ali Shaikh, Donald Paterson, Trevor C Caldwell, David Alldred, and Ping Wing Lai. A dc-to-1 ghz tunable rf $\delta\sigma$ adc achieving dr=74 db and bw=150 mhz at f_0=450 mhz using 550 mw. *IEEE journal of solid-state circuits*, 47(12):2888–2897, 2012.

[Smith19] Karly Smith. Data Analysis of medical physiological parameters and RF-EMF parameters, 2019. Internship Report, University of Waterloo, Canada, Sorbonne University, Paris, France.

[So15] Jaewoo So and Rayadurgam Srikant. Improving channel utilization via cooperative spectrum sensing with opportunistic feedback in cognitive radio networks. *IEEE Communications Letters*, 19(6):1065–1068, 2015.

[Söderberg02] Karin C Söderberg, Estelle Naumburg, Gert Anger, Sven Cnattingius, Anders Ekbom, and Maria Feychting. Childhood leukemia and magnetic fields in infant incubators. *Epidemiology*, 13(1):45–49, 2002.

[Statistical Methods19] NIST/SEMATECH e-Handbook of Statistical Methods. e-handbook of statistical methods 6.4.4.2. stationarity. `https://www.itl.nist.gov/div898/handbook/pmc/section4/pmc442.htm`, Accessed: 2019.

[Sun16] Dafei Sun, Tiecheng Song, Bin Gu, Xi Li, Jing Hu, and Miao Liu. Spectrum sensing and the utilization of spectrum opportunity tradeoff in cognitive radio network. *IEEE Communications Letters*, 20(12):2442–2445, 2016.

[Surampudi16] Atchutananda Surampudi and K Kalimuthu. An adaptive decision threshold scheme for the matched filter method of spectrum sensing in cognitive radio using artificial neural networks. In *2016 1st India International Conference on Information Processing (IICIP)*, pages 1–5. IEEE, 2016.

[Tani15] Andrea Tani, Romano Fantacci, and Dania Marabissi. A low-complexity cyclostationary spectrum sensing for interference avoidance in femtocell lte-a-based networks. *IEEE Transactions on Vehicular Technology*, 65(4):2747–2753, 2015.

[Taparugssanagorn14] Attaphongse Taparugssanagorn, Kenta Umebayashi, Janne Lehtomäki, and Carlos Pomalaza-Ráez. Analysis of the effect of nonlinear low noise amplifier with memory for wideband spectrum sensing. In *1st International Conference on 5G for Ubiquitous Connectivity*, pages 87–91. IEEE, 2014.

[Teguig18] Djamel Teguig and Mohamed S Azzaz. Fpga implementation of spectrum sensing methods for cognitive radio. In *2018 International Symposium on Networks, Computers and Communications (ISNCC)*, pages 1–5. IEEE, 2018.

[To19a] Statistics How To. Adf - augmented dickey fuller test - statistics how to. `https://www.statisticshowto.datasciencecentral.com/adf-augmented-dickey-fuller-test/`, Accessed: 2019.

[To19b] Statistics How To. Kpss test: Definition and interpretation - statistics how to. `https://www.statisticshowto.datasciencecentral.com/kpss-test/`, Accessed: 2019.

[Turk17] Shadi Turk. Design and Implementation of a Configurable Circuit for Spectrum Sensing, 2017. M.Sc. Report, Sorbonne University, Paris, France.

[Umar13] Raza Umar, Asrar UH Sheikh, and Mohamed Deriche. Unveiling the hidden assumptions of energy detector based spectrum sensing for cognitive radios. *IEEE communications surveys & tutorials*, 16(2):713–728, 2013.

[Umar14] Raza Umar, Asrar UH Sheikh, and Mohamed Deriche. Unveiling the hidden assumptions of energy detector based spectrum sensing for cognitive radios. *IEEE Communications Surveys & Tutorials*, 16(2):713–728, 2014.

[Valkama01] M. Valkama, M. Renfors, and V. Koivunen. Advanced methods for i/q imbalance compensation in communication receivers. *IEEE Transactions on Signal Processing*, 49(10):2335–2344, Oct 2001.

[Wang17] Xusong Wang, Shailesh Chaudhari, Mihir Laghate, and Danijela Cabric. Wideband spectrum sensing measurement results using tunable front-end and fpga implementation. In *Signals, Systems, and Computers, 2017 51st Asilomar Conference on*, pages 499–503. IEEE, 2017.

[Yu11] Tsung-Han Yu, Oussama Sekkat, Santiago Rodriguez-Parera, Dejan Markovic, and Danijela Cabric. A wideband spectrum-sensing processor with adaptive detection threshold and sensing time. *IEEE Transactions on Circuits and Systems I: Regular Papers*, 58(11):2765–2775, 2011.

[Yucek09a] T. Yucek and H. Arslan. A survey of spectrum sensing algorithms for cognitive radio applications. *IEEE Communications Surveys Tutorials*, 11(1):116–130, First 2009.

[Yucek09b] Tevfik Yucek and Huseyin Arslan. A survey of spectrum sensing algorithms for cognitive radio applications. *IEEE communications surveys & tutorials*, 11(1):116–130, 2009.